UNIVERSITA' DEGLI STUDI DI CATANIA

DIPARTIMENTO DI FISICA E ASTRONOMIA

DOTTORATO DI RICERCA IN SCIENZA DEI MATERIALI E NANOTECNOLOGIE

ALESSANDRO MELI

Epitaxial growth and characterization of thick 4H-SiC epi-layer for neutron detection application

Tutor:

Prof.ssa L. Calcagno

Dott. Francesco La Via

Anno accademico 2021- 2022

Acknowledgements

The completion of this thesis could not have been possible without the contribution and guidance of many people that I had the opportunity to meet and work with.

First and foremost, I would like to express my deepest thank you to my advisor Dr. Francesco La Via who gave me the opportunity to be his PhD student and work under his guidance. I really appreciate all his continuous support, time, advice and ideas that had helped and encouraged me to widen my research work.

Besides, I would like to send my thanks to my other advisor Prof. Lucia Calcagno for all her help regarding administrative papers and fruitful discussions about the measurements of the epilayers and diodes. I really appreciate their helpful suggestions and corrections in order to complete the present manuscript.

I should also thank the ENI group, Antonio Trotta, Laura Meda and Miriam Parisi for their help, support and attention to details when it came to experiments, writing and presentations.

To Annamaria Muoio for all her support and help for electrical measurements and simulations with Comsol and FLUKA tool. Many thanks go to all the people who have been and are at CNR-IMM Headquarter in Catania for creating a nice environment to work too, for their help and support during my research.

My thanks also go out to the other PhD students, for their mutual support, and researchers who shared their views and experiences in the field during common shared trainings events and conferences. Moreover, the wonderful environment and the friendships created are invaluable.

I should also thank Matteo H. Kushoro, M. Rebai and M. Tardocchi from CNR-ISTP in Milano for the detector characterization under working conditions.

Lastly, I would like to express my deep graditude to my family and friends for their support and for beliving in me during all this period.

Index

Introduction

The growing technological development in various fields of application has given a greater impetus to the use of increasingly complex devices, miniaturized on a micrometric scale, such as to integrate in the single device-system a multiplicity of functions capable of implementing a complex interaction between the external world and the system itself. The concept of "microsystem" (MS) was then spreading to have, therefore, microscopic devices designed, assembled, and used to interact and produce alterations in each environment, thus allowing for greater operational reliability, low energy consumption, reduced dimensions, weigh and, in the future, low production costs. The fields of application where is observed an increasingly massive use of microsystems are automotive, industrial automation, consumer electronics and biomedicine. Nowadays, the basic technologies and materials for the realization of the MS are those by consolidated deriving from the microelectronics of integrated circuits and from the chemical micromachining of silicon and its oxide. However, the use of microsystems for innovative applications where high performance is required in hostile environments and in critical operating conditions, such as in the presence of corrosive agents, high temperatures, strong mechanical stress and intense levels of photonic radiation and particles, made it necessary to introduce new materials with chemical-physical properties that better respond to these application sectors.

Among these, the diamond, and the synthetic single crystal diamond (SCD, "Single Crystal Diamond") produced by chemical vapor deposition (CVD, "Chemical Vapor Deposition"), the material towards which, by now for decades, the interest of the world has grown stronger scientific and technological, and the amount of related theoretical-applicative studies is increasingly broad and in-depth. Thanks to its excellent mechanical, optical, thermal and electronic qualities and, in particular, to the high energy gap between the valence band and the conduction band (5.5 eV of the diamond against 1.12 eV of Si), to the consequent low noise in the presence of both high temperatures and visible radiation, high melting point, low reactivity, extreme resistance to difference, diamond seems to be, on the one hand, the ideal candidate to operate in hostile environments and, on the other, the most suitable material to replace silicon for the realization of microsystems operating in such contests.

The experimental results clearly demonstrated the ability of these detectors to be able to operate stably, without any degradation of the spectroscopic performance, as in shown in figure 1, and in a reproducible way, for neutron diagnosis even in large nuclear plants and in the presence of large fluxes. However, the high cost, the small dimensions of the samples

and a low availability of commercial monocrystalline diamond allow the use of alternative materials.

The limited availability of large size commercial single crystal diamonds has led to the development of a 12-pixel (5x5 mm^2 each) matrix to boost the counting rate, especially in D plasmas, instead of having a single diamond detector with equal area.

Diamond detectors have been shown to withstand neutron fluence up to $2x10^{14}$ n/cm^2 as shown in [1] for single crystal and in [2] for polycrystalline diamonds.

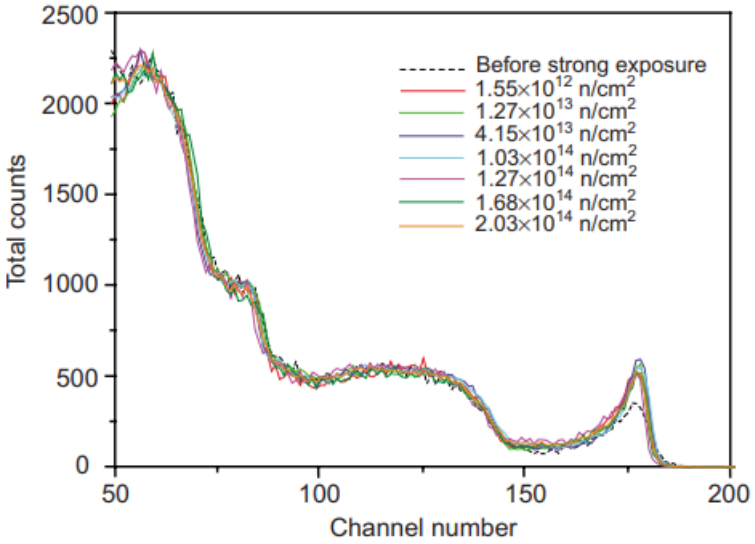

Figure 1. Pulse heigh spectrum (PHS) in the diamond detector irradiated by 14.1 MeV neutrons which shows the radiation hardness for these detectors [1].

The latter, after irradiation with $8x10^{14}$ n/cm^2, recovers up to 70% of their initial performance after a suitable annealing. Moreover, transient effects have been noticed for SCD detectors irradiated with high energy neutrons and alpha particles [3]. Transient effects are due to partial trapping of the charge carries within the detector bulk defects and in the interfaces between the diamond crystal and the ohmic contacts. These are known as polarization effects and depend on the type, and amount, of crystal defects, naturally present or induced by neutron irradiation [4].

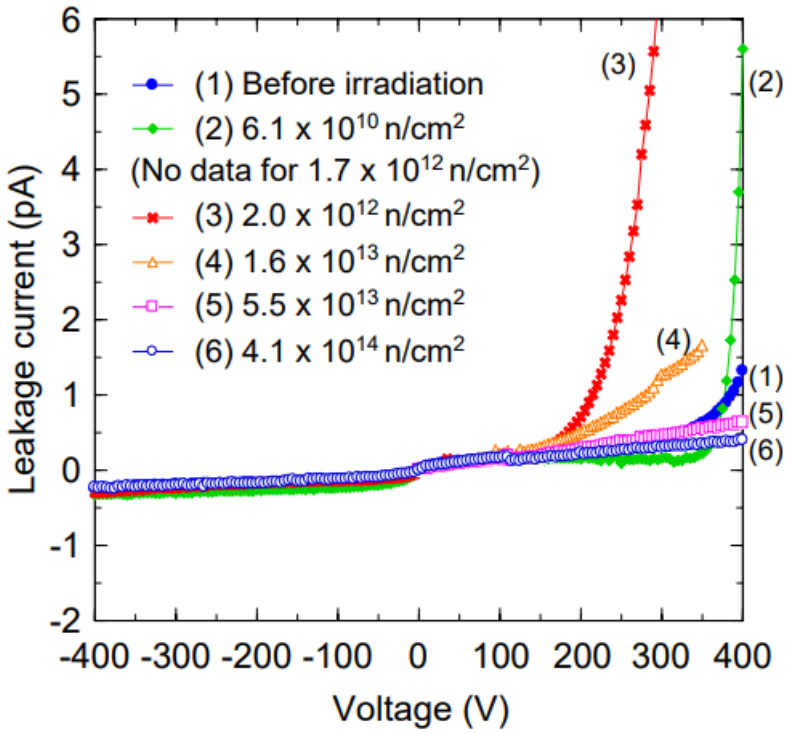

Figure 2. Change in I-V characteristics after neutron irradiation for SCD detectors [4].

The polarization effect can be reset by inverting the bias voltage, as discussed in [5], but it could affect energy resolution if not considered.

Therefore, in future projection, SiC can be considered a good alternative material for the realization of sensors in more complex microsystems, resistant to diffusion and operating effectively even in hostile operating conditions such as in a thermonuclear fusion reactor for neutron detection. Silicon carbide (SiC) is one of the Wide Band Gap (WBG) semiconductors which possess intriguing physical properties which can lead to higher power density, higher junction temperature and higher voltage capabilities.

SiC has been extensively studied for decades in academic institutions and at industrial level, but recent advancements in SiC growth technology (commercially available 6-inch 4H-SiC wafers and in the future years also 8-inches 4H-SiC wafers with reduced defect density and zero micropipes) demonstrate the material benefits for power electronics regarding power energy, efficiency, performance, and a reduction of device costs. All these progress in material technology attracted more attention from industrial level as more and more SiC power devices are reaching the market.

Although technological breakthroughs are evident, the SiC epitaxial growth still confronts with several important challenges that are limiting the device performances. To reduce such

limitations, we need to continue the understanding of growth mechanisms and impurity incorporation. Doping of SiC is performed usually during in-situ epitaxial growth to adjust the properties of the grown material to the device requirements. Therefore, process optimization and comprehension of doping mechanism in the epitaxial layers are necessary to avoid the defects formation and increment the parameters that strongly influence the performances of the devices, such as carrier lifetime and diffusion length.

SiC devices have been already used in the past to measure the thermal neutron flux in reactors [6] and the 14 MeV neutrons from DT reactions. As shown in [7] good quality SiC detectors are now available, and measurement of the fast neutron spectrum is possible also at high temperatures as done with diamond detectors [8], as is shown in figure 3.

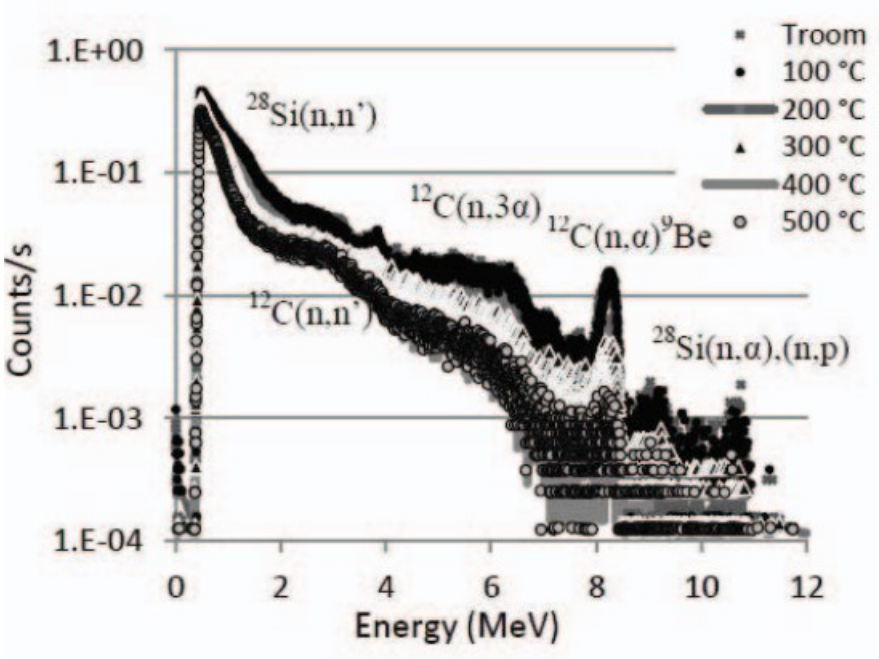

Figure 3. The resulted energy histograms recorded during irradiation tests with 14 MeV neutrons on different ambient temperatures. The structure of the energy histogram is determined by deep inelastic nuclear reactions between neutrons and the crystal atoms of SiC. The most prominent orientation point on the spectrum is served by the full energy peak of the $^{12}C(n,\alpha)^{9}Be$ reaction, which could be distinguished on all the applied measurement temperatures [9].

Today SiC detectors can be produced in relatively large areas (up to 1.5 cm^2), with thicknesses up to 250 μm and with a low number of defects per cm^2, which represent an excellent enhancement in the SiC growth technology (see Ref. [10]). This allows for the use of these detectors in environments in which fast neutron spectroscopy is required at high counting rates (up to 1 MHz) such as neutron spectroscopy of fusion plasmas. In fact, due to the short time scales of the phenomena that can occur in fusion plasmas (typical time scales of the order of tens of ms), high count rate capability is a paramount [11] [12]. In addition, the possibility of growing SiC layers with large area and with different thickness, makes this

material an interesting candidate for applications in fusion plasma physics, like for instance for Fast Ions Loss Detectors (FILD) that measure the fast ions lost by the plasma before they hit the first wall. Currently, FILD systems are based on scintillator crystals coupled to optical fibres leading scintillation light towards a CDD [13]. They work in an environment where neutrons are the highest source of background. An advantage of SiC in this application is that, by decreasing the crystal thickness, the detector efficiency for neutrons can be accordingly decreased to as low as 10^{-5}, without losing efficiency for 500 keV ions. Moreover, in the near future they could be worked in Geiger mode, in order to detect single photons [14].

As in SCDs, neutron detection in SiC is based on the collection of electrons–hole pairs produced by charged particles generated by neutron interaction with C and Si nuclei (see Figure 4). Due to their abundances in natural C and Si, in this work we will consider only interaction on ^{12}C and ^{28}Si.

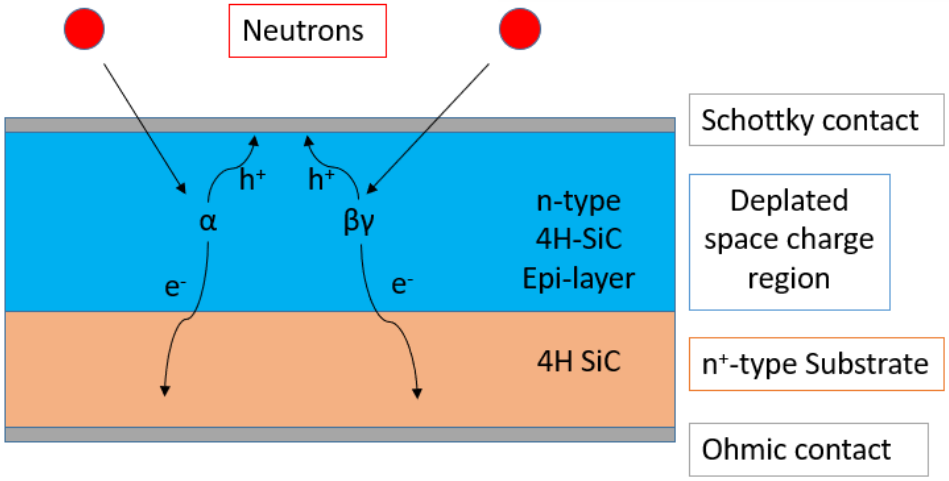

Figure 4. Design of a SiC detector and the charge separation due to neutron interaction with Si and C nuclei and bias applied.

When a neutron does undergo interaction, it is with a nucleus of the absorbing material and it is detected through nuclear reactions which result in energetic charged particles such as alpha (α) particles, gamma rays (γ), protons and so on. Virtually every type of neutron detector involves the combination of an absorbing material designed to carry out this conversion together with conventional radiation detectors which detect the charge particles above mentioned. A detailed description of the most useful detection processes can be found in [15].

The electrons and holes generated by the radiation are then separated by an electric field, generated by the detector bias, and their motion induces a current pulse at the anode and cathode electrodes, respectively. The detection of such pulses via external circuits in a pulse processing method allows the construction of a histogram of pulse heights (the pulse height spectrum).

In all the materials the interacting neutrons increase by increasing the thickness of the detectors, but very thick detectors are difficult to be realized due to the increase of defects density in very thick epitaxial layers, that could be improved with new advances on epitaxial growth processes. Furthermore, a higher bias is needed to deplete the thick epitaxial layer, necessary for the correct functioning of the detector. To decrease this high voltage, it is possible to decrease the doping concentration in the epitaxial layer, but in the case of silicon carbide is extremely difficult to reach doping concentration lower than $1x10^{14}/cm^3$. In our case, for a detector with a 250 μm thick epi-layer we need to use bias of around 5000Vcompared to the 700V used for a 100 μm thick epitaxial layer. Instead, the high voltage necessary to deplete a thick epitaxial layer, and the low yield of the very thick detectors with large area are the main limitation of this technology.

Another aspect that should be taken under consideration is that when we use very thick epitaxial layers for the detectors, we need to have a diffusion length larger than the depleted layer to have a good charge collection, but with an optimized epitaxial growth process we can reach this purpose.

Then with a good epitaxial process the diffusion length does not seem to be the limiting factor in the increase of the epitaxial layer thickness and of the neutron sensitivity. Indeed, to obtain the maximum efficiency of the detector it is necessary to deplete the entire area. The voltage at which a given thickness depletes strongly depends on the doping level of the epitaxy. Therefore, to have low depletion voltages it is necessary to have low doping, as mentioned before. This problem currently limits the possibility of using SiC detectors with thicker epitaxial layers.

Despite the actual limitation, 4H-SiC detectors could be the promising alternative to the current detectors used (Single Crystal Diamond-SCD) for a variety of reasons including the good radiation hardness and the high carrier lifetime also due to the mature epitaxial growth technology, which allows to obtain large thicknesses and detectors with larger areas than the diamond.

The manuscript is structured in four chapters, as follows:

In the first part of the first chapter an overview of the SiC material is presented. It includes details about the chemical, physical and electrical properties of the most used SiC polytypes in microelectronics, focusing on the 4H SiC polytype. A new field of application for 4H-SiC material was presented, in particular as neutron detector in a thermonuclear fusion reactor. The second part of the chapter was attributed to the description of the Silicon Carbide properties and the growth process of epitaxial layers to obtain a thick epi-layer, 250 μm and presents the different defects formed in the epitaxial layer and the general characterization of this epi-layer, focusing the attention on stacking Faults (SFs) defects and their influence on devices performances.

In the second chapter the state of art of SiC detectors is described focusing the attention on the different field of application, in particular as neutron detection in harsh environments.

In the chapter three there is a deep description of the characterization techniques and the information obtained useful for our purposes. In particular, the study of important parameters as carrier lifetime and diffusion length was evaluated to understand the possible use of these devices for detection application. This chapter represent the core of the research study showing the advantages of using SiC detectors on this field of application.

Chapter four has been assigned to device fabrication and its electrical characterization, which is the last chapter of this manuscript, it includes the electrical design and analysis of prototype devices and tests under working conditions.

The manuscript is closed by some general conclusions of the main results obtained during this study and perspectives of further studies.

1 Chapter 1. Silicon Carbide overview

Power semiconductor devices constitute the heart of power electronics systems, and silicon (Si)- based power devices have been the dominant choice for this system. However, as the needs and requirements for electrical energy continuously grow, Si-based power devices have limited performance related to inherent material characteristics, which make them unable to meet future demands, especially in high-voltage, high-efficiency, and high-power density applications [16] [17]. SiC has become the material of choice for next generation power semiconductor devices to replace existing Si technology. The wider bandgap, higher thermal conductivity, and larger critical electric field allow SiC devices to operate at higher temperatures, higher current density, and higher blocking voltages than Si power devices. Not only for power devices but also in the field of detection, SiC could be an alternative material to the current materials used, especially in hostile environments thanks to its radiation hardness.

Silicon carbide is comprised of equal parts silicon and carbon via covalent bonding. Since this process will lead to a highly ordered configuration, a single crystal SiC is extremely hard; in fact, it is known to be the third hardest substance on earth. There are more than 200 different polytypes. Depending on the polytype crystal structure, the energy gap of silicon carbide varies from 2.2 to 3.3 eV. Among them, 4H and 6H are of interest technologically since large wafers can be made in this material, and hence used for device production. Table 1 summarizes the characteristics of 4H and 6H SiC devices in comparison with Si devices.

Table 1. Main physical properties of SiC material compared to Si and Diamond.

Electrical Property	Si	SiC (4H)	SiC (6H)	Diamond
Band Gap Energy (eV)	1.12	3.28	2.96	5.5
Critical Electrical Field (MV/cm)	0.29	2.5	3.2	20
Hole mobility (cm^2/VS)	490	115	90	1800
Electron Mobility (cm^2/VS)	1200	800	370	2200
Thermal Conductivity (W/cmK)	1.5	3.8	3.8	20
Maximum Junction Temperature (°C)	150	600	600	1927

As observed in Table 1, the wide band gap energy of SiC results in several favourable characteristics for power electronics devices and hostile environment applications.

1.1 Crystalline structure

SiC is a compound semiconductor, with a rigid stoichiometric composition (Si:C=1:1), 50% silicon (Si) and 50% carbon (C). The electronic structures of neutral Si and C atoms in their ground states are:

$$\text{Si - } 14e^- : 1s^2 2s^2 2p^6 3s^2 3p^2$$
$$\text{C - } 6e^- : 1s^2 2s^2 2p^2$$

Both Si and C atoms are tetravalent elements and have four valence electrons in their outermost shells. Si and C atoms are tetrahedrally bonded with covalent bonds by sharing electron pairs in sp^3-hybrid orbitals to form a SiC crystal. Each Si atom has exactly four C atom neighbours, and vice versa. The fundamental structural unit is a tetrahedron, with four atoms of Si (C) and one atom of C (Si) at the center, as shown in Fig. 5.

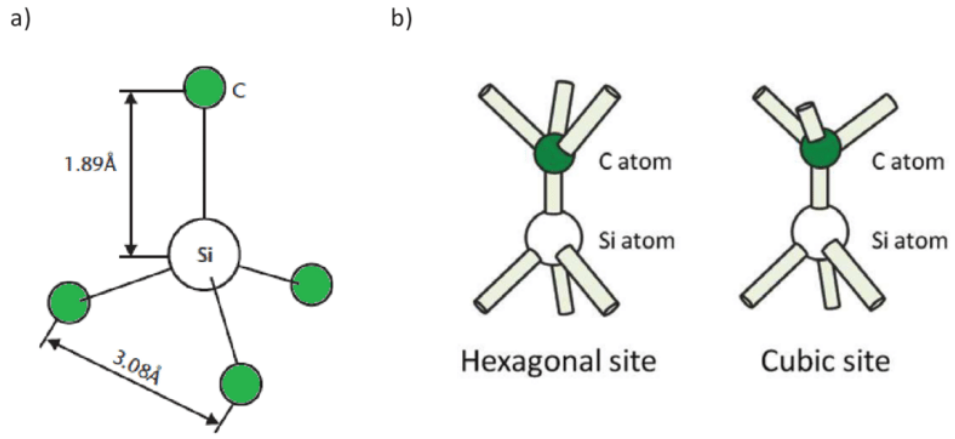

Figure 5. (a) SiC tetrahedron structure and (b) hexagonal and cubic sites.

The distance between adjacent C is near to 3.08 Å (a); the Si atom is located at mass centre of the tetrahedral structure so that to keep an equidistance among neighbouring C atoms of about 1.89 Å. The height of the cell (c) changes among the polytypes: in particular, the c/a ratio is 1.641, 3.271 e 4.908, respectively for 2H-, 4H- and 6H-SiC [18]. The Si-C bond energy is very high (4.6 eV), which gives SiC a variety of outstanding properties, as described below.

From a crystallographic point of view, SiC is the best known example of polytypism, which is the phenomenon where a material can adopt different crystal structures which vary in one dimension (that is, in stacking sequence) without changes in chemical composition. The variation in the occupied sites along the c-axis in a hexagonal close-packed system brings

about different crystal structures, known as polytypes. Consider the occupied sites in the hexagonal close-packed system, shown schematically in Figure 6.

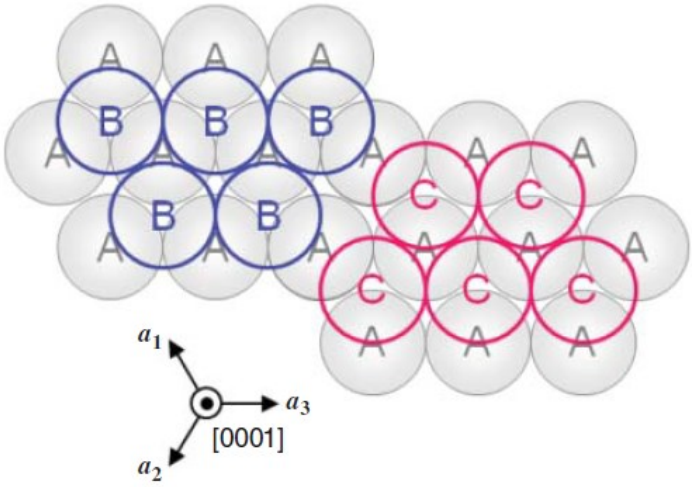

Figure 6. Hexagonal close-packed system in the stacking sequence.

There are three possible sites, denoted as A, B, and C. Two layers cannot successively occupy the same site; the next layer on top of an "A" layer must occupy either "B" or "C" sites (and, similarly, "A" or "C" is allowed over "B"). Though there exist, in principle, almost infinite variations of the stacking sequence when stacking several layers; for most materials, only one stacking structure (often either the zincblende or wurtzite structure) is usually stable. However, SiC crystallizes in surprisingly many (more than 200) polytypes. A schematic view of different stacking sequence for some common SiC polytypes is presented in Fig. 7, while a complete analysis to SiC polytypism can be found in [19].

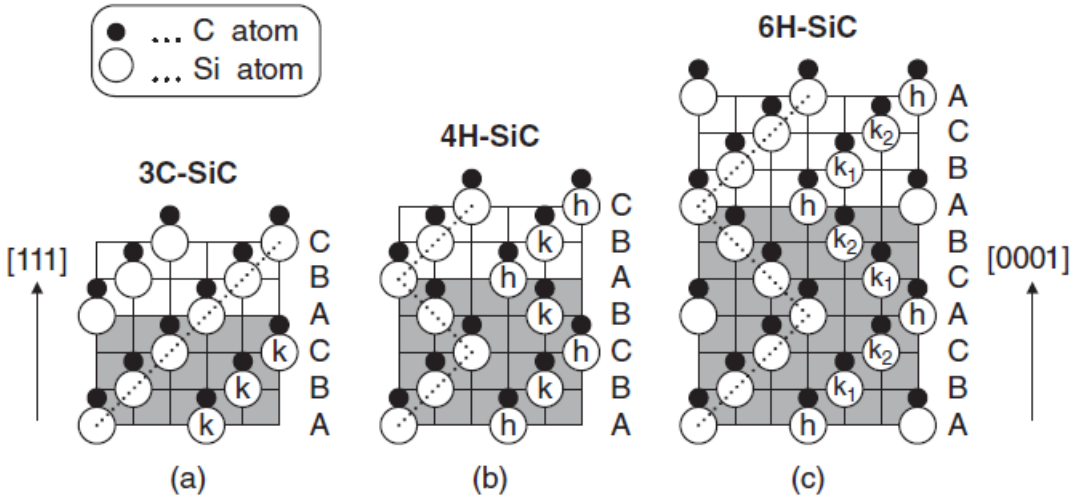

Figure 7. Stacking sequence of the three most common SiC polytypes [20].

Depending on the stacking order, the bonding between Si and C atoms in adjacent bilayer planes is either of zinkblende (cubic) or wurtzite (hexagonal) nature. So that each type of bond provides a slightly altered atomic environment, whose effect is relevant when the substitutional impurity incorporation and electronic transport properties of SiC are considered. The inequivalent layers are denoted by the letters h and k and the hexagonality of a polytype can be defined as the percentage of h-type layers, according to the Jagodzinski's notation [20].

There are other different ways to indicate the SiC polytypes. The traditional notation consists of using the stacking sequence, so that 4H- and 6H-SiC are respectively indicated by the sequence of ABCB and ABCACB. Besides this, another commonly used notation is due to Ramsdell [21] who categorizes every polytype with a number, followed by a letter: the first one represents the stacking periodicity, while the latter the bonding type, so that 4H- and 6H-SiC are hexagonal polytypes (which are also referred to as α-SiC in literature) with a stacking period of four and six, respectively. A review of the possible notations for indicating the principal SiC polytypes is reported in Table 2.

Table 2. Most common notations to define SiC polytypes.

Ramsdell's notation	Zhdanov's notation	Jagodzinski's notation
2H	11	h
3C	∞	k
4H	22	hk
6H	33	hkk
15R	$(32)_3$	hkkhk

1.2 Electronic structure and Energy bandgap (E_g)

Different polytypes differ only in the stacking of double layers, however, this affects all electronic and optical properties of the crystal. From an application viewpoint the important polytypes are the 3C and the 6H and 4H. The latter two can be grown conveniently thanks to your mature technology and the fact that it was the first SiC polytype used in microelectronics, unlike 3C-SiC. Let's focus on the 4H-SiC polytype. 4H-SiC has two non-equivalent positions for carbon and silicon atoms according to hexagonal (h) and cubic (k)

bilayers. Properties and electronic structure of defects may vary depending on the two different places. This is called site-dependency. Polytypes with hexagonal crystal structure have hexagonal Brillouin zone (BZ). Fig.5 shows the most important points in the hexagonal Brillouin zone, as well as the M − Γ section of the calculated band structure of 4H-SiC. Silicon carbide is an indirect semiconductor. In 4H-SiC the conduction band minimum is at the M point, while the valence band maximum is at the Γ point of the BZ see Fig.8. Carbon and silicon atoms are bonded by sp^3 hybrid covalent bonds. Due to the higher electronegativity of carbon atoms, bonds are slightly negatively polarized toward carbon atoms.

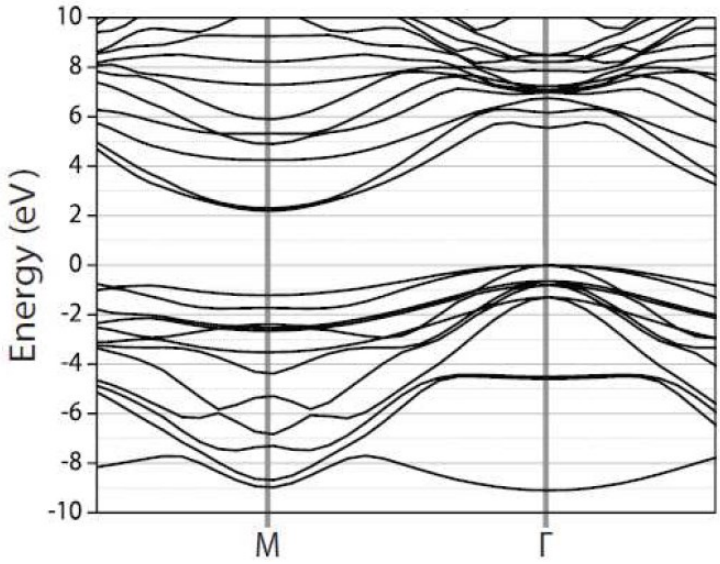

Figure 8. Illustrative picture of the indirect gap of the calculated band structure of 4H-SiC [22].

The band gap in SiC polytypes is indirect. Experimentally, the band gap energy for the different polytype range from 2.39 eV for 3C-SiC, to 3.330 for 2H-SiC with 3.265 eV for 4H-SiC [22] at room temperature. The top of the valence band is at the Γ point (k=0) in the Brillouin zone (BZ), whereas the conduction band minima occur at the BZ boundary. The exact positions of the conduction band minima and their energy with respect to the top of the valence band (the band gap) depend on the polytype. For example, the minima are at the X points in the BZ of 3C-SiC (Fig.9), the M points in the BZ of 4H-SiC, and along the M-L lines in the BZ of 6H-SiC (Fig.9 b). The number of equivalent conduction band minima is therefore three, three, and six, respectively for these polytypes.

Photons with the necessary energy to bridge the band gap have a very small momentum or k-vector compared with the k-vector separation between the valence and conduction band edges.

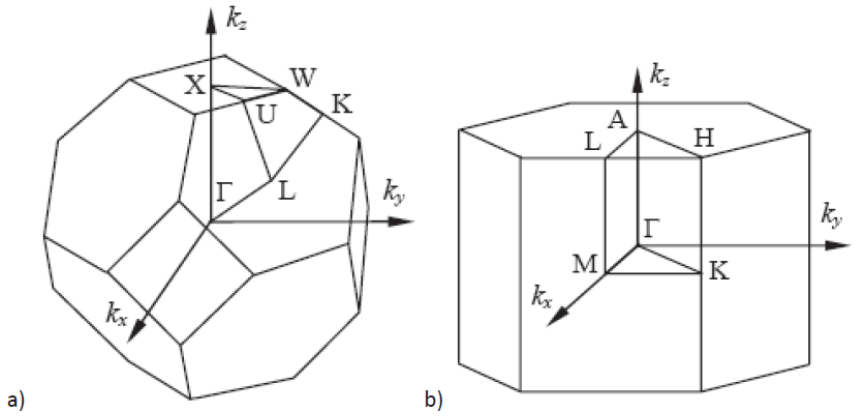

Figure 9. Brillouin zones for a) cubic (3C) and b) hexagonal (4H and 6H) SiC.

The top of the valence band in SiC is *P*-like. The holes can thus be characterized by an orbital angular momentum L_h=1 and a spin S_h=1/2. A small splitting of the valence band states results from the spin-orbit (SO) coupling and the crystal field (CF) of the particular SiC polytype. The degeneracy of *P*-like states is not lifted in cubic symmetry. Therefore, in 3C-SiC the valence band edge is only split by SO coupling. The resulting states are states of total angular momentum J_h =3/2 and J_h=1/2, the former lying uppermost. In the hexagonal and rhombohedral polytypes the CF is uniaxial, and thus the *P*-like states are affected.

An electron at the bottom of the conduction band in SiC behaves as a spin like particle, that is, L_e=0 and S_e=1/2. In addition to spin degeneracy, there will also be degeneracy owing to the occurrence of several inequivalent conduction band minima. The wavefunction of the electron can be described by a linear combination of the wavefunctions belonging to the different conduction band minima. If the electron is localized at a defect, the linear combinations will have to conform to the symmetry of the defect. Since the different possible combinations will overlap differently with the defect, they may have different energies resulting in so-called valley orbit (VO) splitting. In Fig. 10 we can see a diagram of the energy band gap for the five most common SiC polytypes. The energy difference of the conduction band of the cubic polytype in respect with the hexagonal is quite large while the respective differences in the valence bands is of the order of 1/10 of the differences in the conduction bands.

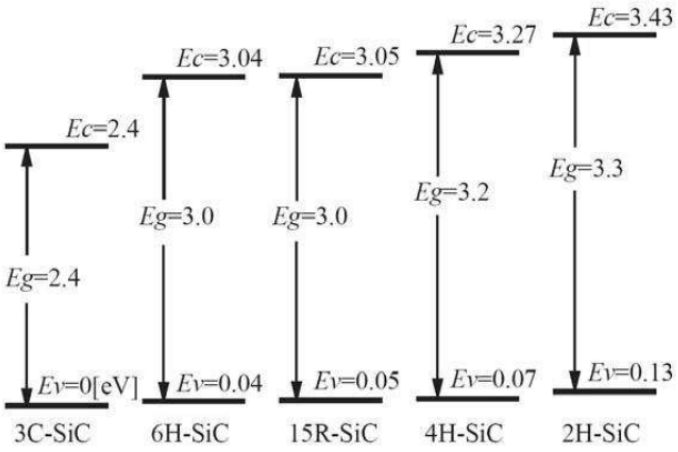

Figure 10. The energy diagram of five most common polytypes.

The experimentally energy band gap for 4H-SiC is 3.265 eV [22]. Fig. 11 shows the band gap structure of 4H-SiC. The wide band gap makes it possible to use SiC for very high temperature operation.

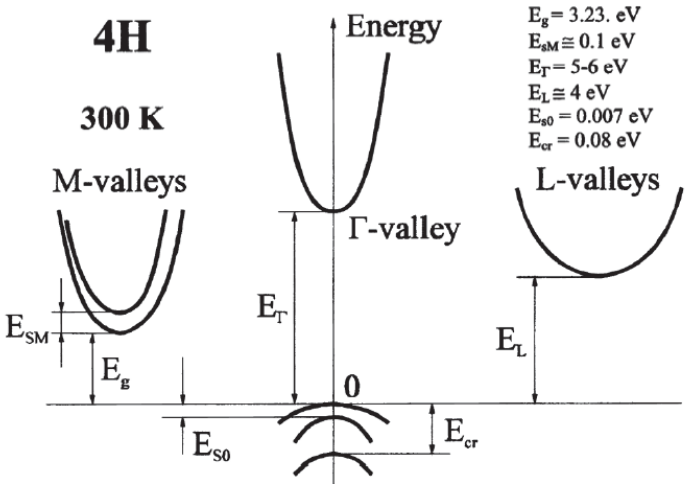

Figure 11. Band structure of 4H-SiC at 300K. Important minima of the conduction band and maxima of the valence band are shown.

Thermal ionization of electrons from the valence band to the conduction band, which is the primary limitation of Si-based devices during high temperature operation, is not a problem for SiC-based devices due to the wide band gap.

1.3 Transport properties

The transport properties of 4H-SiC polytype are listed in Table 3, along with other wide bandgap semiconductors, like Gallium Nitride and Diamond, and the most commonly used semiconductor materials (Si and GaAs). By a direct comparison, the advantages of SiC over Si are the tenfold increase in breakdown fields, twofold increase in saturation velocity, and more than doubling of thermal conductivity.

Although the carrier mobility in Silicon Carbide is somewhat lower than in Silicon, in general the transport parameters give Silicon Carbide devices better performances than comparable Silicon devices.

Investigating the basic electrical and physical parameters for electronic devices, such as bandgap (*Eg*), mobility (μ), saturation velocity (*vsat*), breakdown electric field (*Ecrit*), and thermal conductivity (λ), it instantly evident that wide bandgap semiconductors are very promising materials for using in high performance electronic devices.

Table 3. Main characteristics for 4H-SiC vs other semiconductors material.

	Si	*GaAs*	*4H-SiC*	*GaN*	*Diamond*
$E_{g\ @300K}$ *[eV]*	1.1	1.4	3.2	3.4	5.4
E_c *[MV/cm]*	0.3	0.4	2.2	2.0	10.0
v_{sat}*[x10^{7}cm/s]*	1.0	2.0	2.0	2.5	2.7
$\mu_{n\ @N=10^{16}cm^{-3}}$ *[cm^2/Vs]*	1500	8500	720	1000	2200
$\mu_{p\ @N=10^{16}cm^{-3}}$ *[cm^2/Vs]*	480	400	120	30	850
ε_r	11.9	13.1	9.7	8.9	5.5
λ *[W/cm K]*	1.5	0.5	5.0	1.3	22

In general:

- A higher electric breakdown field brings to power devices with higher breakdown voltages. For the same breakdown voltage, instead, the consequence of higher E_{crit} is the reduction of the width of the drift region, which enables smaller unipolar device and smaller on-resistance as can be seen in Fig. 12. The ramifications of this are a lower conduction loss and, as a consequence, increasing efficiency.

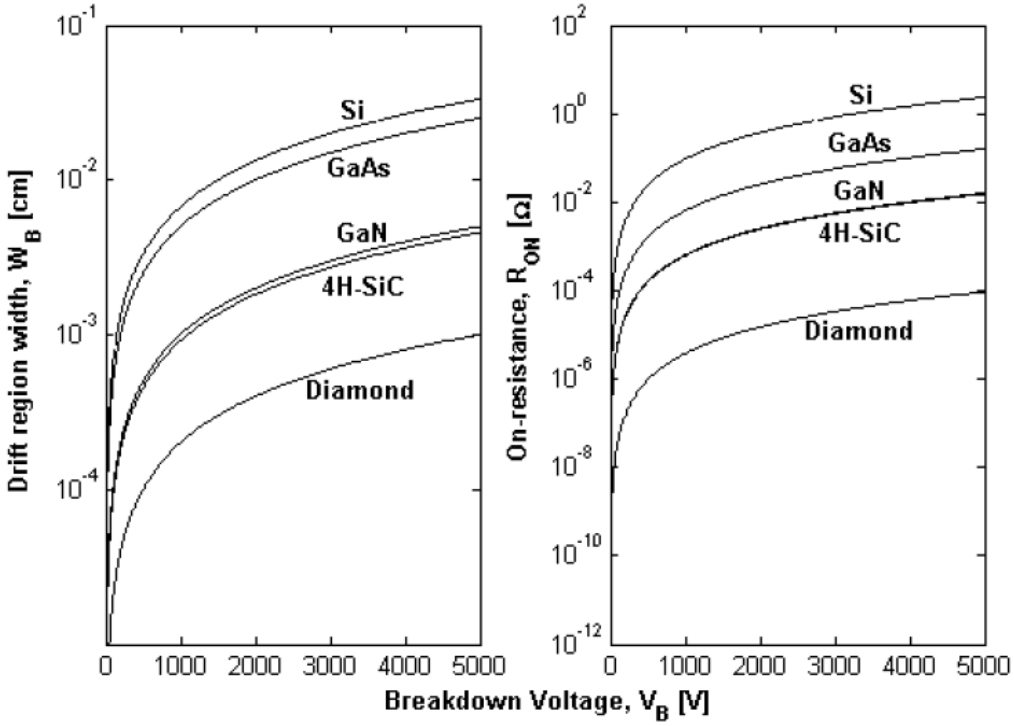

Figure 12. Width (left) and resistance (right) of the drift region vs. breakdown voltage.

- Semiconductors with wider bandgap can operate at higher temperatures.
- Due to the direct proportionality between the high frequency switching capability of a semiconductor material and its drift velocity, it is expected that wide bandgap materials, having more than twice the drift velocity of Si, could be switched at higher frequencies than their Si counterparts. Moreover, higher drift velocity allows charge in the depletion region of a diode to be removed faster, so it is likely that the reverse recovery current of diodes based on wide bandgap semiconductors is smaller and the reverse recovery time is shorter.
- The thermal conductivity does not directly affect the performance, but with a good thermal conductivity it is easier to conduct the heat away from the chip to a heat sink, so it obviates the need to have bulky and expensive cooling systems.

1.4 Carrier Recombination Lifetime

In semiconductor materials the generation of electrons and holes in excess is due to thermal activity, electrical and/or light excitation; opposite to this phenomenon, there is the recombination of such carriers, whose rate can be defined by the following expression:

$$U = \frac{\Delta c}{\tau}$$

with Δc the excess carrier density, and τ the recombination lifetime of such carriers. This latter parameter is strongly related to the crystal quality and defects and, since its value quantifies the effect of different processes which conjointly participate to the recombination phenomenon, it is important to use a complete model that includes all the involved recombination mechanisms to get an accurate estimation of the effective lifetime.

As shown in the following sections, there are fundamentally three recombination mechanisms which occur in semiconductors, with different intensities: radiative recombination, Auger recombination and recombination through defects in the bandgap [23]. Respect to the latter, the first two are band to band, or direct, recombination processes and they depend only on the concentration of free carriers

present in the bulk semiconductor. The free carrier concentrations (electrons and holes) are defined

as:

$$\text{for n - type material} \quad n = n_0 + \Delta n \approx N_D + \Delta n$$
$$\text{for p - type material} \quad p = p_0 + \Delta p \approx N_A + \Delta p$$

where n_0, p_0 are the electron and hole concentrations at equilibrium, N_D, N_A the donor and acceptor doping density, and Δn, Δp the density of electrons and holes in excess per unit volume. At equilibrium, both excess carrier concentrations must be equal, because the generation process involves the creation of electron-hole pairs, i.e., $\Delta n = \Delta p$. Therefore, at given doping density and illumination level mechanisms, the direct recombination processes are exclusively inherent to the material properties: in this case, the only way to reduce the total recombination rate is through the minimization of the number of defects during the manufacture process.

1.4.1 Radiative Recombination

The radiative recombination consists of the annihilation of an electron-hole pair, which leads to the creation of a photon with energy close to that of the bandgap, as shown in Fig. 13.

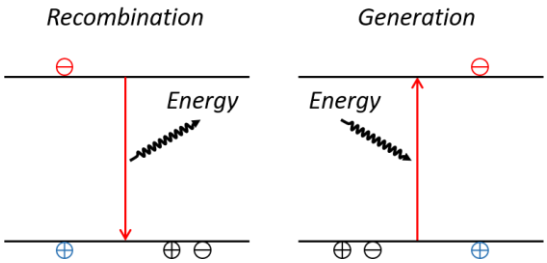

Figure 13. Radiative Generation and Recombination process.

If the carrier has energy higher than that of the bandgap, the excess energy is released as thermal energy to the lattice. The radiative recombination rate depends directly on the availability of electrons and holes, and it is given by:

$$U_{rad} = \beta\,(np - n_i^2)$$

where β is the radiative recombination coefficient. The radiative carrier lifetime results constant at low injection levels, while it is inversely proportional to the excess carrier density at high injection levels, as can be observed combining equation above, which bring to the followings:

$$\tau^{low} = 1/\,\beta N_{D,A}$$
$$\tau^{high} = 1/\,\beta \Delta n$$

Since the Silicon Carbide is an indirect semiconductor, like the Silicon, the radiative process must be assisted by a photon and a phonon to simultaneously preserve momentum and energy. This makes the radiative recombination for SiC much less probable respect to the others recombination mechanisms.

1.4.2 Auger Recombination

Auger recombination, that can be considered as the inverse of the impact ionization process, involves three particles (one electron and two holes, or vice versa). It occurs when the energy released by the recombination of an electron-hole pair is transferred to a third free carrier [24], as shown in Fig. 14. In this process, at low injection level, the expression of the recombination rate is related to the excess

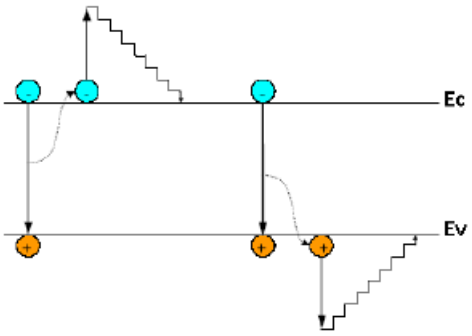

Figure 14. Auger Recombination process.

carrier concentration and to doping density [25]:

$$U_{Auger\,n} = C_n \ \Delta p N_D^2 \quad \text{for n - type material}$$
$$U_{Auger\,p} = C_p \ \Delta n N_A^2 \quad \text{for p - type material}$$

with *Cn* and *Cp* the Auger coefficients for electrons and holes. Therefore, the Auger carrier lifetime at low injection level is given by:

$$\tau_{\text{Auger low}} = 1/C_{n,p}N^2_{D,A}$$

Keeping in count that at high injection levels both carriers participate to the recombination process, the carrier lifetime at these regimes can be expressed as:

$$\tau_{\text{Auger high}} = 1/C_a\Delta n^2$$

where $C_a = C_n + C_p$ is the ambipolar Auger recombination coefficient.

Focused on the evaluation of radiative and Auger coefficients, abundant literature exists for the traditional semiconductors, but this is not the same for Silicon Carbide. By our knowledge, estimated and derived values for 4H-SiC can be found just in [26] they are reported in Table 4, along with values of the traditional semiconductors.

Table 4. Radiative and Auger recombination process for different semiconductors material [27].

	Radiative Recombination Coefficient $\beta[cm^3\ s^{-1}]$	*Auger Recombination Coefficient* $C_{n,p}\ [cm^6\ s^{-1}]$
Si	2.0E-15	C_n=2.8E-31; C_p=1.0E-31
Ge	5.2E-14	C_n=8.0E-32; C_p=2.8E-31
GaAs	1.7E-10	C_n=1.6E-29; C_p=4.6E-31
4H-SiC	1.5E-12	C_n=5.0E-31; C_p=2.0E-31

1.4.3 Shockley-Read-Hall (SRH) Recombination

The recombination through defects in the bandgap is a process which is the dominant recombination mechanism in semiconductors with indirect forbidden bandgap, such as Silicon and Silicon Carbide.

It results explicitly dependent on the number of imperfections in the crystal, caused by impurities or by crystallographic defects, such as vacancies and dislocations. These imperfections originate intermediate states (see Fig. 15) within the bandgap that act as recombination centers, or traps, for the free carriers. The theory for recombination through these localized traps was for the first time analysed by Shockley and Read [28] and then by Hall. Their analytical model which describes the recombination rate (SRH-rate) is given by:

$$U_{SRH} = \frac{pn - n_i^2}{\tau_p (n + n_1) + \tau_n (p + p_1)}$$

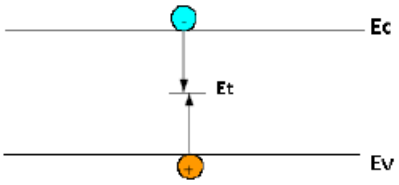

Figure 15. SRH Recombination process.

With $n_1 = n_{ie}\, e^{Et-Ei/KT}$; $p_1 = n_{ie}\, e^{Ei-Et/KT}$ and $\tau_{n,p} = (\sigma_{n,p}\, v_{th}\, N_T)^{-1}$. Here, E_t and Ei are, respectively, the recombination center and the intrinsic Fermi energy levels; Nt is the recombination center density; v_{th} is the electron thermal velocity, and σ_n (σ_p) is the capture cross section, that is an estimation of how much the electron (hole) must be near to the trap to be captured. Since most of recombination centers are close to the intrinsic Fermi level, the previous equation can be simplified in:

$$U_{SRH} = \frac{pn - n_i^2}{\tau_p (n + n_i) + \tau_n (p + n_i)}$$

For conventional semiconductors, the SRH carrier lifetimes in the above equations are modelled as functions of doping and temperature by the following [29].

$$\tau_{n,p}^{SRH} = \frac{\tau_{n0,p0}}{1 + \frac{N}{N_{n,p}^{SRH}}}$$

where N is the total doping density and the other parameters are fitting values, conveniently chosen for considering the process-dependent factors.

At the present, poor contributes are avoidable in literature focused on the estimations of these values for Silicon Carbide, particularly for the 4H-SiC polytype. However, for the $N^{SRH}_{n,p}$, parameters it is typically used value for Silicon [30], i.e., $N^{SRH}_{n,p} = 5\text{x}10^{16}$ cm^{-3}.

1.4.4 Effective Lifetime

With different intensity, depending on the semiconductor topology and technology, all the above recombination mechanisms conjunctly contribute to the final effective carrier lifetime, whose value can be evaluated by the following:

$$\tau_{EFF} = \frac{1}{\tau_{SRH}^{-1} + \tau_{rad}^{-1} + \tau_{Auger}^{-1}}$$

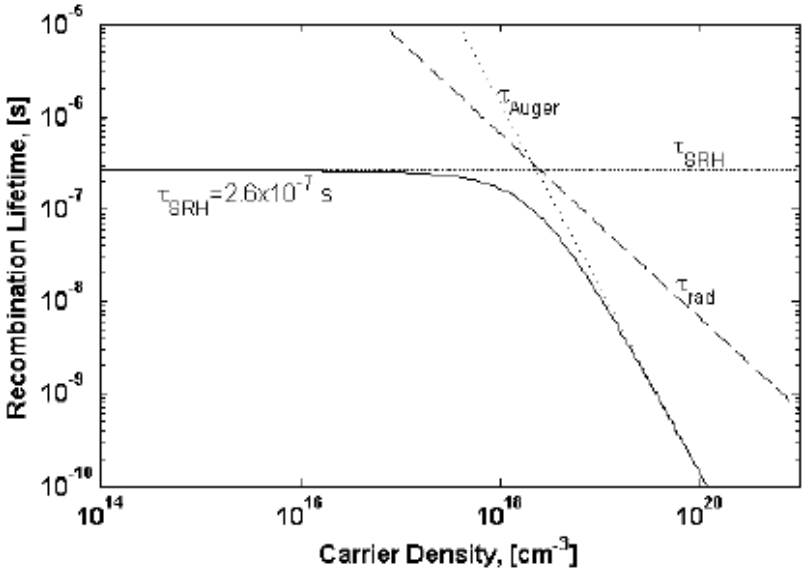

Figure 16. Recombination lifetime in 4H-SiC as a function of the injection level [32].

The 4H-SiC recombination lifetime due to these three components is displayed in Fig. 16: as evident, the Auger recombination is significant only at high carrier densities, while the radiative recombination is completely negligible in Silicon Carbide. There are several experiments over the past few years [31] conducted for investigating the carrier lifetimes for Silicon Carbide.

Since it is an indirect semiconductor, for this material values comparable with those of Silicon are expected in pure crystals, with very low contaminations [32]. At the present, the highest estimated values are up to 2 μs as growth at ambient temperature, which are achieved in thick (40-60 μm) CVD grown epitaxial layers [33].

Because of its high influence on semiconductor performances, the recombination carrier lifetime has been one of the most measured parameters for traditional materials during years. For example, in a pin rectifier, the recombination carrier lifetime is a crucial parameter to predict the performance of the device. In fact, the voltage drop in direct conduction is related to the degree of carrier modulation in the epi-layer, and so it is a function of carrier lifetime and thickness of this region. Therefore, at a given carrier lifetime, a larger epitaxial layer thickness brings to a bigger voltage drop, while a higher carrier lifetime results in better conductivity modulation, with on-state voltage drop approaching the built-in voltage of a $P^{+}N$ junction.

Due to the fragmentary knowledge that is available for the Silicon Carbide, the carrier lifetime is still a crucial parameter, especially for monitoring the semiconductor properties and the device operation conditions. So, it must not amaze the intensive effort made by a lot of scientific works to provide accurate measurement methods for evaluating the carrier lifetime, not only for conventional materials but also for innovative semiconductors, like SiC.

1.5 Epitaxial growth process

Silicon Carbide is interesting on account of its superior properties for high power device applications. The power devices that are of particular interest are devices that can pass large currents in the forward direction and block several hundred volts in the reverse direction. This requires large area devices which makes the demands on the deposition techniques a challenge. The substrate material has in the past recent years improved both in size and quality, however, not sufficiently to process devices directly on them, which puts additional requirements on the quality and uniformity of the epitaxial layers.

Power semiconductor devices have attracted increasing attention as key components in a variety of power conversion units. Realization of high-performance power devices will lead to enormous energy saving, conservation of fossil fuels, and less environmental pollution. Because of the mature technology of Si power devices currently employed in most applications, it is now difficult to achieve innovative breakthroughs in this field. Newly

emerging semiconductors such as silicon carbide (SiC) are attractive for advanced power devices, owing to their superior physical properties, as mentioned before [34] [35] [36] [37]. It should be noted that SiC is an exceptional wide bandgap semiconductor with a very high field breakdown. Furthermore, the doping concentration can be controlled in a wide range, more than five orders of magnitude, for both n-type (N or P doping) and p-type (Al doping). The epitaxial growth technique of choice is chemical vapor deposition (CVD) which has gone through a significant development in the recent decade as the demands on the material quality and throughput increases.

There are two significant reports by Westinghouse on CVD from the 60s by Jennings et al. [38] and by Campbell and Chu [39]. In both studies they used $SiCl_4$ and CCl_4 as precursors, however, Jennings et al. used a vertical cold-wall reactor with the gas inlet at the top and the substrate facing the gas flow and Campbell and Chu used a horizontal cold-wall reactor.

These publications are interesting as they managed to deposit 6H on 6H Si-face Lely platelets. An in-situ hydrogen etch was performed prior to growth. In the report given by Jennings et al. mechanically polished substrates and temperatures above 1725 °C were required to achieve 6H growth. Campbell and Chu, however, produced hexagonal material between 1700 °C to 1730 °C but no growth occurred at higher temperatures. They also produced doped layers using N_2, PH_3, AsH_3, and B_2H_6.

The cold-wall reactor was by far the most common reactor up until the mid-1990s [40], [41] [42] when the hot-wall reactors became popular. The first reactors were normally horizontal with an RF heated graphite susceptor. The gases used were usually silane and propane with hydrogen as gas carrier and the growth temperature were well above 1500 °C. The graphite was normally coated with SiC as the reactions between hydrogen and the graphite otherwise could change the C/Si ratio of the process as well as add a lot of impurities to the growing layer. Typically layers with a background doping concentration around $10^{15}cm^{-3}$ could be obtained but the layers were not very uniform comparing to today's standards.

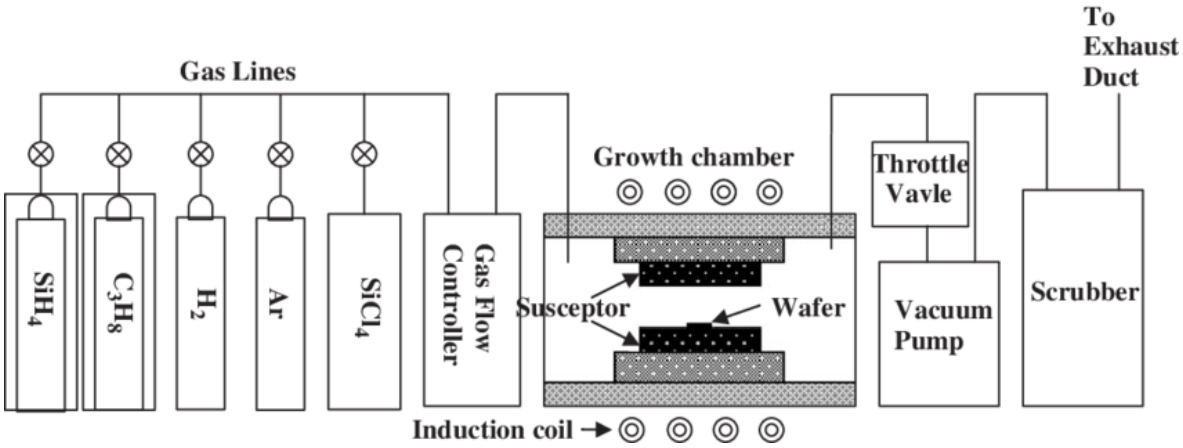

Figure 17. Schematic image of the horizontal hot-wall reactor.

The hot-wall reactor concept was first introduced in 1993 and has since then been scaled and developed [43] [44]. The susceptor normally consist of a top half, a bottom half, and two sidewalls thus providing a rectangular growth chamber (see Figure 17).

The substrate is located on the "floor" of the susceptor, on a rotating satellite or on a load plate located in the center of the gas stream. Thermal insulation is placed around the susceptor to completely block the radiation coming from it to give low energy consumption and uniform thermal fields. Normally, the gases are forced through the rectangular opening using a quartz liner, which gives good utilization of the gases [45].

This type of reactor was a significant step forward in terms of producing high quality material. The material was of substantially better morphology, with a lower background doping, in the low 10^{13} cm^{-3} range, and thicknesses greater than 50 µm could readily be grown. The initial growth rates were in the order of 3–5 µm/h, but they have later been increased to about 10 µm/h after some further development.

Thanks to the low thermal gradient, [46] [47] the backside deposition was not as severe as in the cold-wall reactors and the lifetime of the susceptors could be substantially prolonged. Due to these compelling advantages, the hot-wall reactor has become increasingly popular and is today used by most groups working on SiC.

Recently, high voltage SiC devices with breakdown voltages on the order of 20 kV, have been realized. These new devices include: Double-diffused Metal Oxide Semiconductor Field Effect Transistor (DMOSFET) [48], Vertical Junction Field Effect Transistor (VJFET) [49], PiN diodes [50], and Schottky diodes [51]. These high-power devices can be used, for e.g., the realization of a solid state transformers (SST), [52] one of the key elements of the future power grid where a considerable amount of energy will come from renewable energy resources. Indeed, one of the major challenges to the widespread adoption of renewable

energy is the ability to store and control the wide variety of different energy resources that can have also very different scales: starting from the large-scale centralized installations (such as wind and solar farms) to the small-scale power station of the single house. With SiC high-power devices, it is possible to realize a solid-state transformer that works at high frequency (20–50 kHz), much smaller than traditional transformers and with a much lower switching loss.

To obtain the high breakdown voltages needed for these devices, thick epitaxial layers are necessary for a breakdown voltage between 10 and 11 kV an epitaxial layer thickness of the order of 80–100 µm is needed and the doping density should be in the $10^{14}cm^{-3}$ range [53]. Growing this thick layer with a standard epitaxial growth rate of 6–8 µm/h requires a process time of more than 10 h with a consequently high processing cost. Furthermore, to obtain good wafer yield, on the large devices needed to carry high currents, a low defects density, in both the substrate and epitaxial layer, is required. For the epitaxial layer, it is necessary to realize a process that introduces a low density of stacking faults and point defects/particles. In fact, stacking faults can expand under forward current conduction degrading the on-state characteristics of SiC bipolar devices [54]. Regarding deep traps in SiC, correlation with carrier lifetime has been suggested [55] [56]. Therefore, the reduction of deep traps is also required to realize high-voltage SiC bipolar devices.

A new epitaxial process than overcome some of these limitations have been developed [57] which represent, together with the step-controlled growth mode, a technological breakthrough in SiC epitaxies. In these new processes, the growth rate has been increased with respect to the standard ones by increasing the silane flow combined with the introduction of Chloride-based chemistry, either adding HCl [58] to the Silane precursor or substituting it with trichlorosilane (TCS) [59], [60]. Both processes produced very high deposition rates (>100 µm/h), good surface morphology, high minority carrier lifetime, good thickness, and high doping uniformity.

The key is the shift from Si to $SiCl_2$ as the dominant Si containing species for the growth. While atomic Si is the main chemical species responsible for the homogeneous nucleation of silicon droplets in the gas phase, $SiCl_2$ is very stable and thus remains available to contribute to the film growth while suppressing homogeneous gas phase nucleation of Si during the growth [61].

The Schottky diodes realized on the epitaxial layers grown with this process showed good electrical characteristics and high yield [62], [58] [57] [63]. This process is therefore extremely interesting for high voltage SiC devices with breakdown voltages of about 10 kV.

Another explored approach is based on the use of methyl trichlorosilane as a single gaseous precursor [64] [65]. Using this single precursor growth rates higher than 100 μm/h can be reached with a good quality of the epitaxial layer. Unfortunately, it seems that the use of a single precursor that fixes the C/Si ratio to 1 represents a critical limitation as it is very important to modify this ratio to alter the film doping and the overall quality.

The process with chloride precursors represented a second breakthrough, after the "step-controlled epitaxy," and the main parameters (Si/H_2, C/Si, Cl/Si, growth rate) influence the growth and the quality of the epitaxial layer using these processes. The 4H-SiC epitaxy is still affected by several extended and point-like defects, mainly due to the high defect density of the substrates (mainly dislocations, stacking faults, and surface defects), to the high growth temperatures (which can favour step bunching and particles precipitates) and the peculiarity of the SiC lattice structure (low formation energies for stacking faults and polytype inclusions).

Therefore, it is of paramount importance that for the particular application of the detectors it is necessary to minimize the point defects to increase the lifetime of the minority carriers and therefore to increase the signal collected at the contacts. Furthermore, since the detectors must have very large areas, even large defects (SF, dislocations, triangles, particle and so on) must be reduced as much as possible.

For this reason, it is necessary to grow at a not too high growth rate (60 microns/hour turns out to be better than 90 microns/hour) to improve the lifetime of the carriers. The growth rate must not be too low to attempt to shut down both SFs and BPD.

Furthermore, to avoid the formation of SF from the BPDs present in the substrate, it is necessary to use a thick and highly doped buffer layer to reduce the lifetime in the buffer region and to recombine the carriers in this region and not to allow the formation of SF.

To decrease both triangles and dot defects, a not too low growth temperature should be used. This could result in a fairly rough surface. For this reason, a CMP of the epitaxy surface was also performed.

1.5.1 Defect in SiC Epitaxial layer and carrier lifetime

1.5.1.1 Extended defects

Commercial SiC wafers contain various types of extended defects, as dislocations and stacking faults (SFs), though the defect density has remarkably been reduced in the last decade. Most extended defects in a homoepitaxial SiC layer, which works as an active layer in any SiC power devices, are replicated from the underlying substrate (bulk wafer), but some types of extended defects are generated during the epitaxial growth process [66], some examples are shown in figure 18.

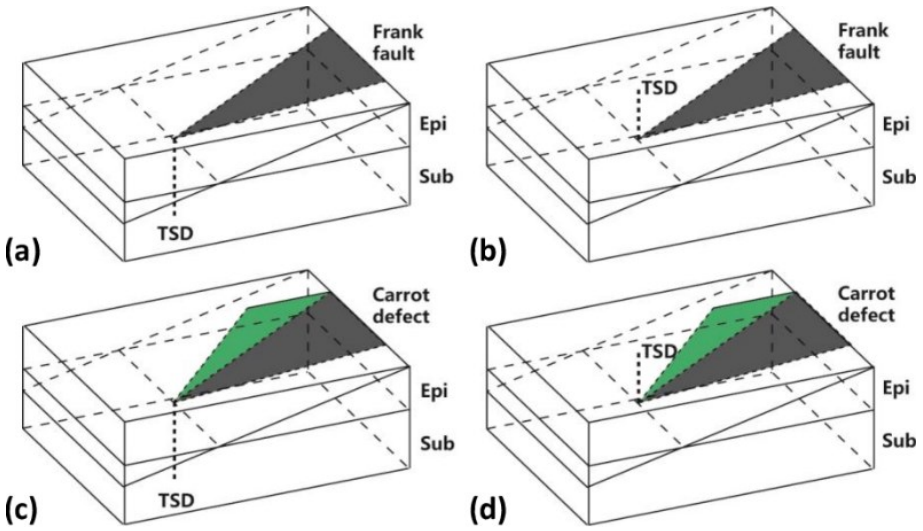

Figure 18. Configurations of intrinsic Frank faults and carrot defects: (a) TSD in the substrate converts to intrinsic Frank fault in the epilayer; (b) simultaneous nucleation of TSD and intrinsic Frank fault in the epilayer; (c) TSD in the substrate converts to carrot defect; (d) simultaneous nucleation of TSD and carrot defect in the epilayer.

Major dislocations present in SiC are threading screw dislocations (TSDs), threading edge dislocations (TEDs), and basal plane dislocations (BPDs), the detail of which is summarized in ref. [67]. Micropipe (MP) defects have been mostly eliminated (density < 0.1 cm^{-2}) and are no longer a primary concern. Figure 19 schematically illustrates replication and

conversion of various dislocations typically observed in SiC epitaxial layers grown on off axis {0001} by chemical vapor deposition process [66] [68].

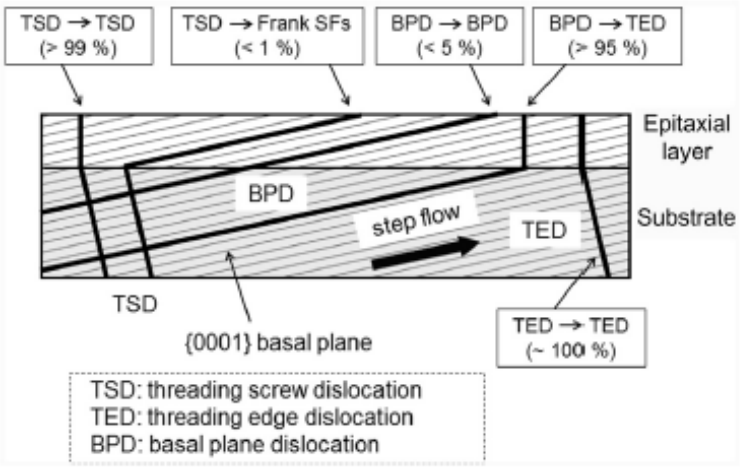

Figure 19. Schematic illustration of replication and conversion of various dislocations typically observed in SiC epitaxial layers grown on off-axis {0001} by chemical vapor deposition [20].

Almost all the TSDs and TEDs in a substrate are replicated in an epitaxial layer. Behaviour of BPDs during epitaxial growth is more complicated. Most BPDs in a substrate are converted to TEDs in the initial stage of epitaxial growth [69] because this conversion results in a substantial decrease of the dislocation length in an epitaxial layer, leading to reduction of total dislocation energy. The BPD-TED conversion ratio is usually high (> 95%) but the ratio depends on the epitaxial growth condition and process (including the in situ etching). The ratio has been improved to 99.9% or higher in recent years and the density of BPDs replicated from a substrate is currently 0.01 - 0.2 cm^{-2}. Although it is hard to observe SFs in SiC wafers, SFs may nucleate during epitaxial growth (especially in the initial stage), which are referred to "in-grown SFs" (IGSFs) [70] [71]. Several IGSFs having different structures (stacking sequences) have been identified, but the nucleation mechanism is still an open question. The IGSF density of high-quality SiC epitaxial layers is below 0.1 cm^{-2}. In addition to common dislocations and SFs, SiC epitaxial layers contain several types of surface morphological defects, most of which accompany some sort of extended defects. These morphological defects are readily discernible by optical microscopy. Such macroscopic defects include so-called "carrot" defects, "comet" defects, "triangular" defect, and "downfalls" [67]. The density of these defects is also dependent on the epitaxial process and the substrate quality, and it is typically 0.1 - 0.8 cm^{-2}.

Table 5 shows the impacts of major extended defects on SiC devices [68]. Though it was believed that threading dislocations (especially TSDs) severely degrade the blocking performance of SiC devices in the early stage, it turned out that threading dislocations in the state-of-the-art SiC wafers are not killer defects when the devices are fabricated by an adequate process [72]. It is crucially important to suppress pit formation at the location where a dislocation appears on the surface.

The superior tolerance of SiC devices against dislocations is most likely due to the extremely low intrinsic carrier density because any carrier-generation current is proportional to the intrinsic carrier density [73]. Since the dislocation density of the state-of-the-art SiC wafers is relatively low (~ 3000 cm^{-2}), the contribution of dislocation-induced leakage is almost hidden by other leakage components. The failure of a gate oxide evaluated by time-dependent dielectric breakdown tests is also not influenced much by dislocations as far as the surface pits are not formed [74].

A BPD is a detrimental defect for any kinds of SiC bipolar devices, because a BPD can work as the source of a single Shockley-type SF upon carrier injection [75], and such an SF induces local reduction of carrier lifetimes (increase of on resistance) and increase in leakage current. This is called “bipolar degradation” and has been a severe obstacle for developing highly reliable SiC bipolar devices.

Although bipolar degradation is not induced during on-state and off-state operation of SiC power metal-oxide-semiconductor field effect transistors (MOSFETs), current conduction through a body diode embedded in the power MOSFET can also initiate the degradation phenomenon.

Table 5. impact of extending defect on SiC devices.

Defect/devices	**SBD**	**MOSFET, JFET**	**PiN, BJT, Thyristor, IGBT**
TDS (without pit)	No	No	No, but causes local reduction of carrier lifetime
TED (without pit)	No	No	No, but causes local reduction of carrier lifetime
BPD (including interface dislocations, half-loop array)	No	No, but can cause degradation of body diode	Bipolar degradation (increase of on-resistance and leakage current)
In-growth SF	V_B reduction (20%-50%)	V_B reduction (20%-50%)	V_B reduction (20%-50%)
Carrot, triangular defects	V_B reduction (30%-70%)	V_B reduction (30%-70%)	V_B reduction (30%-70%)
Downfall	V_B reduction (50%-90%)	V_B reduction (50%-90%)	V_B reduction (50%-90%)

In recent years, this degradation has substantially been suppressed by combination of enhanced BPD-TED conversion during epitaxial growth and introduction of a "recombination-enhancing layer" between the voltage-blocking layer and the substrate [76]. In the case of power MOSFETs, embedding a Schottky barrier diode in the body diode yields a very promising result toward complete elimination of bipolar degradation in SiC power MOSFETs [77].

As summarized in Table 2.4, BPDs, IGSFs, and macroscopic (morphological) defects have been identified as device-killing defects in SiC devices. The total density of these killing defects is typically 0.2 - 0.8 cm^{-2}, which determines a maximum chip area of SiC power devices. To detect and identify these defects in large diameter SiC wafers in a non-destructive manner, a photoluminescence (PL) mapping or imaging technique has been developed [78] [79]. Since each dislocation or SF in SiC epitaxial layers yields PL at a peculiar wavelength, the location and types of individual defects can be easily identified by PL mapping/imaging with an appropriate band-pass filter. With an advanced measurement system, mapping of major defects in a 150 mm SiC wafer can be completed in 30 min or shorter.

During device processing such as ion implantation followed by activation annealing at high temperature, various extended defects are created. Bombardment of high-energy particles in the case of ion implantation naturally causes formation of extended (and point) defects inside and near the implanted region. Furthermore, when the thermal stress caused by an inhomogeneous temperature distribution (and doping-induced lattice mismatch) exceeds a critical value, dislocation glide is activated. Or formation of a BPD half-loop can be introduced from the surface under a large stress. Thus, stress control becomes more and more stringent as the diameter of SiC wafers increases.

1.5.1.2 Point defects

In contrast to the extended defects, all the point defects, which generally create deep levels, in SiC epitaxial layers are independent of the substrate quality and are dominated by the epitaxial growth conditions. The total density of deep levels in lightly doped as-grown SiC epitaxial layers is typically $3x10^{12}$ to $2x10^{13}$ cm^{-3}. This value is low as a compound semiconductor and is well acceptable for fabricating SiC unipolar devices, because the density is much lower than the doping density of a drift layer. For bipolar device

applications, a long carrier lifetime is required, which can be achieved by reduction of deep levels (point defects). Of course, additional point defects are created during device processing such as ion implantation and dry etching. For example, a high density of point defects (mainly intrinsic type defects) is generated inside the implanted region as well as the implant-tail region [80]. Most of these generated point defects are persistent and survive after activation annealing at high temperature.

The energy levels of major deep levels observed in as-grown n-type and p-type SiC epitaxial layers are shown in Figure 20. Among these levels, the $Z_{1/2}$ (E_c -0.63 eV) [81] and $EH_{6/7}$ (E_c -1.55 eV) [82] centers are commonly observed with a highest density in all as-grown epitaxial layers. Both the deep levels are very stable against high-temperature (~1700 °C) annealing. In the lower half of the bandgap, several deep levels such as HK4 (E_v + 1.44 eV) are observed, but these

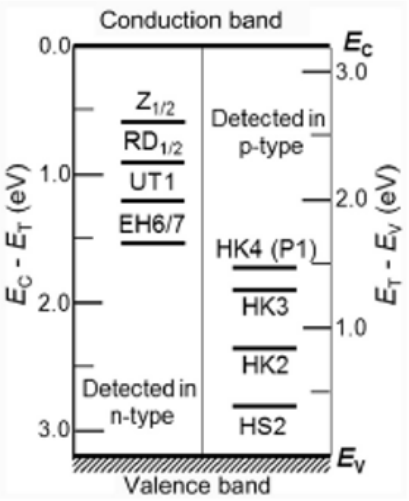

Figure 20. Energy levels of major deep levels observed in as-grown n-type and p-type SiC epitaxial layer.

deep levels disappear after annealing at 1450-1550 °C. As described in the next subsection, the $Z_{1/2}$ center is the dominant carrier-lifetime killer, as confirmed in literature, being the most important deep level in SiC.

The $Z_{1/2}$ center and the $EH_{6/7}$ center are observed with almost identical density in all the SiC samples, and recently the origin of these centers was identified as a carbon monovacancy (V_C) with different charge states [83]. The $Z_{1/2}$ and $EH_{6/7}$ centers correspond to the acceptor-type (negatively charged) and donor-type (positively charged) levels, respectively. The densities of $Z_{1/2}$ and $EH_{6/7}$ centers can be reduced when epitaxial growth is performed under a C-rich condition, as expected. Apart from these intrinsic point defects, a few impurity-

related levels are often observed in SiC epitaxial layers. Boron (B) can be unintentionally incorporated, which results in formation of the boron acceptor level (E_v +0.28-0.35 eV) and the boron-related "D center" (E_v + 0.55 eV) [84]. Another common impurity is titanium (Ti), which creates very shallow electron traps (E_c -0.11/0.17 eV) and probably other deep levels in SiC. The typical B and Ti densities are approximately (1-20) x10^{12} cm^{-3}. The density of other metallic impurities such as iron and vanadium is usually very low.

1.5.1.3 Carrier lifetimes

A carrier lifetime is a key physical property, which determines not only the on-state and switching characteristics of bipolar devices, though it does not matter in unipolar devices such as power MOSFETs but also carrier lifetime and diffusion length for 4H-SiC detectors. The carrier lifetimes in SiC are usually characterized by time-resolved photoluminescence or microwave-detected photoconductance decay (μ-PCD) measurements. The carrier lifetime killer in SiC has been identified as the $Z_{1/2}$ center (acceptor-type levels of carbon vacancy) [85]. Although several other deep levels are present in SiC, the impacts of those levels other than the $Z_{1/2}$ center on the carrier lifetimes are very small. Fig. 18 depicts the inverse of the measured carrier lifetime versus the density of the carbon vacancy defects (half of the $Z_{1/2}$ center density) for 50 μm or 230 μm thick lightly doped n-type SiC epitaxial layers. The inverse of the carrier lifetime is proportional to the carbon vacancy density, when the carbon vacancy density is relatively high (higher than about 1x10^{13} cm^{-3} in the case of 50 μm-thick epitaxial layers). However, the carrier lifetime is governed by other recombination paths when the carbon vacancy density is relatively low. Because of relatively long carrier lifetimes in lightly doped SiC epitaxial layers, the diffusion length of carriers can reach 30-100 μm.

Note that the measured carrier lifetimes are severely affected (underestimated) by surface recombination and recombination in the underlying substrate (or recombination near the interface between the epitaxial layer and substrate). This is one of the major reasons why the linear relationship is lost when the carbon vacancy density is low in Figure 21.

Enhancement of carrier lifetimes can be achieved by reduction of carbon vacancy defects. The carbon vacancy density in as-grown epitaxial layers decreases when the growth is performed under carbon-rich condition. As a postgrowth process for enhancement of carrier lifetimes, a few successful approaches have been established.

In the first technique, excess carbon is introduced by carbon implantation and diffusion of carbon interstitials is promoted by post-implantation annealing [86]. In the second approach, thermal oxidation at high temperature (1300-1400 °C) is effective for carbon vacancy reduction, because some carbon atoms are emitted into the SiC bulk side and diffuse toward a deep region during oxidation [87]. By these techniques, the carbon vacancy defects can be almost eliminated (the density: below $3x10^{10}$ cm^{-3}) from the surface to very deep (100-200 μm) region. It has been reported that annealing with a carbon cap in Ar or annealing in a hydrocarbon ambient is also effective for reduction of carbon vacancy defects in SiC [89]. The carrier lifetime of commercial n-type SiC epitaxial wafers is a few microseconds at room temperature, and it exhibits a gradual increase with elevating the temperature.

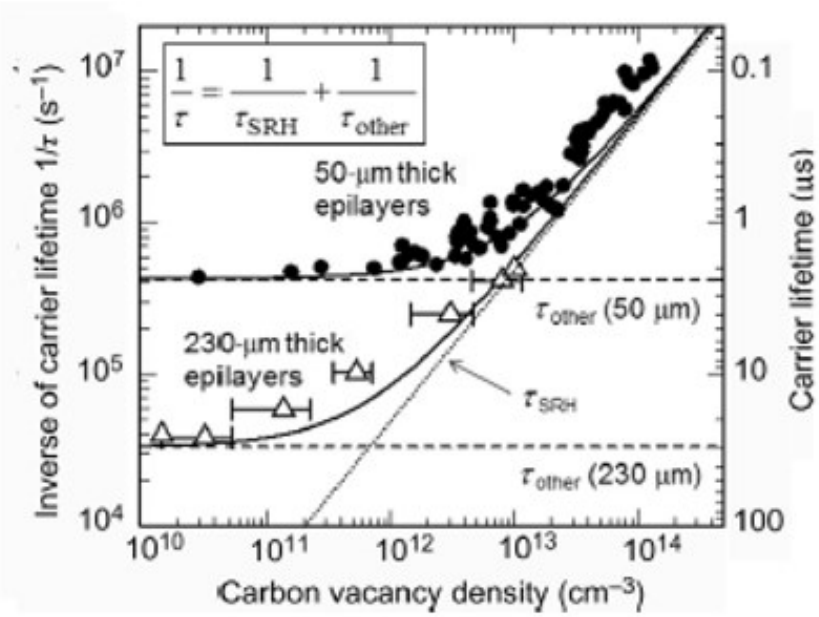

Figure 21. Inverse of the measured carrier lifetime versus the density of the carbon vacancy defects for 50 or 230 um thick lightly doped n-type SiC epitaxial layers [22].

The carrier lifetime can be increased to 30 μs or longer by the carbon-vacancy-reduction process [88]. Although the carrier lifetimes in p-type SiC have been less systematically studied so far, the lifetimes can substantially be enhanced by reduction of carbon vacancy defects as well. Defect passivation by annealing in H_2 at 800-1000 °C is also effective for p-type SiC, leading to a long lifetime over 10 μs [89].

When the doping density or the excess carrier density becomes high, band-to-band recombination and Auger recombination are involved, limiting the bulk carrier lifetime. Recombination of excess carriers in an n-type semiconductor is governed by the following equation [27].

$$\frac{d\Delta n}{dt} = -\frac{\Delta n}{\tau_{SRH}} - B(n_0 + p_0 + \Delta n)\Delta n - C_n(n_0^2 + 2n_0\Delta n + \Delta n^2)\Delta n - C_p(p_0^2 + 2p_0\Delta n + \Delta n^2)\Delta n.$$

Here, Δn, n_0, and p_0 are the excess carrier density, the equilibrium electron density, and the equilibrium hole density, respectively. SRH recombination (τ_{SRH}), band-to-band (direct) recombination (coefficient: B), and Auger recombination (coefficients: C_n, C_p) are considered. By using the band-to-band and Auger recombination coefficients (B, C_n, C_p) reported in literature [90], the decay of the excess carrier density can be calculated and the effective carrier lifetime is extracted.

Figure 22 shows the effective carrier lifetime as a function of the excess carrier

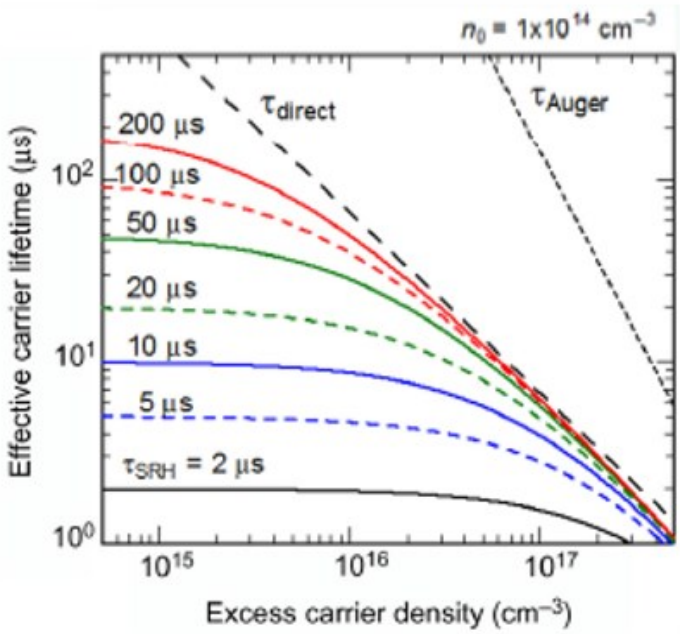

Figure 22. Effective carrier lifetime as a function of the excess carrier density calculated by using the previous Eq. In this case, the equilibrium electron density (n_0) is 1x10^{14} cm^{-3}, and the results for SRH lifetimes varied from 2 to 200 us are shown. The lifetime limited purely by band-to-band and Auger recombinations are indicated by dashed and dotted lines, respectively.

density calculated by using the previous Equation. In this particular case, the equilibrium electron density (n_0) was assumed to be 1x10^{14} cm^{-3}, and the results for SRH lifetimes varied from 2 to 200 µs are shown. In the figure, the lifetimes limited purely by band-to-band and Auger recombination are indicated by dashed and dotted lines, respectively.

As shown in Fig. 22, the carrier lifetimes are limited by Auger recombination when the excess carrier density is very high (> 10^{18} cm^{-3}), and a similar trend is observed in heavily doped SiC. The band-to-band recombination affects the effective carrier lifetime even at a relatively low excess carrier concentration of $1x10^{16}$ cm^{-3} when the SRH lifetime is long (> 50 μs). In such a case, the effective carrier lifetime is mainly limited not by SRH recombination via defects but by band-to-band recombination. Since the excess carrier density in a voltage-blocking layer of bipolar devices exceeds $1x10^{16}$ cm^{-3} at high current density, the lifetimes limited by band-to-band recombination can be one intrinsic performance-limiting factor in high-voltage SiC bipolar devices [91].

2 Chapter 2. Silicon Carbide detectors

2.1 Background

Detection of fast neutrons in SiC detectors is based on the observation of charged-particle products of neutron-induced reactions with silicon and carbon nuclides and other nuclides close to the active volume of the detector as illustrated in Figure 23. Generally, neutron elastic scattering is possible with neutrons of all energies, and other reactions may be possible depending on the neutron energy and reaction energy threshold.

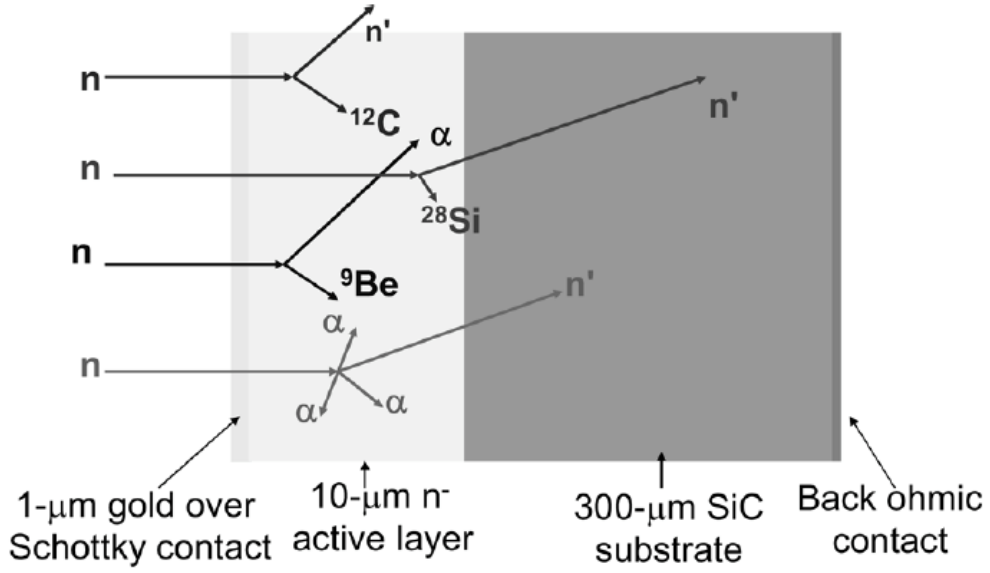

Figure 23. Schematic representation of fast neutron reactions with silicon and carbon nuclides within the active volume of a SiC Schottky diode.

The initial efforts to develop SiC radiation detectors were directed towards neutron monitoring in nuclear reactors [92] [93]. Reactor neutron monitoring must often be carried out in high-temperature environments and intense radiation fields which lead to detector radiation damage concerns. Using crude detectors constructed by applying resistive contacts to SiC crystals, some authors [93] were able to demonstrate detection of alpha particles. In anticipation of the high-temperature monitoring locations that would be encountered in nuclear reactors, these measurements were extended to temperatures up to 700 °C with only minimal changes in the detector response.

In follow-on work [94], a SiC p-n diode coated with ^{235}U was exposed to thermal neutrons in a low-power research reactor. Good agreement was observed between the axial neutron flux profile measurements made with conventional gold-foil activation methods and the SiC

detector measurements. The SiC neutron detector was also shown to have a linear response to reactor power in the 0.1 W to 1 kW range. Detecting the alpha response was observed to be acceptable after a thermal-neutron fluence of 6 x 10^{13} cm^{-2}.

Further development of SiC detectors was hindered by the poor quality of the available SiC materials available at the time. Efforts at developing SiC detectors were renewed by Tikhomirova and co-workers in 1972 [95] [96]. Beryllium diffused 6H-SiC detectors with low, 1 nanoampere leakage currents were shown to be capable of 8% energy resolution for 4.8 MeV alpha particles.

The effects of neutron damage on a ^{235}U-coated, beryllium-diffused 6H-SiC diode were examined. The detector response did not change significantly up to a thermal-neutron fluence of 10^{13} n cm^{-2}. At higher neutron fluences, the detector count rate decreased dramatically. The observed response changes were likely a result of fission fragment induced radiation damage in the detector. The fission-fragment dose corresponding to a thermal-neutron fluence of 10^{13} cm^{-2} is approximately 10^{8} cm^{-2}. Increases in SiC detector leakage currents as a result of neutron irradiation were reported by Evstropov, *et al.* [97]. In the 1990's, long-term development work resulted in the demonstration of technologies for producing high-quality SiC both in chemical vapour deposited (CVD) and large-wafer form. As a result of this development, some of the last major obstacles to commercial fabrication of high-performance SiC semiconductor devices were overcome.

The first use of these developments in high-quality CVD epitaxial SiC detectors was by Ruddy, *et al.* [98]. SiC substrate layers doped with n- donor atoms (nitrogen) were overlayered with a lightly doped epitaxial layer containing a nitrogen concentration of 10^{15} cm^{-3}. The epitaxial layer thicknesses ranged from 3 μm to 8 μm. Detectors with 200 μm and 400 μm diameters were tested. Although detectors with diameters up to 1 mm were fabricated, the presence of defects in the form of micropipes limited the performance of detectors with diameters greater than 400 μm. Nickel Schottky metal contacts covered by gold were applied to the epitaxial layers to form Schottky diodes, and thin (1 μm) p^{+} layers were applied to the n- epitaxial layers to form p-n junction detectors. Both the Schottky diodes and p-n junctions were demonstrated as alpha detectors with ^{238}Pu sources. No drift in the pulse-height response was observed in the temperature range from 18 °C to 89 °C. Similar results were reported by Nava, *et al.* [99]. Alpha-particle response measurements were carried out for ^{241}Am using Schottky diodes fabricated on 4H-SiC epitaxial layers. Charge-carrier collection efficiency was shown to increase linearly with the square root of the detector reverse bias. Rapid development of epitaxial SiC ensued leading to the

development of high-resolution SiC alpha detectors (Ivanov, *et al.*, 2004; Ruddy, *et al.*, 2009b), high-resolution and temperature insensitive X-ray detectors [100] [101] and detectors for minimum ionizing particles [102] as well as neutron detectors.

2.2 Charge particle detectors

The 4H polytype produces most of SiC-based radiation detectors, with Schottky contacts being the most common. When a reverse bias is applied (negative bias) between the Schottky (or p contact) and the ohmic contact, the region of the epitaxial layer depleted from charge carriers forms the active layer of the detector. The thickness (d) of the latter is determined by the applied bias (V) and doping concentration (N) as follows:

$$d \cong \sqrt{\frac{2\epsilon\,(V_{built-in} + V)}{eN}}$$

where e is the electron charge, $V_{built-in}$ the junction barrier height, and ϵ the SiC dielectric constant. It is clear from this relationship that there are two ways to thicken the active layer. One is to increase the reverse bias, though this solution might be constrained by an upper limit (~ 1000 V) in order to protect the electronic chain and the bonding wires from discharges. The other option is to reduce doping levels. Nowadays, the minimum doping concentration achievable by state-of-the-art SiC epitaxy is about 10^{13} Nitrogen/cm^3 [103].

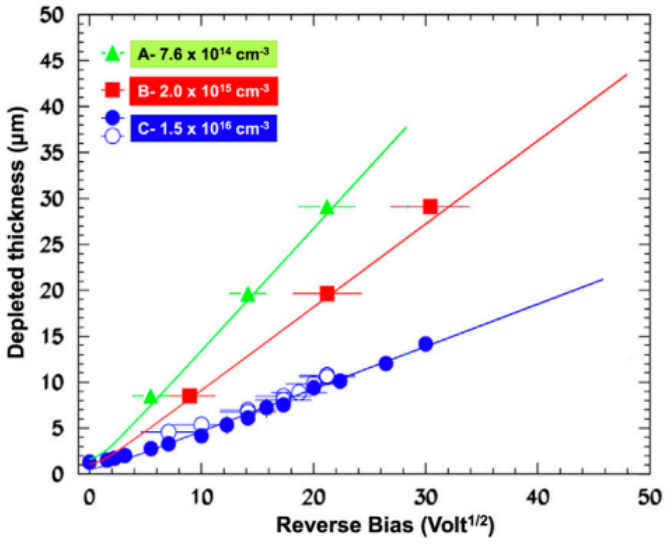

Figure 24. Thickness of the depleted epitaxial layer as a function of the applied voltage [104].

Figure 24 shows the thickness of the depleted region as a function of square root of the reverse bias for three 4H-SiC Schottky detectors with different epitaxial layer doping concentrations. The bias needed to deplete the same thickness is lower for lower doping concentrations, as expected from the previous equation. It is worth noticing that the biases needed are quite high, 400 V to deplete only 30 μm of the lightest doped sensors.

2.2.1 Electron detection

Different works have investigated the response of SiC detectors to electrons, when used as MIP (Minimum Ionizing Particle) detectors. For MIP, the various measurements point to a quantity of produced electro-hole pairs (e-h) on the order of 50(e-h)/μm. In previous works [105] [106] the authors investigated the signals of 2.2 MeV electrons generated into 4H-SiC p-n junctions and Schottky barrier, respectively, using a ^{90}Sr β source. Detectors based on n-type, $6x10^{13}$ cm^3 doped, and 40 μm (nominal) thick epitaxial layers were used in the latter case. In Ref. [107], the charge collected as a function of the applied bias is reported in electron charge units. A bias of ~60 V saturates the collected charge. The latter is about 2090*e* corresponding to 55 ± 3(e-h)/μm. A consistent value (51 e/h) is found in Ref. [108], which used semi-insulating 300 μm thick 4H–SiC detectors with ohmic contacts to test them with a ^{90}Sr β source. For a reverse voltage of 500 V, a response of approximately 2000e has been measured. Nonetheless, the high density of deep level defects generates a large number of trapping processes, causing the signal to decay rapidly to 800e with a decay constant of 14 min. Bruzzi et al. [102]] used a 0.1 mCi ^{90}Sr source to test the charge response of 4H-SiC Schottky barriers. Epitaxial layers with an effective doping concentration and maximum active thickness of $6.1x10^{14}$ cm^3 and 20.8 μm, respectively, were used, as determined by C-V analysis. In the range of 0–250 V, the pulse height spectrum is measured as a function of the reverse voltage. A bias of ~240 V saturates the collected charge at around 1100e, which corresponds to 51(e-h)/ μm, which is consistent with the results of the previous measurements. Minority carriers also contribute to the signal. The minority carrier diffusion length measured at zero bias is $L_p \sim 4$ μm.

2.2.2 Proton, alpha and heavy ions detection

During the last two decades, SiC Schottky barrier detectors have been extensively studied as ionizing radiation detectors with protons, alphas, and heavy ions. In this section, the research work of note and corresponding outcome are summarized. Even though the performance of such devices depends on their design, some general conclusions can be drawn from the literature.

Linearity. High degree of linearity between the incident energy of the radiation and the collected signal. In Ref. [109] the response of the detectors is found to be linear as a function of the proton energy. The authors also extracted the average energy *En* needed to generate e-h pairs. The value of *En* is related to the energy of the incident particle (E) and the average number of pair (N_{eh}) created in the active volume of the detector by $En = E/N_{eh}$. E is evaluated considering the energy lost in the detector entrance window and N_{eh} is inferred by measuring the total collected charge $Q = qN_{eh}$. Using a standard Si detector as reference and assuming $En_{Si} = 3.64$ for protons, En_{SiC} for protons is found to be 7.78 eV.
Recently, Bernat et al. [110] also found an high degree of linearity as a function of incident energy up to 6.7 MeV, the maximum energy that allows α to stop within the thickness of the SiC epitaxial layer.

Charge collection efficiency. SiC Schottky diodes can provide 100% Charge Collection Efficiency (CCE). It is worth mentioning the recent work of Ref. [111] on Ni/SiO_2/n-4H-SiC vertical MOS (metal-oxide semiconductor). Despite the presence of the oxide layer, the detectors showed a high CCE of 96% at 40 V (detector depleted to 18 μm, almost equal to the alfa range). The drift-diffusion model discussed above gives a $L_p = 24$ μm.

Energy and time resolution. When the particle range in the detector is longer than the depleted layer, a contribution from minority carriers is observed in the signal. Energy resolution as a function of the applied bias is measured by M. De Napoli et al. in [112]. Increasing the bias improves the energy resolution significantly. It varies slightly depending on the doping concentration, and as expected, less doped SiC detectors have better resolutions due to a lower defect concentration.
Kleppinger et al. [113] measured an energy resolution lower than 0.5% at 200 V in their thick detectors. Chaudhuri et al. [111] reported the highest energy resolution ever measured

on SiC-based MOS detectors: 0.42% for 5.48 MeV alpha particles. Although good, in general MOS detectors do not yet have the same energy resolution as Schottky barrier detectors. The reason for this is that lifetime killing defects like $Z_{1/2}$ and $EH_{6/7}$ typically have a much higher concentration (at least one order of magnitude).
Moreover, excellent timing properties have been proved with time resolutions as high as 117 ps.
Spectroscopic performances comparable to standard Si detectors have been observed with energy resolutions below 0.5% and up to 0.25% (FWHM) for ~5.5 MeV alpha particles.

2.2.3 UV and X/γ-Ray detection

Pin photodiodes and avalanche photodiodes (APDs) are the most common SiC photodetectors. A pin photodiode can have the following basic structure: the active region is formed by the growth of an n-doped layer on a n^+ substrate, which is in contact with a thin heavily doped p^+ layer forming the diode junction. The p^+ layer's metal contacts are spaced apart to allow light to pass through, and the surface is coated with an antireflective coating. Photogenerated primary carriers are accelerated in APDs, resulting in secondary ionization and signal amplification. Usually, the choice falls on the further acceleration of holes instead of electrons due to their higher ionization coefficient. For this purpose, an additional thin and heavily doped n layer is included through the n-collection region to generate a region of high electric field where accelerated charges produce secondary ionization.
The results obtained by several works [114] [115] show the excellent noise performance of 4H-SiC APDs, indicating that 4H-SiC is an ideal semiconductor for low noise APD fabrication.
Moreover, many studies on the response of SiC detectors to X- and γ-rays have been conducted. Different detector structures have been investigated depending on the type of application, ranging from spectroscopy to beam monitoring and dosimetry: traditional Schottky diodes, microstrips, pixel, and very thin layers. Some general conclusions can be drawn from this diversity:

• In terms of x-γ adsorption, 4H-SiC Schottky barrier detectors with active layers as low as 16 μm thick are sensitive to electromagnetic radiation up to 59.6 keV.
• Energy resolutions as high as ~ 3.6% at 5.9 keV can be achieved

• SiC detectors can measure high-resolution X-ray spectra at high temperatures (up to 100°C) and during temperature changes.
• In terms of transparency, linearity, dynamics, and signal to-noise ratio, SiC devices have shown comparable or even better performance than commercial polycrystalline diamond as X-ray beam monitors.
• In vivo dosimetry is another field where SiC-based sensors have comparable performance to commercial diamonds.

2.3 Silicon Carbide neutron detector

The structures of the devices typically used for the realization of a detector are semiconductor junctions (p^+/n, n^+/p, or $p^+/i/n^+$) which operate in reverse polarization. A space charge region is formed and the p^+, n^+ regions or the metal layer act as electrodes. The lowest concentration of impurities and defects is required to avoid a reduction in the amplitude of the current signal due to the recombination of the electron-hole pairs. The wide bandgap of SiC leads to a significant reduction in the rate of carriers thermally generated, reducing the leakage current and the noise level. Additionally, SiC detectors still have a high signal-to-noise ratio (SNR) at higher temperatures than Si devices, unless external cooling is used to reduce the intrinsic carrier level.
Radiation damage can affect various properties of a detector, such as leakage current and charge collection efficiency (CCE), due to the removal of free carriers from the active region of the device. The radiation hardness is, therefore, an important parameter to consider for detectors [116].
Due to its wide bandgap and chemical bonds, silicon carbide has been considered an alternative to silicon to produce hard radiation detectors.
SiC neutron detectors are usually based on Schottky or p-n diodes. A schematic drawing of a SiC Schottky diode detector is shown in Figure 24. The SiC substrate layer consists of high-purity material containing a residual n^+ doping concentration that is typically about 10^{18} cm^{-3} of nitrogen. The epitaxial layer is applied to the substrate layer and contains a much lower nitrogen concentration, typically 10^{14} – 10^{15} cm^{-3}. Lower n^- concentrations are necessary if the thickness of the epitaxial layer is greater than 10 μm in order to limit the voltage required to fully deplete the layer and collect the radiation-induced charge from this layer. An ohmic back contact and a Schottky front contact are applied. The front contact

typically consists of a thin layer of titanium or nickel (~800 Å) covered by thicker layers of platinum (~1000 Å) and gold (~9000 Å).

The thicker layers are needed to protect and ruggedize the Schottky metal layer. The optional convertor layer is used to obtain increased neutron sensitivity.

The field of application of solid-state detectors with wide band gap is expanding in those environments where high neutron flux is a problem, such as high flux neutron sources and thermonuclear fusion environment. To date, the best detectors in this field are diamond based, Single-Crystal Diamond (SCD), with important performances, but the high costs and limited availability of large commercial monocrystalline diamonds has led to the development of alternative materials for such purposes. Good quality SiC detectors are now available and fast measurement of the neutron spectrum is possible even at high temperatures such as with diamond detectors.

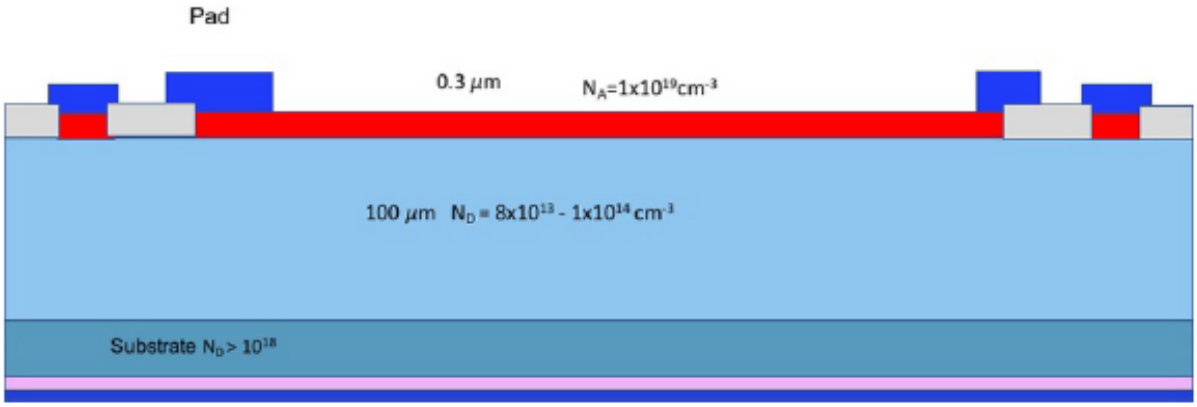

Figure 25. Detector layout in SiC.

Today SiC can be produced on relatively large areas (up to 1.5 cm^2), with thicknesses up to 250 μm and with a low number of defects per cm^2, which represent an excellent improvement in the growth technology of this material [10]. This allows the use of these detectors in environments where fast neutron spectroscopy with high count rates (up to 1 MHz) is required such as in fusion plasmas. Indeed, due to the short time scales of the phenomena that can occur in fusion plasmas (typical time scales of the order of tens of ms), the ability of a high count is critical.

Neutron detection with SiC is based on the collection of electron-hole pairs produced by charged particles generated by the interaction of neutrons with the C and Si nuclei, the group

of reactions are shown in the Table 6, and they represent the possible reactions for fast neutrons with Energy of 14.1 MeV on a SiC detector [117].

At the high energy range pertaining to fast neutrons, several neutron-induced threshold reactions directly with the Si and C atoms of the detector become viable. These reactions lead to the creation of ionizing particles within or close to the detector active volume which carry part of the kinetic information of the incoming neutron thereby enabling neutron detection and, to some extent, neutron spectroscopy.

Neutrons, as well as the charged particles produced in the converter layer (which is often used on the top of the detector to enhance the neutron detection), can cause damage. The latter appears to be more severe than γ damage in SiC detectors. Several different studies have been conducted by various groups. Ruddy et al. [118] recently published a review on the subject.

In general, at fluences of the order of 10^{11} n/cm^2, SiC detector performance begins to deteriorate due to epithermal/fast neutron irradiation [119] [120]. However, no significant CCE degradation is expected. Radiation effects become important at fluences greater than about 10^{14}–10^{15}n/cm^2, resulting in an acute degradation of the CCE and a reduction in e and h drift length. However, even after a fluence of 1.7 x 10^{17} n/cm^2 some detectors have been found to still work [107]. Cases where SiC becomes semi-insulating at fluences of 4 x 10^{14} n/cm^2 have been reported [107]. The effect is caused by electrons being trapped in radiation-induced deep level defects.

SiC UV-photodiodes with drift layer doped less than 1 x 10^{15}cm^{-3} preserve their performance up to fluence of 5 x 10^{12} (fast-neutrons)/cm^2. Elevated temperatures during irradiation attenuate the effects of the radiation damage on CCE, opening the possibility of using SiC neutron detectors in high temperature environments.

Table 6. Fast neutron-induced reactions in Silicon Carbide.

REACTION	Q Value (MeV)	Energy Threshold (MeV)
$^{12}C(n,n')^{12}C$ ground state	0	0
$^{12}C(n,n')^{12}C$ 2+	-4.4389	4.8088
$^{12}C(n,\alpha)^{9}Be$	-5.7012	6.4196
$^{12}C(n,n')3\alpha$	-7.3666	8.4286
$^{12}C(n,p)^{12}B$	-12.5865	13.7401
$^{28}Si(n,n')^{28}Si$ ground state	0	0
$^{28}Si(n,n')^{28}Si$ 2+	-1.7790	1.8425
$^{28}Si(n,\alpha)^{25}Mg$	-2.6537	2.7653
$^{28}Si(n,p)^{28}Al$	-3.8599	4.0042

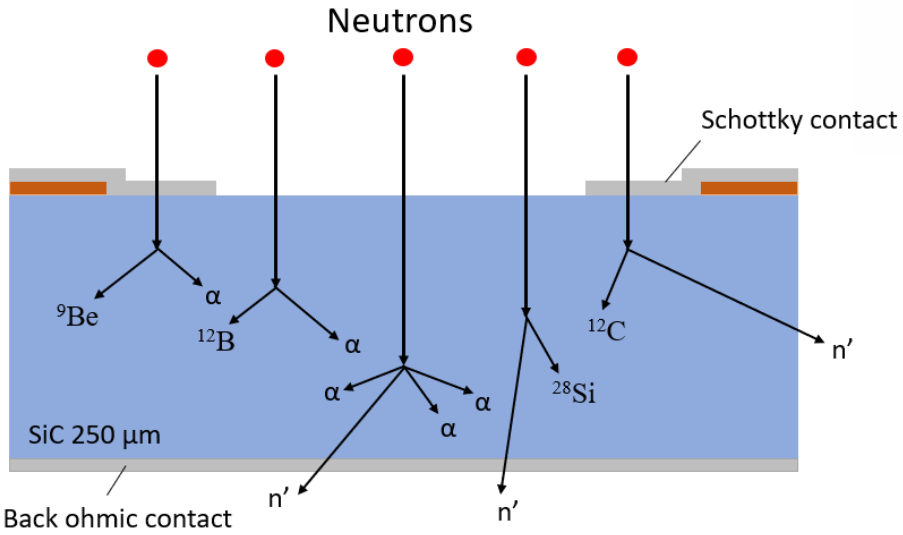

Figure 26. Scheme of the common interactions that take place on the epitaxial layer of our SiC devices.

As described in table 6, the neutrons in the case of SiC reacts with both Silicon and carbon unlike the diamond detectors (most used on this field) where are present just carbon atoms. The list includes only the most prevalent fast-neutron reactions in SiC and Figure 26 shows the interaction scheme. Other more complex reactions resulting in the emission of two or more particles will also occur. Also, reactions are listed only for the most abundant Si and C isotopes in the natural elements. Silicon consists of 92.23% ^{28}Si, 4.87% ^{29}Si and 3.10% ^{30}Si. Carbon consists of 98.90% ^{12}C, 1.10% ^{13}C and a negligible amount of ^{14}C. Fast-neutron reactions similar to those listed above can occur with the less abundant isotopes.

Two of these reactions listed include elastic and inelastic neutron scattering. In elastic scattering, the neutron interacts with the target nucleus and transfers a variable fraction of its momentum while preserving the overall kinetic energy of the two particles. In inelastic scattering, the neutron elevates the target nucleus to an excited state and transfers momentum without preserving the kinetic energy of the system. The ^{28}Si or ^{12}C recoil atoms are energetic

charged particles, which can produce ionization in the active layer of the SiC detector. The secondary neutrons resulting from these reactions however generally escape from the system before inducing any further reactions due to the combined effects of low cross sections and small detector volume. In both elastic and inelastic scattering, the amount of kinetic energy transferred to the ionizing particle is not fixed and a continuum of recoil ion energies will result in the response. While this continuum makes fast-neutron detection still possible, it will not convey an adequate amount of information to infer the energy of the incoming neutron.

The other reactions listed result in charged particles, which will all produce ionization in the detector active volume. If the incident fast-neutron energy is monoenergetic, these reactions will produce a fixed response, and a peak will be observed in the pulse-height response spectrum.

SiC has begun to compete with diamonds in terms of energy resolution and sensitivity in fast neutron detection. In thermal neutron detection, an excellent degree of γ discrimination has been recorded, with ~ 100% sensitivity to neutrons.

Tests were carried out using a SiC detector in comparison with a SCD (Fig. 27) irradiated with 14 MeV neutrons [8]. It was experimentally obtained that the detector, with an active area of 25 mm^2 and an epitaxial thickness of 100 μm, showed good efficiency thus demonstrating the improvements made to the epitaxial growth procedures. The absence of instability during irradiation, up to a neutron fluence of 14 MeV of 4.45 x 10^{11} n/cm^2, suggests a direct use of this detector for rapid neutron detection. Obviously, the performance of the best devices such as the diamond ones is not yet reached, but we are working in the right direction, in order to improve the resolution.

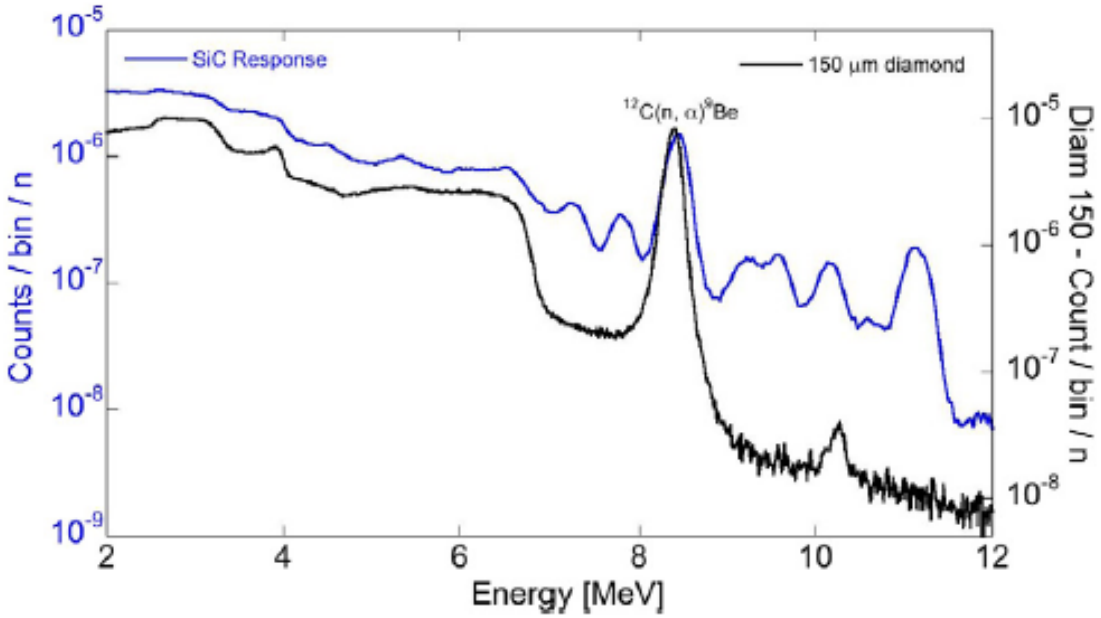

Figure 27. Comparison spectra between diamond (150 um) and SiC (100 um) detectors under working condictions.

From the first results obtained on SiC neutron detectors it is evident that it is necessary to increase the thickness of the epitaxy compared to that used in the first experiment (100 microns). In fact, from the comparison with the diamond detectors it was observed that, while compared to the 150 microns diamond detectors the detection efficiency is comparable to that of the 100 micron SiC detectors, the efficiency of the thicker diamond detectors (500 microns) is higher.

This hypothesis is supported by investigations through simulations using the Monte Carlo software Fluka [121]. A parallelepipedal telescopic detector with a base surface of 25 mm^2 was simulated. In the first study of simulations the SiC interactions with neutrons has been studied and compared with Silicon and Diamond detectors, with the same geometric features [122]. From these simulations reported in Fig. 28a it is possible to observe that the interacting neutrons are much higher in Diamonds with respect to SiC and Silicon because the scattering cross section of carbon is higher than that one of silicon. After that the active area of the SiC detector was increased and with this doble area the interacting neutrons are comparable between the diamond and the SiC detectors. This result is extremely interesting because the better material quality of the SiC material with respect to diamond can give the opportunity to obtain larger devices and then a comparable or better efficiency. Of course, the area of the detector cannot be increased over a certain value because the increase of the area also produces a considerable decrease of the detector production yield, with a subsequent increase of the detector costs.

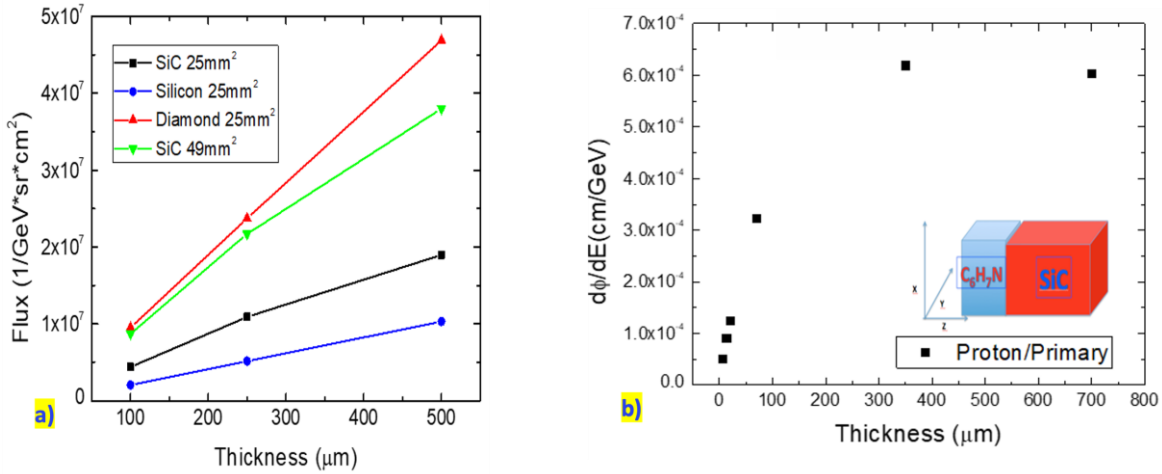

Figure 28. a) Flux versus thickness for different materials (Diamond, Silicon and Silicon Carbide) at different thicknesses (100, 250 and 500 um); b) Differential protons Flux versus thickness of aniline (7–14–21–70–350 e 700 μm), for bitelescope Aniline + SiC.

It was therefore decided to increase the thickness and the area of the detector in order to obtain a greater detection efficiency. As a matter of that, the efficiency of the diamond is higher for the same thickness compared to Si and SiC. By doubling the area of the SiC detector it is possible to obtain the same efficiency as the diamond.

To obtain thicker detectors, it's possible to follow two paths: on the one hand, use semi-insulating substrates that have a thickness of 500 microns, or try to increase the thickness of the epitaxy.

The use of semi-insulating substrates presents two main problems. On the one hand, the high density of point defects determines a low average carrier lifetime in the material, reducing the carriers collected. In addition, the very low concentration of carriers determines a significant lateral depletion that even reaches the limits of the die. To try to overcome these problems, a suitable edge structure could be studied that allows to limit the depleted area laterally and at the same time allows to apply high voltages in reverse polarization. In this way, the effect of the low average lifetime of the material could also be reduced.

In all the materials, as reported in Fig. 28, the interacting neutrons increase by increasing the thickness of the detectors, but very thick detectors are difficult to be realized due to the increase of defects density in very thick epitaxial layers [123] [124]. Furthermore, a higher bias is needed to deplete the thick epitaxial layer as shown in Fig. 29a. To decrease this high voltage, it is possible to decrease the doping concentration in the epitaxial layer, but in the case of silicon carbide is extremely difficult to reach doping concentration lower than $1x10^{14}/cm^3$.

Another aspect that should be taken under consideration is that when we use very thick epitaxial layers for the detectors, we need to have a diffusion length larger than the depleted layer to have a good charge collection. From Fig. 29b it is possible to observe the diffusion length data, calculated using time resolved photoluminescence (TRPL) for the lifetime calculation.

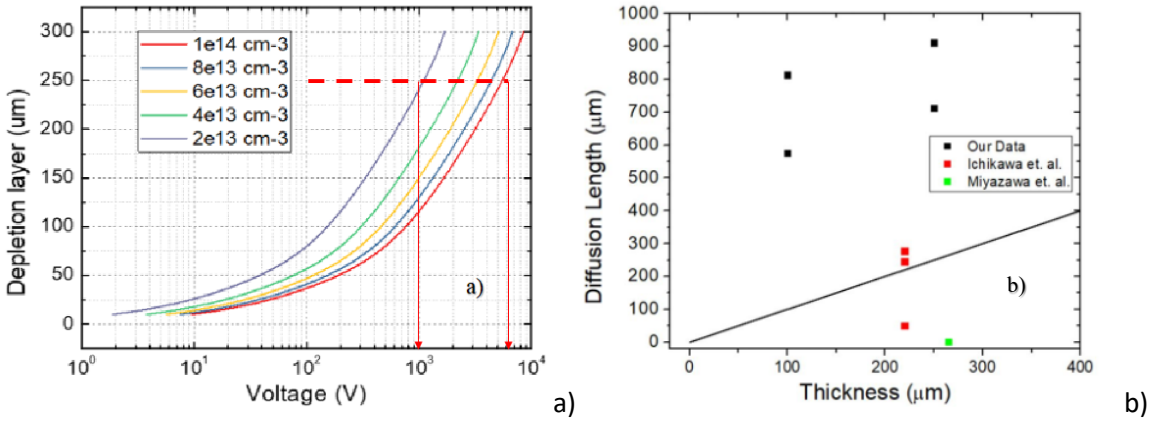

a) b)

Figure 29. a) Depletion layer thickness versus applied voltage for different carrier concentration, the dashed line and arrows refer to the voltage necessary to deplete our epilayer; b) Diffusion length as a function of the thickness for our data compared with data in literature [125] [126].

The diffusion length values are higher than the epi-layer thickness for our samples [127] with an optimized epitaxial process, while in the case of other epitaxial growth processes, the diffusion length is close to thickness of the epitaxial layer or even lower. Then with a good epitaxial process the diffusion length does not seems to be the limiting factor in the increase of the epitaxial layer thickness and of the neutron sensitivity. Instead, the high voltage necessary to deplete a thick epitaxial layer, and the low yield of the very thick detectors with large area are the main limitation of this technology. Indeed, to obtain the maximum efficiency of the detector it is necessary to deplete the entire area. The voltage at which a given thickness depletes strongly depends on the doping level of the epitaxy. Therefore, to have low depletion voltages it is necessary to have low doping. This problem currently limits the possibility of using SiC detectors with thicker epitaxial layers.

3 Chapter 3: Characterization and carrier lifetime evaluation of epilayer

As previously described, the fundamental parameter necessary for the for the good functionality of the detectors is the epitaxial layer quality, which is the active area of the detectors. Therefore, it is important to characterise the epi-layer in terms of SF or point defects, carrier lifetime and diffusion length.

Almost all the material characterization techniques commonly used are applicable to SiC although special care is often required. The major points that are unique to SiC characterization are summarized

as follows:

1. *Sample structures:* Characterization of properties or defects in SiC epitaxial layers is often intended because they are likely to be directly linked to the device performance. However, SiC epitaxial layers are often relatively thin (5–10 µm), and the influence of the underlying substrates therefore cannot be neglected. Thus, it is important to be aware of the thickness that is monitored by each individual characterization technique. The effects of the substrate must often be considered even when the epitaxial layers are relatively thick (100–250 µm). In addition to the thickness, the area is also important, in fact as the size of the detector increases, the yield for material defects decreases (Figure 30). With the improvement of substrates and epitaxy processes it is possible to lower defects and improve yield.

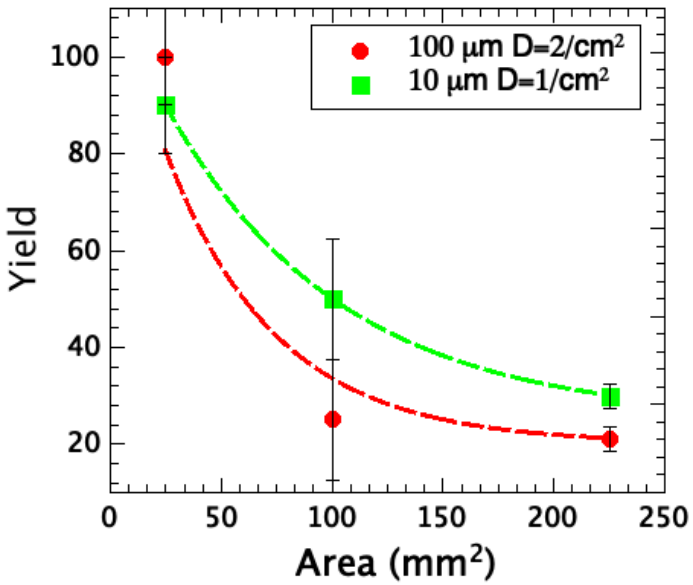

Figure 30. Detector yield as a function of the detector area (mm²).

2. *Wide bandgap*: When optical excitation is required during characterization, the conventional systems that were designed for characterization of other semiconductors as Si and GaAs must be modified substantially. For example, ultraviolet light with a wavelength that is shorter than 370 nm is required as an "above-bandgap" excitation source (e.g., lamp, laser) to characterize 4H-SiC at room temperature. Because SiC has an indirect band structure, the optical absorption coefficient is small, even when the photon energy is considerably larger than the bandgap (Figure 31). Also, when thermal excitation is used in the characterization process, very high temperatures (>450 °C) are required to monitor the mid-gap states because the bandgap of 4H-SiC is approximately three times larger than that of Si.

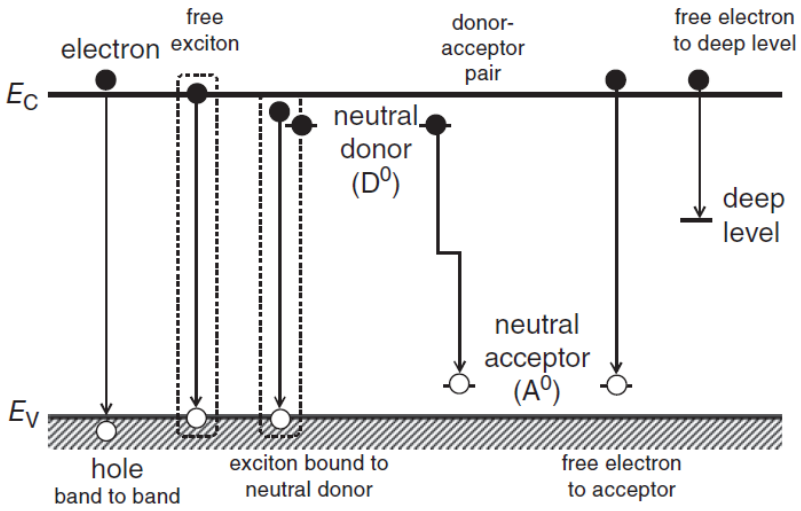

Figure 31. Schematic illustration of typical recombination paths of excess carriers in SiC [128].

In this section, the major techniques that can be used for characterization of the physical properties and detection of the defects in SiC are briefly introduced, together with the results obtained from samples characterization.

3.1 Characterization techniques

3.1.1 Photoluminescence (PL)

Low Temperature Photoluminescence or LTPL is an optical spectroscopy technique considered as the most informative tool for qualitative characterization of semiconductor thin films. In the case of SiC layers, LTPL spectrum allows the polytype identification and provides information about the impurities and defects presented into the material. It is considered as a non-destructive technique that does not require any sample preparation. Although, if the cryostat size is smaller than the wafer diameter, the cut of the wafer is necessary, disregarding it as a routine technique. Also, a quantitative evaluation of the impurity concentration can be extracted after the correlation between intrinsic and extrinsic emissions. In this thesis a room temperature photoluminescence apparatus was used in order to evaluate the general status of epitaxial layer and for the defect characterization.

Photoluminescence (PL) is one of many forms of light emission from the material. In PL, the light emission is initiated by photoexcitation: the electrons are excited from their ground state by an excitation source (usually a laser) with certain photon energy, creating electron-hole pairs or excitons. To reach back the equilibrium state, radiative and non-radiative recombination of the electron-hole pairs take place.

Since the SiC is an indirect band gap semiconductor, the recombination of electron-holes pairs occurs only assisted by one or multiple momentum conserving phonons. Furthermore, contrarily to direct band gap semiconductors where the PL measurements can be performed at room temperature, the analyses on SiC layers have to be performed at low temperatures (e.g., in the range 2-5 K) in order to obtain the resolution and intensity high enough to correctly interpret the spectra [129].

The radiative recombination of electron-holes pairs includes the intrinsic radiative recombination observed in high purity materials and the extrinsic radiative recombination related to the presence of impurities and/or defects in the epilayers.

In this thesis, a HR800 integrated system by Horiba Jobin Yvon in a back-scattering configuration was used for the acquisition of PL maps. The excitation wavelength was supplied by a continues He-Cd laser (325 nm), which was focalized on the sample by a x40 objective, whit numerical aperture (NA) of 0.5. the emitted light was reflected onto a 300 grooves/mm kinematic grating.

3.1.2 Raman (RM) measurements

Raman scattering spectroscopy is a vibrational spectroscopic technique that enables a wide range of information about a material to be acquired. When light is scattered from a solid material, the scattered light mainly contains the wavelengths that were incident on the material, which is called *Rayleigh scattering*.

However, the scattered light also contains different wavelengths at much lower intensities, caused by the interaction of the light with the material. A typical example is the interaction of the light with phonons, and this scattering is called *Raman scattering* [130]. The scattered light, which has an energy that is lower than that of the incident light by an amount equal to the energies of the emitted phonons (*Stokes-shifted Raman scattering*), is monitored in Raman scattering spectroscopy. An intense laser such as an argon ion laser is used as an excitation source, and a high-resolution double monochromator is used to exclude the Rayleigh scattered light.

Because Raman scattered light contains detailed information about the phonons, Raman scattering spectroscopy is a powerful tool for identification of the material polytype and characterization of the stress or the defects in SiC [131] [132]. Because of the wide bandgaps of the SiC polytypes, 4H-SiC is completely transparent to conventional excitation light (e.g., 488 nm from Ar^+ laser). In this case, the Raman scattering signals have poor depth resolution. A confocal configuration and deep ultraviolet Raman scattering (using a frequency-doubled Ar^+ laser (244 nm)) have been proposed as methods to improve the depth resolution [133] [134]. In contrast, the lateral resolution is good, because the incident light can be focused to a small spot diameter (~1 μm), and mapping measurements are possible.

The group theory analysis predicts a number of phonon modes at the Γ point for the higher polytypes (*folded modes*). For the hexagonal (and rhombohedral) SiC polytypes, the phonon modes are divided into axial and planar modes, in which the atoms are displaced along the directions parallel and perpendicular to the *c*-axis, respectively. For *n*H-SiC, a folded mode at the Γ point corresponds to a phonon mode with a reduced wave number $x = q/q\mathrm{B} = 2m/n$ along the <111> direction in the basic Brillouin zone of 3C-SiC, where m is an integer that is less than or equal to $n/2$, and qB is the wavenumber at the edge of the basic Brillouin zone. The planar modes in *n*H-SiC consist of Raman active E_1 and E_2 modes, and the axial modes consist of Raman active A_1 and inactive B_1 modes. It should be noted that the Raman scattering spectra that are observed depend on the scattering geometry.

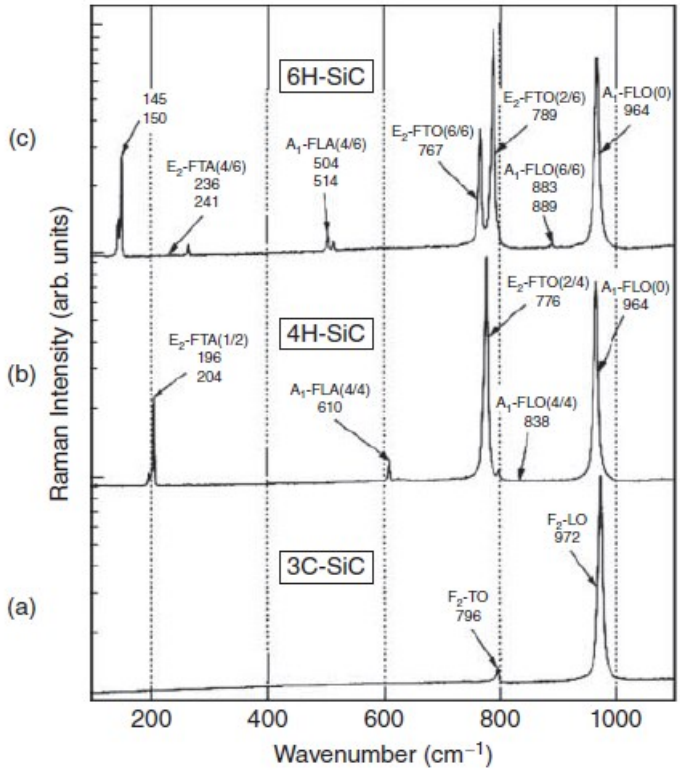

Figure 32. Raman scattering spectra of (a) 3C-, (b) 4H-, and (c) 6H-SiC polytypes observed with the back scattering geometries of {0001} crystals.

In the typical back scattering geometry for hexagonal SiC {0001}, E_2-type TO (folded transverse optical, FTO), and A_1-type LO (folded longitudinal optical, FLO) modes are allowed, while the E_1-type LO (FLO) mode is prohibited (the E_1-type LO peak is weakly observed when the sample has an off-angle).

Figure 32 shows the Raman scattering spectra of the 3C-, 4H-, and 6H-SiC polytypes, which are observed with the back scattering geometries of {0001} crystals. In the low-frequency region below 280 cm^{-1}, Raman peaks attributed to the TA (folded transverse acoustic, FTA) modes are observed, except in 3C-SiC. Intense Raman peaks caused by the TO and LO modes appear at wavenumbers of approximately 770–800 and 960–970 cm^{-1}, respectively, but the peak positions differ slightly for the different SiC polytypes. Table 7 summarizes the Raman wavenumbers of the TA, LA, TO, and LO modes observed for 3C-, 4H-, and 6H-SiC [135]. Raman scattering is thus a useful and non-destructive technique for unambiguous identification of the SiC polytypes. Raman modes for other SiC polytypes can be found in a review paper by Nakashima and Harima [135]. Because the Raman scattering spectra are sensitive to the stacking structures, the existence of stacking faults can cause the appearance of extra peaks and/or distortion of the Raman peaks.

In a polar semiconductor like SiC, free carriers interact with the LO phonons, forming the *longitudinal optical phonon-plasmon coupled (LOPC) mode*. Thus, the Raman peak due to the LO mode is affected by the carrier density in the monitored region. As the carrier density increases, the LO peak shifts toward the high wavenumber side with peak broadening. The carrier density can then be estimated by fitting this LO peak while taking the plasmon coupling into account [136].

Table 7. Major Raman wavenumbers of the TA, LA, TO, and LO modes observed for 3C-, 4H-, and 6H-SiC.

Polytype	TA (cm^{-1}) (planar acoustic)	LA (cm^{-1}) (axial acoustic)	TO (cm^{-1}) (planar optic)	LO (cm^{-1}) (axial optic)
3C-SiC	–	–	796	972
4H-SiC	196, 204	610	776, 796	964
6H-SiC	145, 150	504, 514	767, 789, 797	965

Because Raman scattering is sensitive to strain, local stresses can also be characterized. The stress can be quantitatively determined based on the shift of a Raman peak from its original position. Stress characterization by Raman scattering is receiving increasing attention in the Si and III–V semiconductor fields [137]. Similarly, Raman scattering is likely to be used extensively for stress characterization of SiC.

Therefore, Micro-Raman spectroscopy is a powerful technique based on the inelastic scattering of light (usually supplied by a laser) by solid-state material. A typical Raman spectrum allows a rapid analysis of the phonon modes which incorporate many properties of the semiconductor material. The high spatial and spectroscopic resolution of the micro-Raman technique makes it suitable for the analysis of defects in thin film. Currently, the Micro-Raman technique can be used as a complementary method to PL imaging for SiC characterization thanks to the simultaneous collection of information related to the material probed, e.g., strain status, polytype inclusion, doping concentration.

Some authors have reported the relationship between SFs and Raman scattering [138][[139] in the cubic polytype (3C-SiC). An enlargement and a shift of the TO Raman mode is observed for highly defective epilayers (which shows an appreciable enlargement of the TO Raman mode for high stacking fault density, with an average distance between the SFs of 20 nm) and in regions with intense stress fields [140] [141]. Given the higher quality of 4H-SiC homoepitaxial films (characterized by much lower defect densities and stress fields) the enlargement and shift of the TO Raman mode cannot be used. Micro-Raman technique has been used to study the properties of SiC and to detect extended defects [142] in highly

defective regions by using the variation of the TO Raman mode that depends on the stacking fault density. Moreover, the UV-Raman technique has been used to detect comet defects in 4H-SiC [143] by probing the intensities of the Raman modes, and to characterize ion implanted SiC crystals, [144] demonstrating that, by using a deep UV laser as excitation wavelength, micro-Raman spectroscopy is a powerful tool for investigating surface structures and surface defects.

An alternative method that allows the detection of defects (in particular, SFs) can be considered by using the longitudinal optical (LO) Raman mode, as mentioned before. The atomic displacements associated with the LO phonon mode generate a longitudinal electric field (due to the partially ionic nature of the lattice and the difference in electronegativity between Silicon and Carbon atoms) which interacts with the neighbouring electrons.

In the case of high free-carrier density such a longitudinal electric field results in an additional interaction between the LO phonons mode and the free carriers [145]. The mathematical model that describes such an interaction is widely used and described in the literature, [146][[147] [148] it determines the doping [149] [150] and the electron mobility [149] of thin films. Micro-Raman analysis has also been used along with the Hall effect and transmission measurements to extract carrier density profiles from SiC wafers [151]. Moreover, as described by some authors, [152] at high optical excitation the formation of a dense electron-hole plasma has been observed in many semiconductors (GaAs, GaP). Furthermore, under an intense laser excitation, the LO phonon-plasmon coupling mode has been detected and studied in undoped GaP crystal [153]. In this context the excess carriers, induced by laser pumping, are characterized by a carrier lifetime and electrical mobility, appearing as a local increase of carrier concentration that can be easily measured by Raman tools. These electrical properties are perturbed by crystallographic defects so that a systematical study of the local (induced) carrier density variation can be used to detect crystallographic defects. Free carrier redistribution, resulting from SF formation in annealed 4H-SiC, has been observed by some authors [154]. Based on these considerations a new Raman methodology analysis, called induced-LOPC (i-LOPC), was designed. The injection of free carriers by a laser with a wavelength lower than the material band edge (HeCd at 325nm, 4H-SiC band-gap at 388 nm) with different power densities was used to study the effect of a crystallographic defect, such as SF or point defects, on a local increase of the carrier density.

The interaction between the electronic plasma and the lattice vibration, through inelastic scattering, is related to the plasmon damping constant $\gamma = e/(m^*\mu)$, and the plasmon

frequency $\omega^2_p = 4\pi ne^2/\varepsilon_{inf}m^*$, where e is electron charge, m* is the electron effective mass, μ is the carrier mobility, and ε_{inf} is the high frequency dielectric constant, see Ref. [148] for details.

From this set of equations, it is possible to extract n and μ, hence determine the doping and carrier mobility of the film.

It is interesting to note that, in general, the effective electron-hole pair density (n) is controlled by the equilibrium conditions between carrier generation (G) and recombination processes (U), this equilibrium can be expressed by the following expression:

$$U = G = n - n_0/\tau; \quad (1)$$

where n is the equilibrium carrier concentration, n_0 is the initial carrier concentration, τ is the minority carrier lifetime and G is the injection of carriers due to the laser exposure

$$G = \Phi\alpha e^{\alpha x}; \quad (2)$$

where Φ is the flux applied by the laser, α is the absorption coefficient, and x is the distance within the epitaxy at which the carriers are generated. In the case of high doped epitaxies, low laser densities or low carrier lifetimes $G\tau << n_0$ so that $n\text{-}n_0 \sim 0$, and no carrier generation can be revealed ($n \sim n_0$ 10^{18}). In these conditions, the standard Raman LOPC determines the film doping (n_0). On the other hand, in the case of low-doped epitaxies ($n_0 < 10^{15}$) and for high carrier injections ($\Phi > 10^{17}$) a substantial carrier generation can be observed and from Eqs. (1) and (2) carrier lifetime can be extracted.

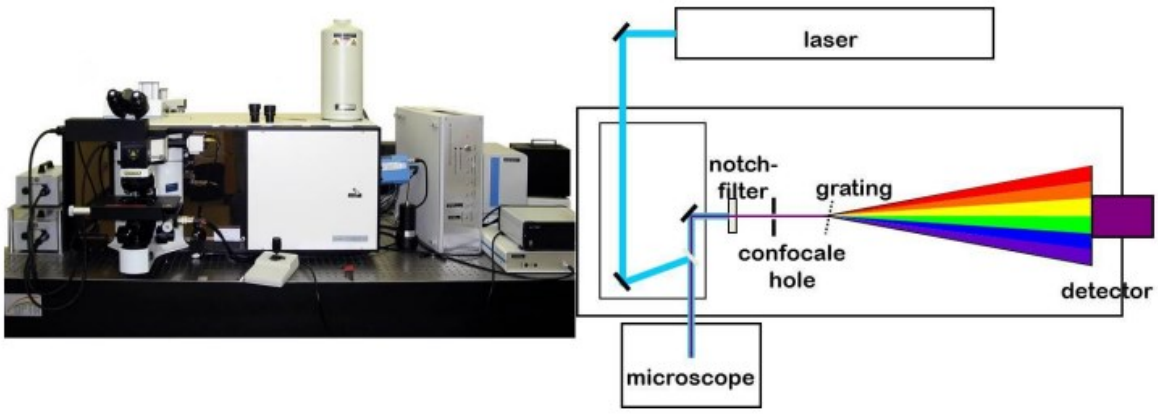

Figure 33. Schematic apparatus used for PL and Raman analysis.

We systematically compared the PL signal and the phonon modes to determine the nature of the perturbation generated by the defects observed in Raman spectra: crystallographic and stress field effects (TO mode sensitive) or electronic effects (LO mode sensitive).
Micro Raman maps were acquired using an HR800 integrated system Horiba Jobin Yvon [155] in the back scattering configuration (see Figure 33). The accuracy of the instrument at room temperature (±1 °C) is about ±0.2 cm^{-1}. The spatial resolution achievable with the motorized stage is 0.5 µm and is also used for spot laser definition. A He-Cd Laser with a wavelength of 325 nm was used for these measurements. The laser power was changed from 0.15 to 15 mW using different filters. A x40 objective was used to focus the laser. The diameter of the laser spot was about 9 µm. This value was extracted following the Raman signal across a metal line previously realized using photolithography. Each Raman spectrum was collected with an acquisition time of about 1 s. For the lowest laser power (0.15 mW), the acquisition time was increased (12 s) in order to obtain an appreciable signal.

3.1.3 Time resolved photoluminescence (TRPL) measurements

The PL intensity of the free exciton peaks is proportional to the number of excess free carriers, although the majority of the free carriers and excitons recombine via nonradiative recombination in SiC because of its indirect band structure. The carrier lifetime can therefore be determined from the decay curve of the PL intensity for the free exciton peaks (~390 nm at room temperature). No preparatory processing, such as contact formation, is required prior to the measurements, and it is easy to acquire maps of the carrier lifetimes of SiC wafers with high spatial resolution using a conventional PL mapping stage. The temperature dependence of the carrier lifetimes can also be measured easily. Assuming the density of the excess carriers as Δn, the intensity of the free exciton peaks is proportional to $(n + \Delta n)(p + \Delta n) \sim (\Delta n)^2$ when Δn is higher than the equilibrium carrier density (high-injection conditions), while it is proportional to Δn when Δn is lower than the equilibrium density (low-injection conditions). Therefore, the decay time obtained (τ_{decay}) gives $\tau/2$ under high-injection conditions and τ under low-injection conditions (where τ is the carrier lifetime) [156].
Time-resolved photoluminescence measurement was conducted using a 5 µs pulsed lamp. The wavelengths of the polychromatic emission pulse were selected with a low straylight double monochromator before reaching the sample. The luminescence decay was recorded with a photomultiplier and using a decay-by-decay technique, with a time window of 0.1 ms.

3.1.4 Deep level transient spectroscopy (DLTS) measurements

Deep Level Transient Spectroscopy (DLTS) is an efficient and powerful method used for observing and characterizing deep level impurities in semiconductors. The method was initially introduced by D. V. Lang [157] in 1974. DLTS is a capacitance transient thermal scanning technique, operating in the high frequency (Megahertz) range. It uses the capacitance of a p-n junction or Schottky barrier as a probe to monitor the changes in charge state of a deep centre. The capacitance techniques [158] [159] used before DLTS lacked either in sensitivity, speed, range of observable trap depths, or the spectroscopic nature, thus rendering the techniques inadequate for a complete characterization of a deep level. DLTS has the advantage over all the techniques used to-date in that it fulfils almost all the requirements for a quick and complete characterization of a deep centre. DLTS is a technique, which is sensitive enough, rapid and easy to analyze. It can distinguish between majority- and minority-carrier traps [160]. DLTS can also give the concentrations, energy and capture rates of both kinds of traps. It is spectroscopic in the sense that it can also resolve signals due to different traps. In the many variants of the basic DLTS technique the deep levels are filled with free carriers by electrical or optical methods. Subsequent thermal emission processes give rise to a capacitance transient. The transient is analyzed by signal processing while the temperature is varied at a constant rate. This results in a full spectroscopic analysis of the semiconductor band-gap.

Figure 34. Typical instrument for deep level transient spectroscopy measurements.

Deep level transient spectroscopy (DLTS) measurements were carried out by means of a Sula Technologies, Ashland in Oregon (USA), double boxcar spectrometer with exponential

correlator measurements in the temperature range 100–750 K by using rate windows in the range 2–200 s^{-1} (Figure 34).

3.2 Sample characterization

The epitaxial films were grown in a hot-wall reactor (P106 built by LPE Epitaxial Technology) that allows for the growth on 6 inches (150 mm) wafer. The chamber was designed to reduce the temperature ramp-up and ramp-down time and particle formation. The substrates were 4H- SiC (0 0 0 1), Si face, n-type (N_D $10^{18}/cm^3$) off-axis (4° off towards the [11-20] direction). The wafers were loaded into the reactor through a load lock that was pumped down to a pressure of 10^{-5} Torr. The growth begins with a hydrogen etch sequence. At the deposition temperature (1550–1650 °C) the growth precursors are introduced into the hydrogen carrier gas flow (150slm) and the growth starts at a fixed pressure of 100 mbar. TCS was used as the silicon source, ethylene as the carbon source and nitrogen or trimethylaluminum (TMA), respectively, for n-type and p-type doping. The epitaxial layers were grown with different Si/H2 ratios that produce different growth rate. At the starting of the growth, a high doped buffer layer was grown with a thickness of about 5 microns. This buffer layer should remove several defects present in the substrate (dislocations and SFs) and avoid that the depletion layer in reverse bias reach the substrate and then produce a high leakage of the junctions due to the high density of defects of the substrate. The obtained layers were analyzed by Fourier transform infrared reflectance (FTIR) for film thickness determination, and mercury-probe C–V measurements for the doping concentration.

The optical characterization on the 250 µm thick epi-layer was performed by room temperature photoluminescence spectroscopy. As shown in Figure 30, most of the defects are located on the left edge of the wafer (35a), highlighted by blue and green colours. This effect is connected to the presence of the off-axis of the substrate towards the [11–20] directions. With this off-axis the left side of the wafer does not present a lateral growth of the steps and more defects are generated in this region. This behaviour is more evident in the thick epitaxial layers and less evident in the thin ones. The red portion of Figure 35 represents the SF-free zone as it shows only the typical 4H-SiC band-to-band peak (3.23 eV).

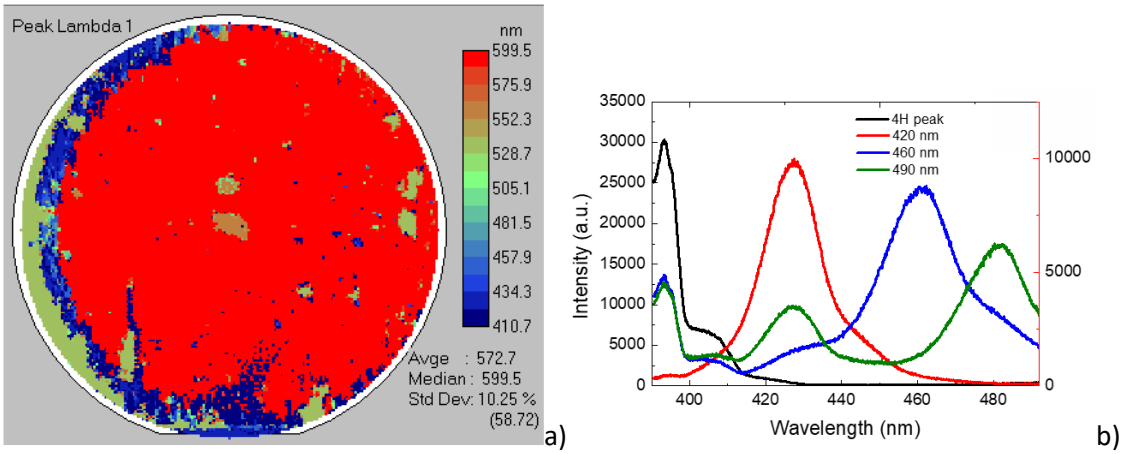

Figure 35. Photoluminescence map (a) and relative stacking fault peaks (b) of 4H-SiC with epitaxial layer thickness of 250 µm. The black peak represents the band-to-band energy while other peaks are different kinds of SFs, located on the left edge of the wafer. The y-scale on the left is relative to the 4H-SiC region without SFs, while the y-scale on the right is relative to the different SFs.

Apart from the band-to-band peak at about 390 nm, the other three peaks related to defects can be observed, alongside different kinds of in-growth stacking faults, at 430 nm, 460 nm, 490 nm. The staking sequence was determined as the (4,4) and (5,3) types in the Zhdanov's notation for 460 nm and 490 nm peaks respectively [161]. The peak at about 430 nm could be related to a bar-shaped staking fault or a single Shockley stacking fault because both exhibit a similar emission wavelength [162]. Some of these stacking faults (SF) are generated from the substrate due to the basal plane dislocations (BPD) but they can also be produced in the epi-layer during the growth, for example due to the presence of impurity deposited on the sample. This kind of defect can affect the reliability and the performance of semiconductor devices owing to the increase of leakage current and the reduction of the carrier lifetime. Therefore, the red zone of the wafer in Figure 35 is the area with the lowest number of defects and represents the useful part for the realization of the devices.

One of the main parameters of the material that strongly affects the performance of the detector is the carrier lifetime. Hence, to collect all the charges generated by neutrons, it is necessary that these charges can reach the contacts and then a high diffusion length is needed in these very thick detectors. To obtain a good measurement of this parameter, several techniques can be used, starting with the micro–Photo Current Decay (µPCD), or the time resolved photo luminescence (TRPL) [156]. An alternative method to define the carrier lifetime is Raman spectroscopy, in particular the Longitudinal Optical Phonon-Plasmon Coupling mode (LOPC) [163], as described in the previous section. The LO phonon mode, due to the atomic displacement associated with it, allows the interaction between nearby

electrons generating a longitudinal electric field which, due to high intensity of free carriers, leads to an additional interaction between the free carriers and the LO phonon mode [145]. As a consequence, there can be observed an LO shift, while the transverse optical (TO) peak always maintains the same position, as shown in Figure 36. The following measurements were taken away from defects, in relatively clean areas. These results will be compared with the values obtained in the vicinity and on the various types of isolated SFs.

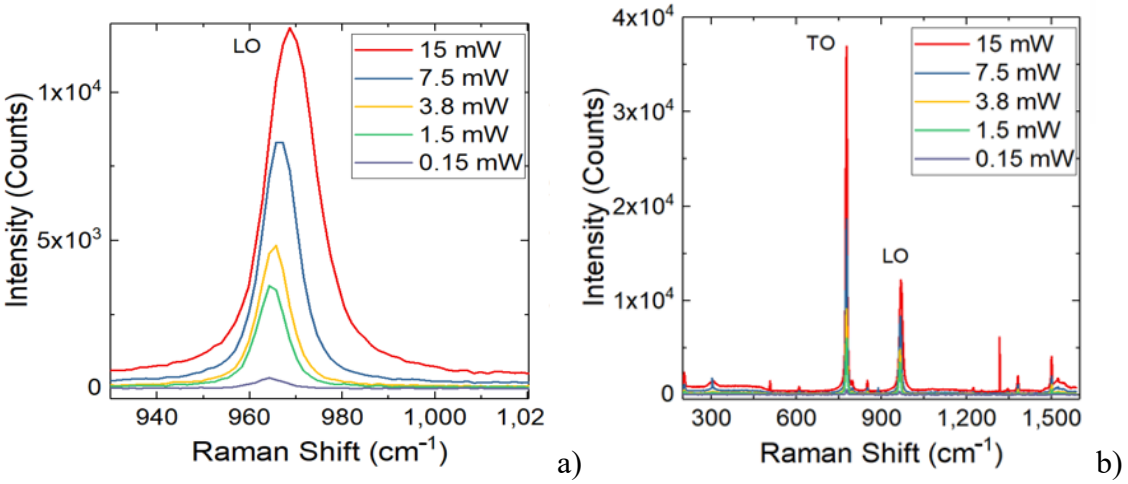

Figure 36. Raman spectra for 250 um sample analyzed at different laser powers (a) and a focus on LO peak (b). The LO shift can be observed while TO peak is always in the same position.

This interaction is widely described in the literature [146] [147] [148] through a mathematical model that allows us to determine the doping [151] [149] and the electron mobility [164] of thin films.

This Raman methodology analysis, called induced-LOPC (i-LOPC), was used in the present work to study the epitaxy quality.

The Raman shift at different laser powers was observed. The LOPC mode was acquired for a low-doped epitaxial layer with 250 µm thickness (N_D about 10^{14} at/cm^3) 4H-SiC film at different laser powers (from 0.15 to 15 mW).

As can be seen in Figure 37, by increasing the laser power, an increase in the Raman shift (LO peak) is obtained and consequently there is also an increase in the laser-induced carrier density. The LO peak underwent a significant shift towards high frequencies due to the increase in e-h pairs generated as the laser power increases. Through the analysis of the LOPC, the free carrier concentration was obtained [136] [148] [165], and Table 8 shows the results.

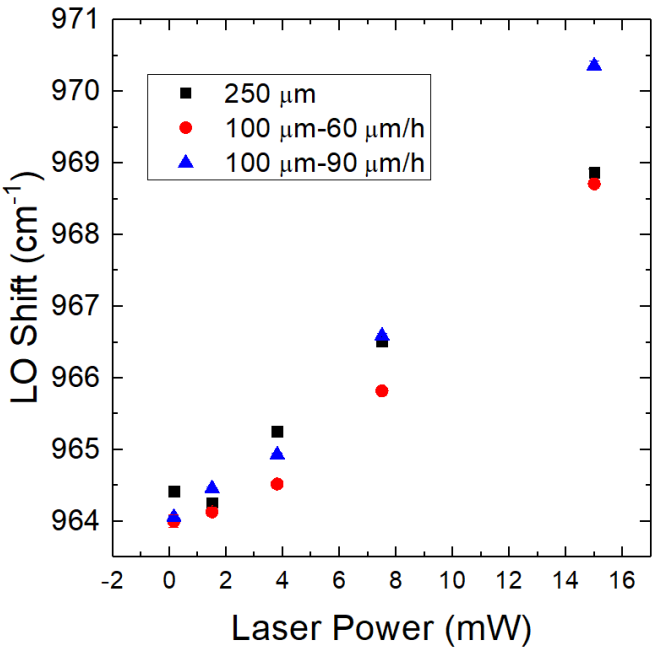

Figure 37. Plot of the Raman shift as a function of laser power used for 4H-SiC epilayers with different thickness.

Table 8. LO Raman Shift, carrier density, carrier lifetime and diffusion length as a function of laser power.

Laser Power (mW)	Peak Center (cm^{-1})	Carrier Density, *n* (At/cm^3)	Carrier Lifetime (µs)	Diffusion Length (µm)
0.15	964.4	3.17×10^{17}	8.71	47.88
1.5	964.3	3.57×10^{17}	0.98	16.02
3.8	965.2	4.15×10^{17}	0.45	10.54
7.5	966.5	5.83×10^{17}	0.32	8.43
15	968.8	9.32×10^{17}	0.26	6.75

As shown in the Table 8, diffusion length values were calculated, however these values are much lower than the epitaxial thickness, necessary for a good detection yield of the detector. It should be emphasized that in this case we are in a high injection regime while the detectors will work in a low injection regime. However, these values are representative of the carrier lifetime behaviour even if TRPL measurements are more confident because they are in a low injection regime, but in any case, it's possible to observe an increment in carrier lifetime with some post growth processes.

There are some processes to increment the carrier lifetime and the diffusion length for 4H-SiC. A post thermal growth process, such as oxidation and passivation, could increase these values thanks to the decrement of carbon vacancies [125], as described later.

A subsequent analysis was conducted to compare the above data for 250 µm thick layer with other 4H-SiC samples having different thickness or different growth rate. A determination

of carrier lifetime and residual carrier density was done for other two samples with an epitaxial layer of 100 µm. Table 9 shows carrier lifetime results for all samples. These 100 µm samples were previously grown epitaxially with the same CVD process in the same horizontal hot-wall reactor with a similar process.

Table 9. Carrier lifetime τ (µs) data for each sample as a function of laser power.

LaserPower (mW)	τ (µs) 100 µm 60µm/h	τ (µs) 100 µm 90µm/h	τ (µs) 250µm 60µm/h
0.15	14.38	6.43	8.71
1.5	0.85	0.80	0.98
3.8	0.40	0.38	0.45
7.5	0.28	0.33	0.32
15	0.26	0.30	0.26

As a result, the carrier lifetime decreases with the increment of laser power. The two samples with the same thickness (100 µm) and different growth rates show a better carrier lifetime in the case of the lower growth rate (60 µm/h). This behaviour is related to a higher concentration of point defects at a higher growth rate that has been previously predicted by Monte Carlo simulations [166] [167] and then confirmed by experimental results [168]. The decay of the quality of the epitaxial growth with increasing thickness has been observed in a previous work [124] where a decrease in the yield of the Schottky diodes was observed for the same epitaxial process, increasing the thickness from 30 to 80 µm, due to the increase of the leakage current of the diodes. In this work we have observed instead a deterioration of the carrier lifetime due to the increase of point defects, probably related to the roughness increase at the surface of the epi-layer due to the step bunching observed in 4H-SiC.

Moreover, for an injection level under 10^{18} cm^{-3}, the radiative contribution can be neglected, so that the Auger recombination (AR) can be neglected too [156]. When the concentration of induced carriers increases, the Auger recombination mechanism becomes more and more important, passing first through a monomolecular recombination mechanism and then through a bimolecular one, as the carrier concentration increases [90]. Probably, due to the high laser powers used, a greater concentration of carriers is induced, and a shorter lifetime due to recombination mechanisms is obtained.

As described in the literature [169], for the highest concentrations, in a high injection regime, the bimolecular recombination rate is presumably contributed by both band-to-band radiative and trap-assisted Auger recombination mechanisms, where the carrier lifetime is lower. It is important to note that surface recombination and point defect recombination

contributions are not distinguished by this method and the temperature could affect diffusivity and recombination rates [170].

In the Figure 38, the trends of the carrier lifetime as a function of laser power for all the analysed samples are shown.

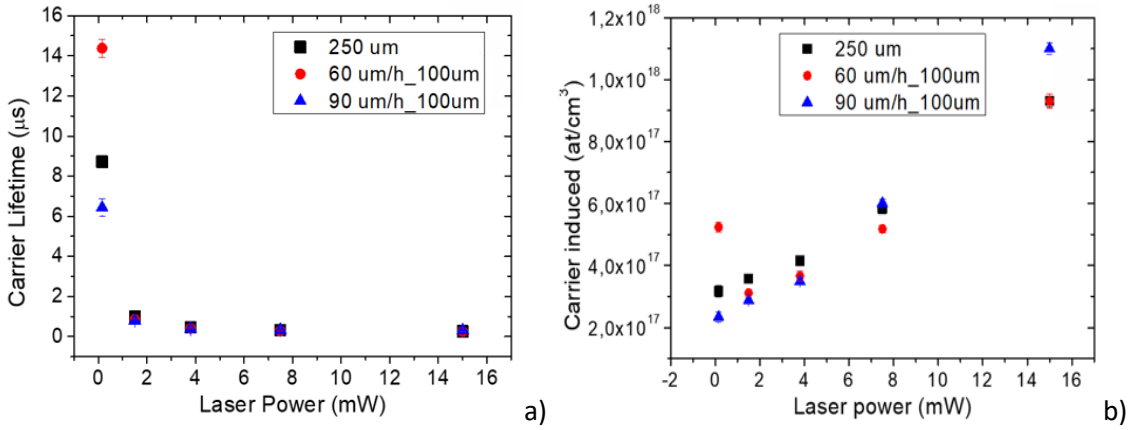

Figure 38. The figure shows the trends of the carrier lifetimes (a) and the amount of carrier induced (b) as a function of Raman shift and laser power for all samples analysed.

As the values listed in Table 9, the carrier lifetime increments when the laser power decreases are reported.

As stated above, the carrier lifetime analysis was done in SF-free areas. To estimate how different types of SFs can affect the increase of free carriers and the carrier lifetime trend, several PL and Raman maps were acquired on SFs in order to compare them with data acquired far from defects. As shown before (Figure 35b), we have different kinds of SF defects that can influence in different ways the characteristics of 4H-SiC devices. Thanks to photoluminescence spectroscopy, it is possible to detect and analyse different crystalline defects inside the epi-layer, which act as recombination centres and, in some cases, we could define whether the SF defects start from the interface, in the basal planes. In general, considering the width of the bars, for the bar shaped SFs, we could calculate the depth of the defect, knowing the off angle and epitaxial thickness [162].

Figure 39 shows a PL map for a SF with energy of 2.88 eV (430 nm) and a variation of TO intensity on and out of SF using high laser power.

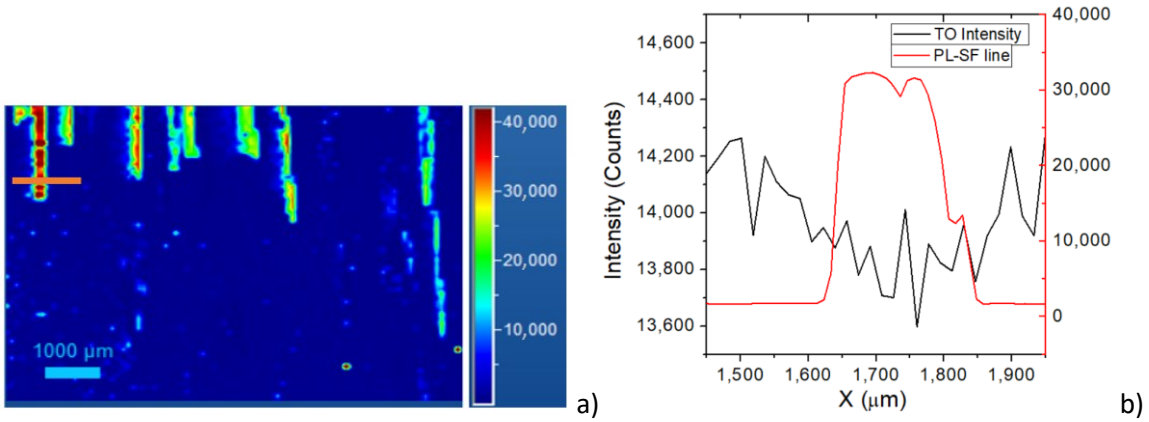

*Figure 39. PL map of an isolated defective zone (SF at 430 nm) **(a)**, and the result of the Raman map line compared with the TO intensity variation (**b**), using a laser power of 15 mW.*

A Raman line across the isolated defect was done, as defined in Figure 38a, using different laser powers to determine the carrier density and the carrier lifetime on the SF and in its proximity. It was performed as the same analysis on different SFs defects, with different energies, 2.43 (510 nm) and 2.53 eV (490 nm), respectively. It was observed that using high laser power (15 mW), the spectrum acquired on the SF showed a strong Raman shift reduction, suggesting a trapping of free carriers. As shown in Figure 40, for the lower laser powers used, we observed that under 3.8 mW, there are no differences between the ON SF and OUT SF spectra.

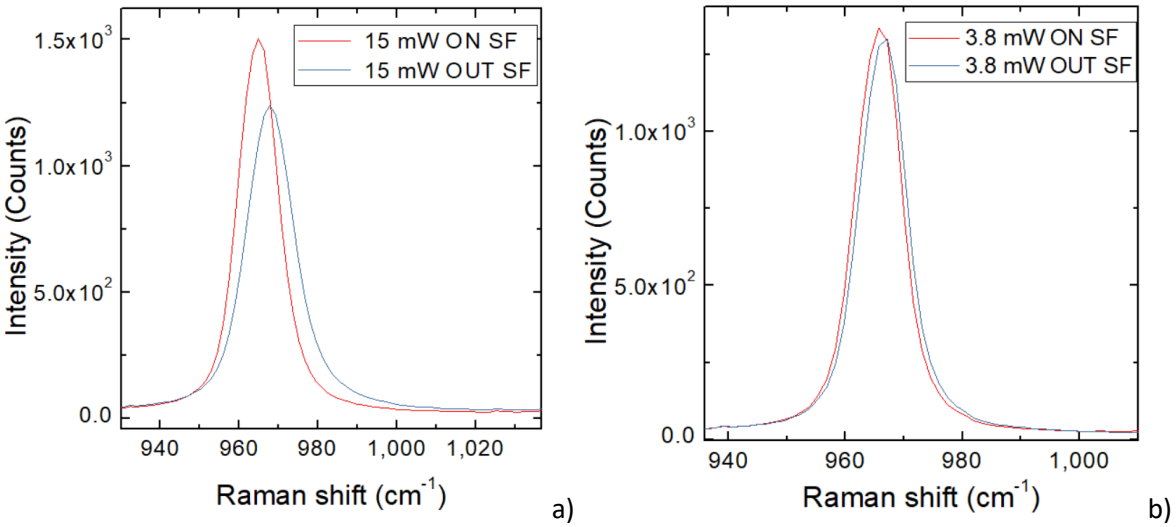

*Figure 40. The figure shows LO Raman Shift on, and in proximity of, isolated SF defect at 430 nm (2.88 eV) with a laser power of 15 mW (**a**) and 3.8 mW (**b**) observing a reduction on shift.*

This suggests that the same values of carrier induced, and the lifetime in and out, of the defect (in proximity) are obtained when low laser power is used. This difference is more evident by the Raman maps, following the LO peak shift as shown in Figure 41.

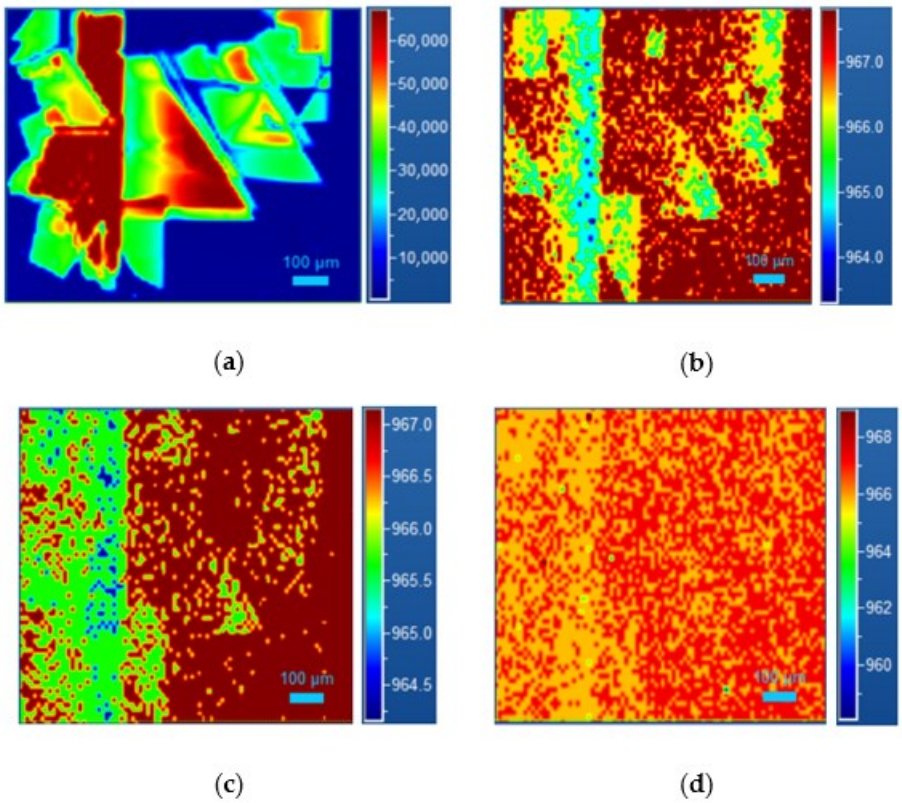

*Figure 41. PL map (a) and Raman map following LO peak shift for a SF at 2.88 eV (430 nm), at different laser powers: 15 (**b**), 7.5 (**c**) and 3.8 mW (**d**) respectively.*

As the laser power decreases, a reduction of the LO Raman shift is observed. This effect is probably due to the fact that, if the carrier lifetime and the diffusion length increases, and then this measure is mediated in a larger region around the SFs, the effect of the carrier lifetime and the induced carrier is lower.

Table 10 shows the lifetime values for different kinds of SFs and for different laser powers compared with the defect-free areas far from the stacking faults.

Table 10. Carrier lifetime data on different SFs defects compared with values on clean area.

LaserPower (mW)	τ (µs) 430 nm Peak	τ (µs) 490 nm Peak	τ (µs) 510 nm Peak	τ (µs) Clean Area
0.15	5.41	3.46	4.43	8.71
1.5	0.68	0.49	0.48	0.98
3.8	0.31	0.23	0.24	0.45
7.5	0.23	0.17	0.17	0.32
15	0.18	0.14	0.15	0.26

As shown in the table above, carrier lifetime data for all SFs are lower than in the clean area. The most common long-range defect in our sample is the SFs at 430 nm in the PL map, the other two, 490 and 510 nm, are generally located on the edge of the wafer, as shown in Figure 35a.

From these results it is clear that Raman spectroscopy is a powerful tool for careful characterization of 4H-SiC epitaxial layers. By exploiting the i-LOPC method it is therefore possible to define parameters such as doping, mobility and lifetime of carriers in the epitaxial layers. Moreover, the different types of defects act in a slightly different way on the carrier lifetime, leading to a recombination or trapping of the free carriers.

An in-depth study of the epilayer is critical to understand the performance of a future device. Some growth parameters influence the quality of the final layer. Among all, the conditions of growth rate and the Si/C ratio play an important role in the defect formation and annihilation. Stacking fault (SF) defects are commonly present in the epitaxial layers. In general, as reported by La Via [123] and Kimoto [68], they are obtained from basal plane dislocation (BPD) propagation from the substrate into the epilayer, but they also can appear directly in the epilayer during growth. Previous studies evidenced the influence of this SF defect on the increment in the recombination current, and this recombination is dependent on the levels introduced in the band gap by the different kinds of SF defects [171].

Carrier lifetimes in n-type 4H SiC have been intensively investigated in recent years [85] [156]. Despite the relatively long carrier lifetime obtained in previous studies [172] [173], it is possible to improve this parameter by identifying and reducing the causes that lead to the reduction in the lifetime, therefore the killer defects.

Many types of defects can adversely affect the carrier lifetime, in particular the $Z_{1/2,}$ which is considered the dominant lifetime killer, and it is a common intrinsic defect in this material. In previous studies, the influence of growth parameters during the CVD process was evaluated [174] [175] [176].

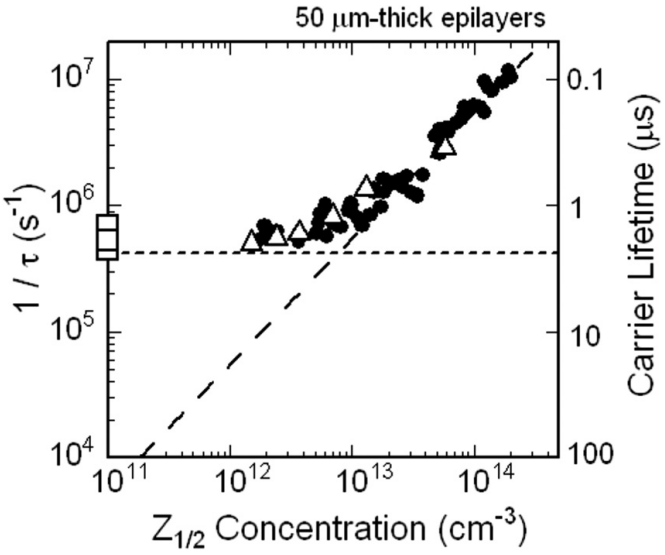

Figure 42. Carrier Lifetime as a function of $Z_{1/2}$ centers concentration.

Moreover, a direct correlation between $Z_{1/2}$ centers and carrier lifetime was defined through low-energy electron irradiation that allows a displacement of carbon atoms, highlighting that this type of defect could be a carbon vacancy or carbon interstitial [56]. There are some processes that allow reduction or elimination as either carbon ion implantation [86] [177] or thermal oxidation [87] [178].

The $Z_{1/2}$ center, which is located at 0.65 eV below the conduction band edge, is now recognized as the dominant lifetime killer, at least, in n-type 4H SiC. As described in the literature, thermal oxidation or carbon ion implantation followed by high-temperature annealing was used to eliminate or reduce the $Z_{1/2}$ center concentration. On the contrary, new depth levels, ON1 (E_C −0.84 eV) and ON2 (E_C −1.1 eV), are detected after thermal oxidation or C^+ implantation, followed by Ar annealing [177], which could be related to interstitials diffusing from the SiO_2/SiC interface (oxidation), or from the implanted region (C^+ implant). Although the effects of the centers ON1 and ON2 on the lifetime are negligible with respect to the effects of the $Z_{1/2}$ centers [179], they may have an effect, not yet well identified, on the carrier lifetime but still less than that of the $Z_{1/2}$ centers. The decrease in carrier lifetime is attributed not only to $Z_{1/2,}$ but also surface and interface recombination and extended defects as staking faults [180] [181].

In a previous paper, the effect of different stacking fault defects was evaluated [127], and a decrement of carrier lifetime, on and around the SFs, was observed. In the present thesis, the carrier lifetime in n-type 4H SiC was further improved by employing a high-temperature and long oxidation process, 1400 °C for 48 h, for a very thick epilayer.

The oxidation process was conducted after the deep cleaning of the sample with acetone, isopropanol and methanol, each in an ultrasonic bath for five minutes. After an RCA process (20 min), cleaning with piranha solution and HF was performed. Furnace ramp up and ramp down was performed at 8 °C/min in Ar atmosphere, and then pure dry O_2 oxidation (0.5 l/min) at 1400 °C for 48 h was conducted.

In order to obtain this information, PL and LOPC Raman spectroscopies were used. Time-resolved photoluminescence was used to evaluate the carrier lifetime across the entire epilayer, using different wavelengths of the source. The decrease in $Z_{1/2}$ centers, which led to an increase in the carrier lifetime after thermal oxidation process, was evaluated using DLTS measurement. Then, a study of the influence of different kinds of SF defects on the carrier lifetime was evaluated after the oxidation process and compared with a non-oxidated sample.

The most common defects that can strongly affect the carrier lifetime are not only the carbon vacancies, defined as $Z_{1/2}$ centers, but also extended defects, such as stacking faults. In 4H SiC epilayers, the carrier lifetimes can be limited by other recombination paths, such as recombination near the epilayer/substrate interface and surface recombination [182]. The thermal oxidation process, as mentioned before, leads to an increment in carrier lifetime thanks to the $Z_{1/2}$ centers' decrement confirmed using DLTS measurements.

Figure 43 shows the DLTS spectra acquired at a rate window of 4.65 sec^{-1} of the non-oxidized sample (black line) and after thermal oxidation (red line). The dominant levels in the no-ox sample are $Z_{1/2}$ (Ec − 0.62 eV) and $EH_{6/7}$ (Ec − 1.5 eV); the energy levels were determined, as usual, using an Arrhenius plot of measurements performed at different rate windows. The concentration of these levels was 0.8×10^{12} cm^{-3} and 0.6×10^{12} cm^{-3}. This value is consistent with the previously reported value in the literature [113] for this thick epilayer, and also, the small capture cross section of 10^{-15}–10^{-16} cm^2 indicated that these defects were mostly single atoms, rather than clusters. Despite this, $Z_{1/2}$ centers could influence lifetime, but these two levels disappeared after oxidation, while two new traps, ON1 (Ec − 0.78 eV) and ON2 (Ec − 1.1 eV), were generated near the surface region, but could be extended further across the entire epilayer using a higher temperature for a long time [183]. The concentration of ON1 and ON2 levels was 3.8×10^{12} cm^{-3} and 1.5×10^{12} cm^{-3}, respectively. In this case, an oxidation process at 1400 °C for 48 h was performed, and even though annealing with Ar as the post-oxidation process was not conducted, the $Z_{1/2}$ centers were eliminated. However, ON1 and ON2 centers appeared, and the exact structure and formation reaction of these centers was not known, but the concentration decrease with

the depth and their influence on carrier lifetime was negligible compared to $Z_{1/2}$ centers [184].

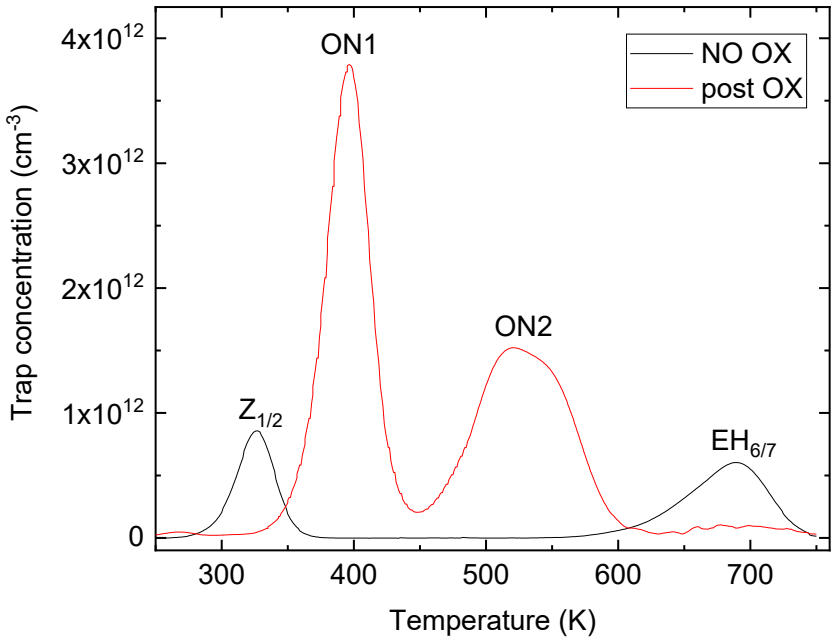

Figure 43. Deep level transient spectroscopy (DLTS) measurements on non-oxidated (black line) and post-oxidated (red line) samples with the appearance of new ON1 and ON2 centers

As mentioned before, the oxidation process allows a consistent decrement in $Z_{1/2}$ centers, thanks to the reduction in carbon vacancies, leading to carrier lifetime increment into the epilayer. This increment was appreciable using Raman spectroscopy, focusing the attention on the longitudinal optical peak shift, and is shown in Figure 44. The longitudinal optical phonon–plasmon coupling mode (LOPC) was used to extract carrier density and carrier lifetime.

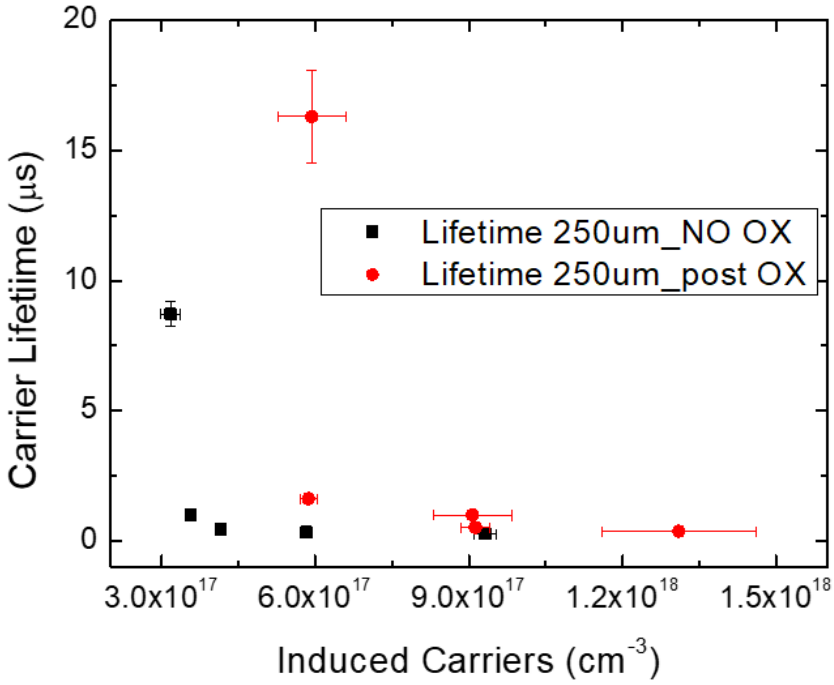

Figure 44. Carrier lifetime as a function of induced carriers, before (NO Ox) and after (Post OX) the oxidation process.

In Figure 45, the carrier lifetime as a function of the induced carriers using different laser powers during the Raman analysis is shown, observing an increment in carrier lifetime as the induced carriers decrease. The red points are the data obtained after the oxidation process, and it seems that there was an increment in the carrier lifetime, more visible at lower induced carrier values. This was due to the fact that if we have an injection level under a value of 10^{18} cm^{-3}, the Auger recombination (AR) can be neglected. However, as reported in the literature [90], monomolecular, bimolecular and Auger recombination coefficients can influence carrier lifetime.

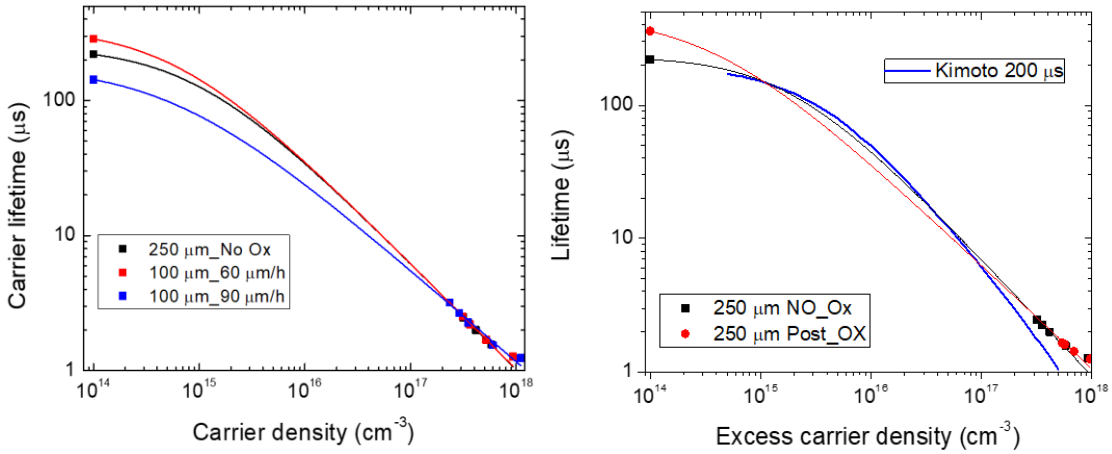

Figure 45. a) The figure shows the trends of the carrier lifetimes as a function of carrier density for all analyzed samples with different thickness; b) Comparison between the 250 um thick epi-layer before and after oxidation process.

Auger recombination (AR) became important when the doping or the excess carrier density became higher. Moreover, there is a temperature dependence of the Auger recombination coefficient (γ_3^{eeh}), specifically, the higher the temperature is, the lower the Auger recombination coefficient is. Finally, this AR coefficient can directly be derived from the relationship $\gamma_3^{eeh}=[\tau N^2_D]^{-1}$, where τ is the carrier lifetime and N_D is the carrier concentration; the oxidated sample shows a lower AR coefficient than a non-oxidated sample, hence a minor contribution of Auger recombination at high carrier density values favors a higher carrier lifetime.

These measures were conducted in SF-free areas and allow us to understand the direct increment in the carrier lifetime after the oxidation process in the high injection regime. This hypothesis is also supported by time-resolved photoluminescence (TRPL) measurements to evaluate the carrier lifetime in a low injection regime using different wavelengths to study different penetration depths. The comparison between oxidated (Post OX) and non-oxidated (NO Ox) samples is shown in Figure 46.

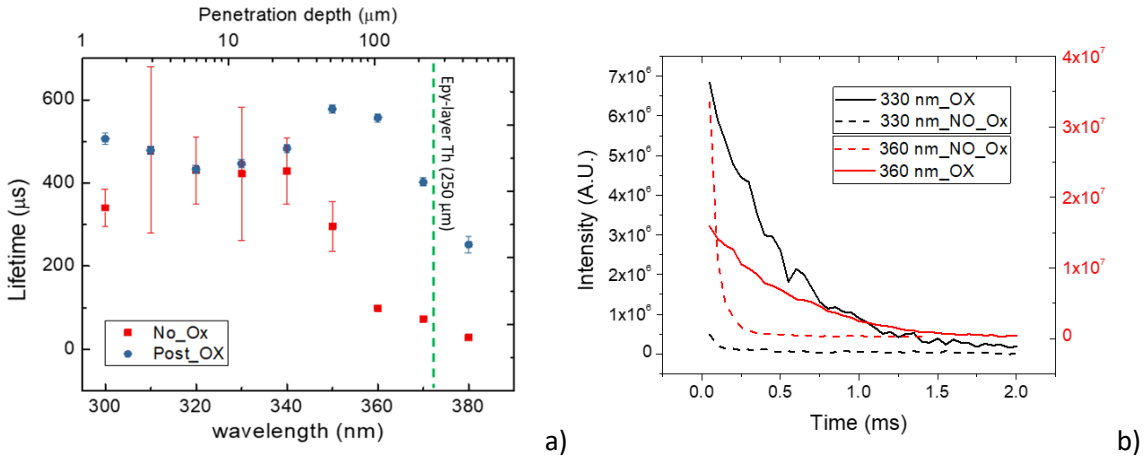

*Figure 46. Time-resolved photoluminescence measurements at different source wavelengths in order to obtain information from different depths, before and after oxidation process (**a**), and the decay curve obtained by this measure at 330 and 360 nm for both samples (**b**).*

The wavelengths used for the measurements were ranging from 300 to 380 nm with penetration lengths between 4 and 600 µm. The last point at 380 nm is referred to as a deep penetration depth, because the greater the wavelength, the deeper the beam penetrates, hence we were going through the entire epitaxial layer until we reached the top of the substrate. For this reason, the carrier lifetime value was lower than the measurements at lower wavelengths. Due to the large spot of the lamp, the signal obtained was averaged over the analyzed area, but the trend was clear and showed an increment in carrier lifetime for the

oxidated sample compared with the non-oxidated sample, especially close to the substrate interface. The different decays at the same wavelength are shown in Figure 4b, where a lower decay and then a higher carrier lifetime value can be observed for Post Ox samples. This difference was particularly evident at higher wavelengths or higher penetration depths. It should be remembered that the measurement of the lifetime was strictly linked to the measurement technique used and, in this case, the values obtained with TRPL were greater, as we were in a low injection regime compared to the measurements made with Raman.

Through this analysis, we confirmed the possibility of increment in carrier lifetime after an oxidation process, which also leads to an increase in the diffusion length, obtained by $L_D = \sqrt{D\tau}$, where D is the diffusion coefficient and τ is the lifetime of the excited carrier. Considering a mobility value of 900 cm^2/Vs and a doping concentration of about 10^{14} cm^{-3} (low injection regime), an increment in diffusion length was observed from 712 µm (NO Ox) to 911 µm (Post Ox).

As stated above, carrier lifetime evaluation was conducted far from any SF defects, but they were present in the epilayer, even if in low percentages, and could affect the performances of the devices by increasing the leakage current and decreasing the carrier lifetime. For this reason, a study of the influence of different SF defects on carrier lifetime was performed to estimate if the oxidation process improves the lifetime on and around these defects.

From both maps in Figure 47 showing before and after the oxidation process, it is possible to evaluate the same SF defects in the same position. However, from a thorough analysis, we observed different behavior after the oxidation process for the defects at 490 nm (2.53 eV), compared to the defects at 430 nm (2.88 eV).

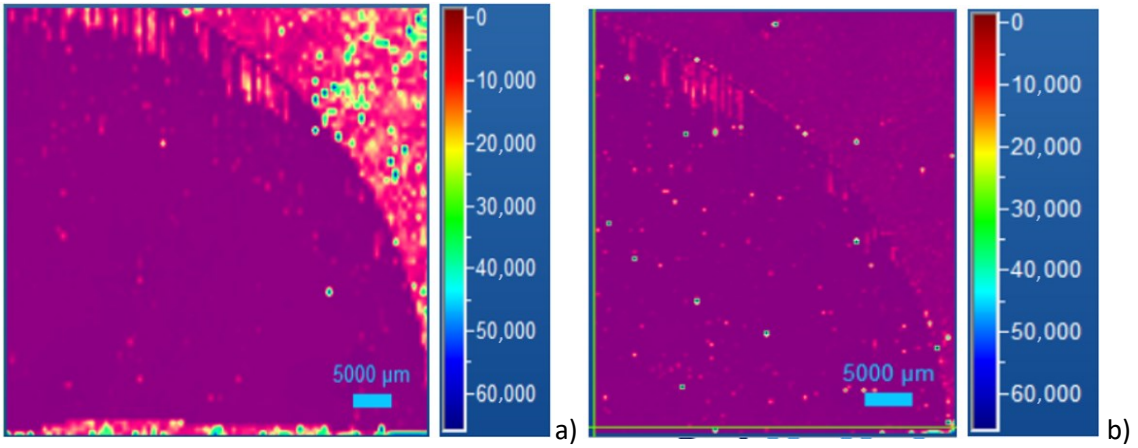

*Figure 47. Photoluminescence map of the same quarter of the 4H SiC wafer highlighted in Figure 30, before a) and after (**b**) oxidation process.*

Both defects show a lower carrier lifetime than the values obtained in the SF-free area and the LO shift difference between IN and OUT SF decreases when the laser power used was decreased, obtaining the same carrier lifetime values for a particular power of the laser. However, this decrement differs depending on the type of defect. As shown in Figure 48, for a 430 nm defect, the Raman maps obtained following the LO peak position show a uniform contrast at 3.8 mW, which are the same results of the non-oxidated sample for the same defect.

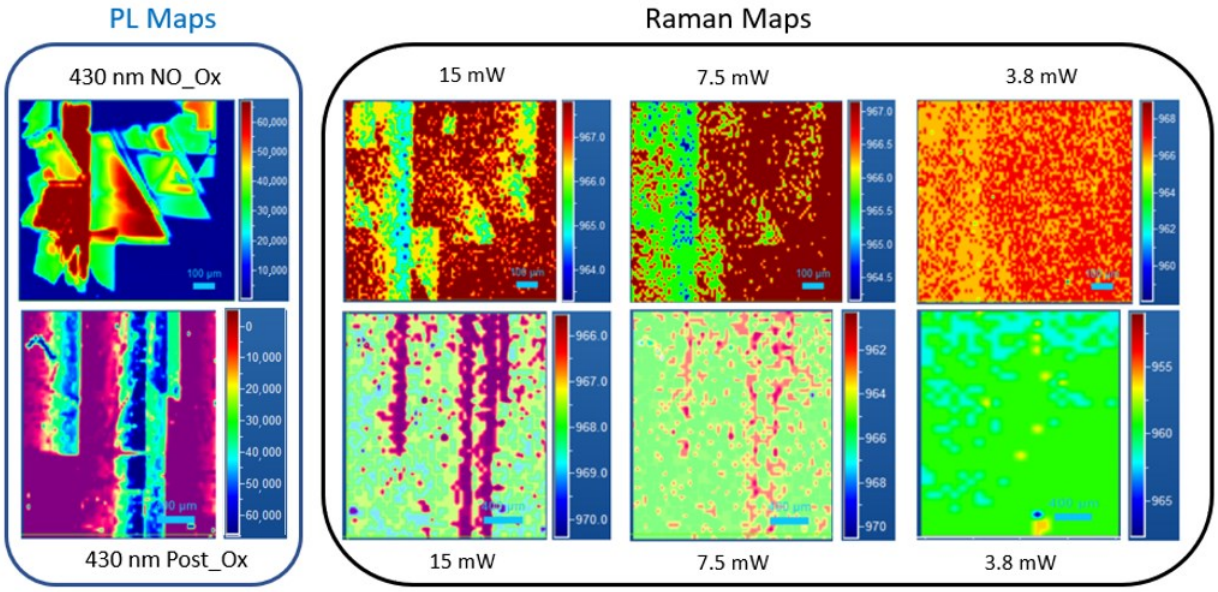

Figure 48. PL and Raman maps of an isolated defect at 430 nm No_Ox (upper strip) and Post OX (lower strip) for different induced carrier values related to the laser power used (15–7.5–3.8 mW, respectively) following the LO peak position.

Instead, for the 490 nm defect, it was observed that when using 15 mW of laser power, the data acquired on the SF defect showed a strong Raman shift reduction, suggesting a trapping of free carriers. Before the oxidation process, both defects analyzed were observed, and under 3.8 mW, there are no differences between IN and OUT SF spectra; instead, it was different for the oxidated sample, where a larger contrast was observed.

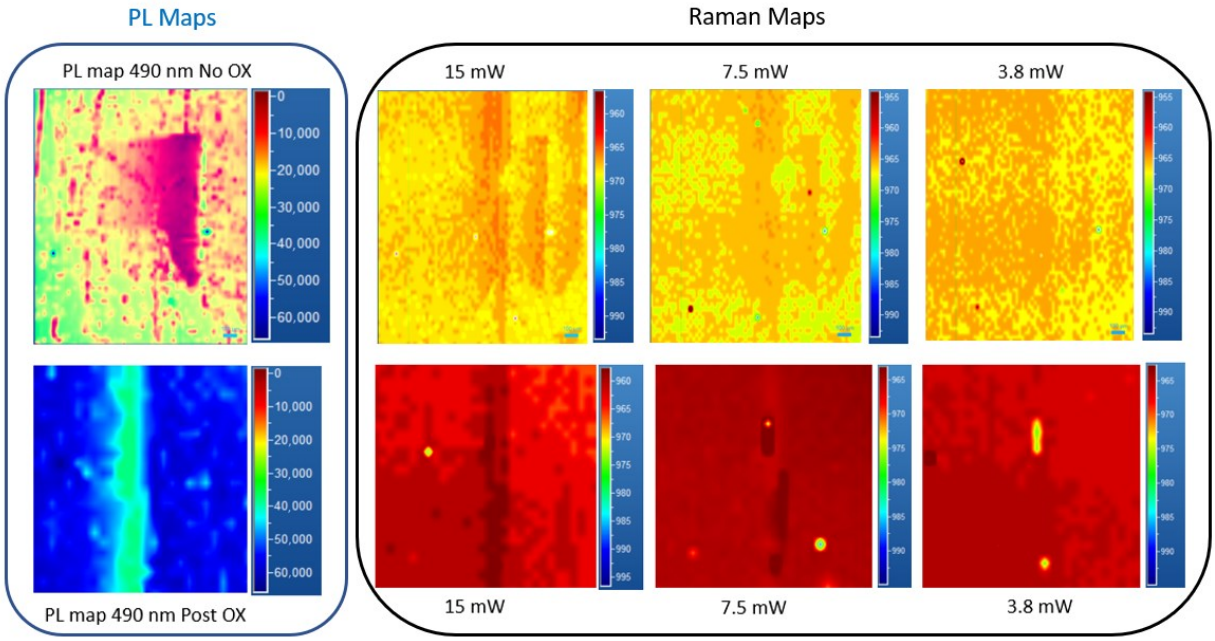

Figure 49. PL and Raman maps of an isolated defect at 490 nm No_Ox (upper strip) and Post OX (lower strip) for different induced carrier values related to the laser power used (15–7.5–3.8 mW, respectively) following the LO peak position.

Figure 49 shows, as in the previous figure obtained for 430 nm SF, PL and Raman maps of a 490 nm SF defect related to the laser power used. It is evident that, moving to a low injection region, the influence of the SF defect on carrier lifetime decreased. This effect is more evident for the oxidated sample, where a minor influence on the part of the SF was observed, as is shown in Figures 48 and 49. This suggests that the same values of carrier induced, and the lifetime IN and OUT, of the defect (in proximity) are obtained when low laser power is used. This difference is more evident in Figure 50.

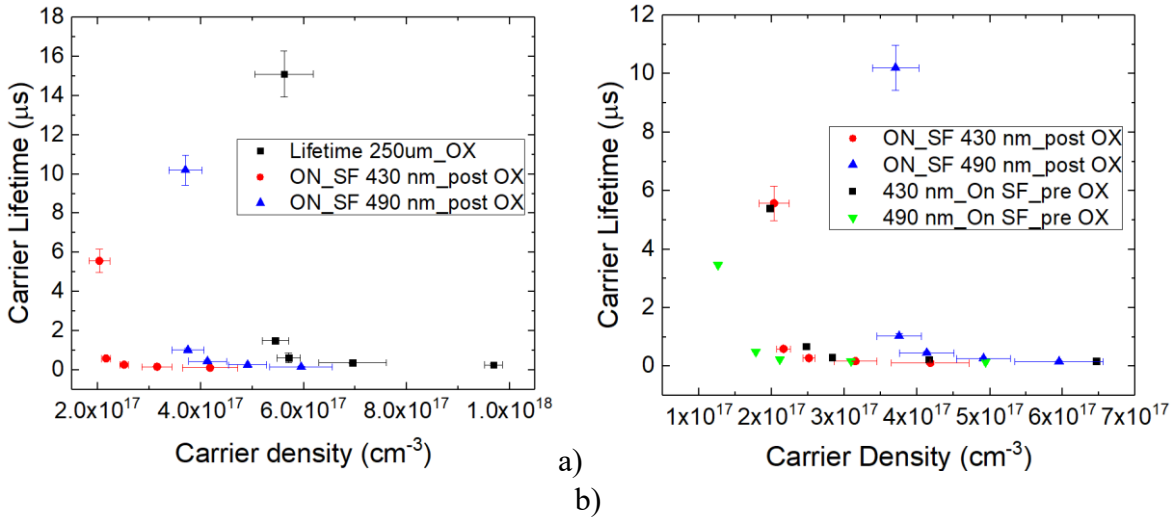

*Figure 50. Carrier lifetime as a function of carrier induced. Comparison between SF-free area and defective zone (**a**); comparison between the same defects (430–490 nm) before and after oxidation process (**b**).*

From these results, it is evident that the oxidation process leads to an improvement in the carrier lifetime. Moreover, not all the stacking fault defects undergo the same improvement. Considering the lifetime, the 490 nm defect is much more influenced by the oxidation process than the 430 nm. In fact, the 490 nm SF shows a large increase in the carrier lifetime at induced carriers of about $4 \times 10^{17}/cm^{-3}$ after the oxidation process; before this process, the increase in carrier lifetime is around $1.5 \times 10^{17}/cm^{3}$ (Figure 49b). Instead, in the case of the 430 nm SF, the increase in the carrier lifetime remains the same, at the same induced carrier conditions [185].

Despite this different behavior of the defects, even after oxidation, they lead to a decrease in the lifetime, compared to the SF-free areas (Figure 50a), leading to a recombination or trapping of the free carriers. In fact, it is clearly shown in Figure 49a that the induced carriers, at which a large increase in the carrier lifetime is observed, increases with respect to the region without SFs both for the 430 and the 490 nm SFs. It seems that the 490 nm SF is less efficient in the reduction in the carrier lifetime, with respect to the 430 nm.

4 Chapter 4: Fabrication, electrical characterization and detection test of devices

4.1 Design and Fabrication process

The manufacturing process of the prototype devices required some initial planning. First of all it is important to check the voltage necessary for the operation of the device in order to avoid a possible break down phenomenon. When a very high electric field is applied to a pn junction or Schottky barrier in the reverse-bias direction, the leakage current increases as a result of generation of electron–hole pairs, and the junction eventually breaks down. The breakdown mechanisms can be classified into avalanche breakdown and Zener (tunneling) breakdown [186]. For junctions with a lightly doped region, avalanche breakdown is dominant; this is the case for most power devices and detectors. In avalanche breakdown, the carriers can gain enough energy under very high electric fields to excite electron–hole pairs by impact ionization. The generation of electron–hole pairs is multiplied inside the space-charge region of a junction, eventually leading to breakdown.

A semiconductor junction breaks down when the maximum electric field strength reaches a critical value which is inherent to the material. This critical value is called the critical electric field strength or breakdown electric field strength. The critical electric field strength E_B can be determined by calculation of the ionization integral using the impact ionization coefficients [73]. Alternatively, it can be obtained experimentally from the breakdown characteristics of devices in which electric field crowding is perfectly suppressed. In n-type Schottky barrier diodes or a one-sided p^+n junction, the breakdown voltage V_B is given by:

$$V_B=\varepsilon_s E_B^2/2qN_D$$

Here a punch through structure is considered. ε_s is the dielectric constant of a semiconductor.

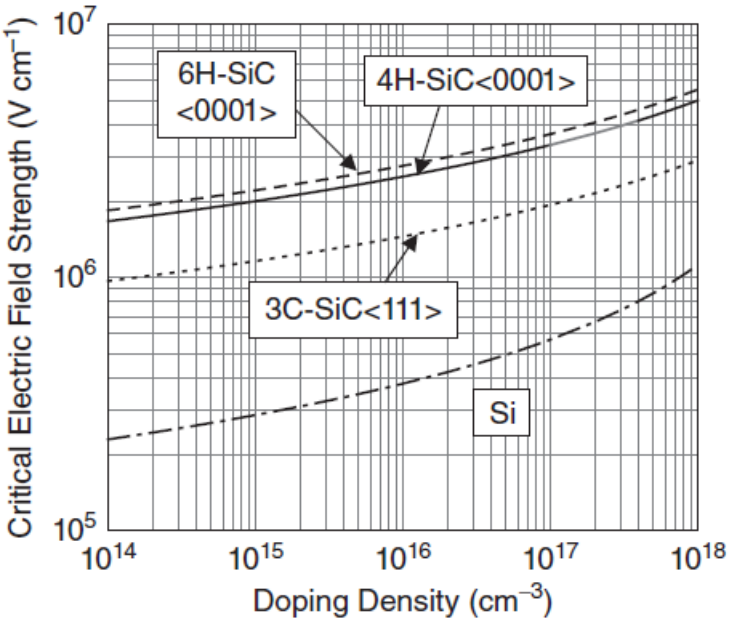

Figure 51. Critical electric field strength versus doping density for 4H-SiC<0001>, 6H-SiC<0001> and 3C-SiC <111>.

Figure 51 shows the critical electric field strength versus doping density for 4H-SiC <0001>, 6H-SiC <0001>, and 3C-SiC <111> [187] [188] [189]. The data for Si are also shown for comparison. 4H- and 6H-SiC exhibit approximately eight times higher critical electric field strengths than Si at a given doping density, while the field strength of 3C-SiC is only three or four times higher because this polytype has a relatively small bandgap (similar to GaP). The high critical field strength of hexagonal SiC polytypes is the main reason why SiC is very attractive for power device applications [190] [191]. One must be aware of the fact that the critical field strength is strongly dependent on the doping density, as shown in above. When the doping density is increased, the width of the space-charge region becomes small and the distance for carriers to be accelerated becomes short. Furthermore, the mobility is reduced in highly doped materials because of enhanced impurity scattering. These are the reasons why the critical electric field strength apparently increases with increasing doping. The critical field strength is a convenient physical property when the ideal breakdown voltage is estimated. However, it should be noted that the critical field strength is valid only for junctions with non-punch through structures. When punch through structures is considered, the critical field strength shown in Figure 51 does not give the correct breakdown voltage. In this case, simulation of leakage current or calculation of the ionization integral using a device simulator is required to determine the ideal breakdown voltage.

Therefore, the voltage applied is fundamental parameter to avoid reaching the critical electric field.

The planning of the fabrication process was done, designing the detector structure also by Comsol simulations to obtain the edge structure to avoid a possible devices failure. The design of the detector structure was defined, with a field plate edge structure for the first version of the detectors, considering layer by layer interaction as shown in the figure 52.

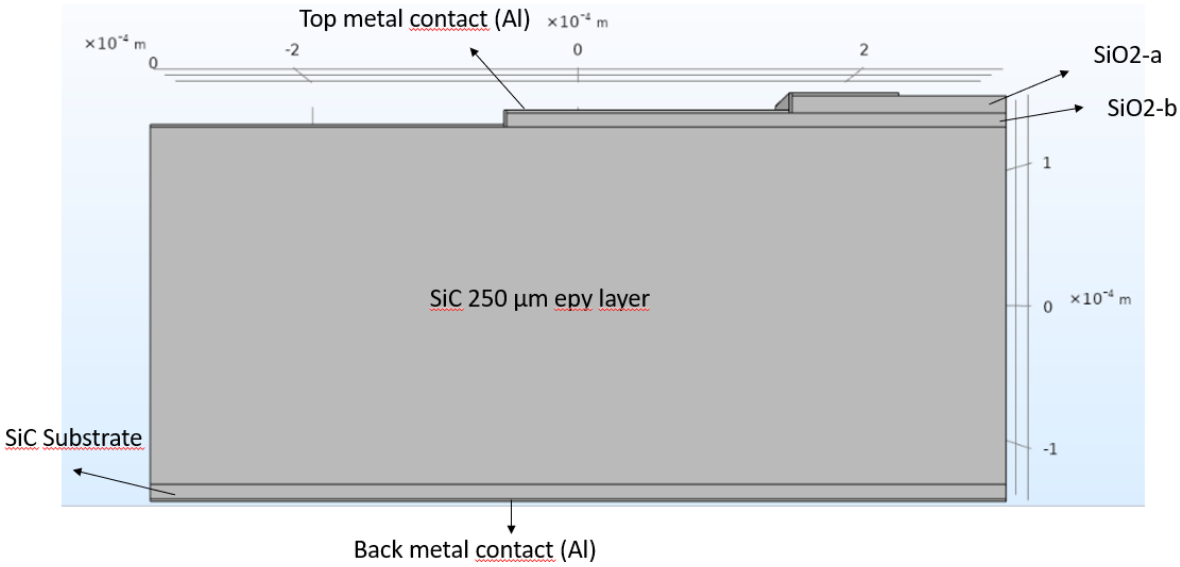

Figure 52. Design of the edge structure of the devices for the Comsol simulation.

A study of the necessary voltage for the complete depletion of the entire thickness was obtained and, for a thick epitaxial layer (250 µm), obtaining a value of around 5000V using the following equation:

$$W=\sqrt{2\varepsilon sVd/qND}$$

Where W is the depletion layer, ε_s is the dielectric constant of the semiconductor, V_d is the built-in potential and N_D represents the doping value [73]. The necessary voltage for a complete depletion across the entire epi-layer is:

$$V= W^2qN_D/2\varepsilon_s=4708{,}1V \sim 5000V$$

At this working voltage the critical electric field for the silicon carbide could be reached so, an edge structure was studied in order to avoid the break down phenomenon.

The Figure 53 shows the study of the breakdown field to understand the optimal thickness of silicon dioxide used in the edge structure.

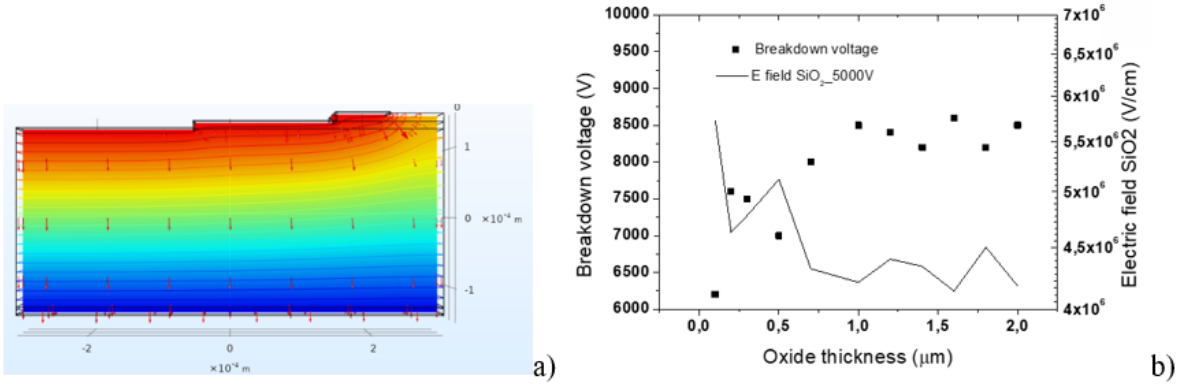

Figure 53. Comsol simulation to study the edge structure with field plate of the first detector version.

The red arrows show the intensity of the electric field that are more intense on the edge of the metal contact. As is shown, the better silicon dioxide thickness is around 1 µm, considering the breakdown electric field for 4H-SiC and SiO_2, $3 \div 5 \times 10^6$ V/cm and 7×10^6 V/cm respectively.

After the edge structure optimization, the masks design was defined, and the fabrication flow was started following the scheme in Figure 54.

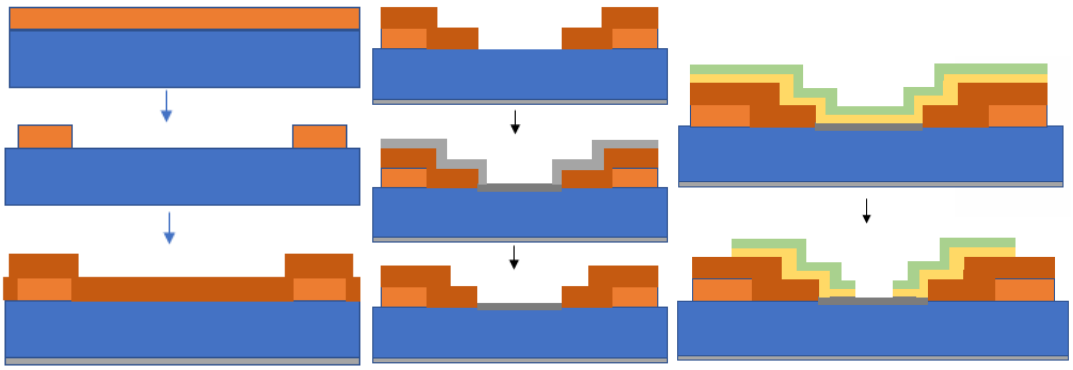

Figure 54. Process flow for the Schottky devices.

The process flow for devices manufacturing was done, making sure step-by-step that everything was fine. The detectors in a quarter of the wafer were fabricated and they are shown in Fig. 55.

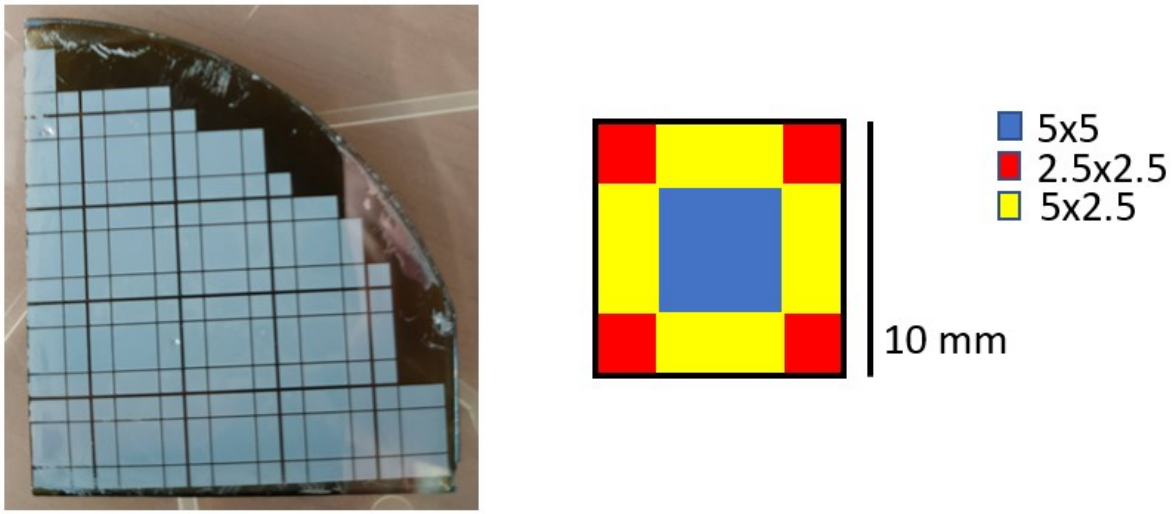

Figure 55. Detectors fabricated on a quarter of 4 inches 4H-SiC wafer with a matrix containing nine detectors with three different dimensions.

A matrix with three different areas was designed (5x5, 5x2.5, 2.5x2.5 mm) in order to compare, under working conditions, the influence of the dimension, hence the total volume, on the detector yield.

The detectors on wafer (before the dicing) were tested in order to evaluate the leakage current and the correct functioning and the results are shown in figure 55. The leakage current values resulted low (around 10^{-9} A) for almost all the detectors analysed. Some of the big detectors (5x5) showed a higher leakage current value, probably due to the higher probability of defects in the epi-layer volume. The doping concentration was also evaluated obtaining a low value of $N_D = 1.4x10^{14}$.

Moreover, a second generation of detectors was designed with a more complex structure in order to obtain a lower leakage current, as shown in figure 56.

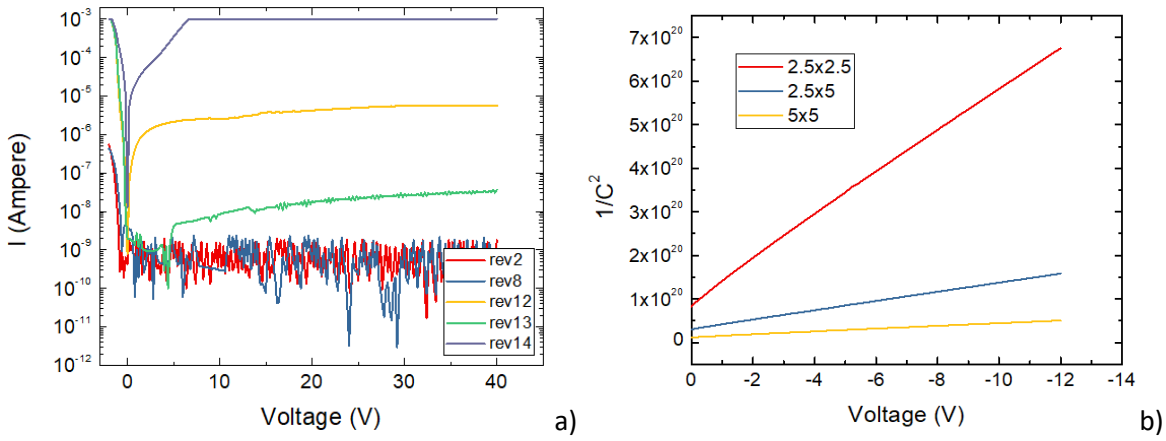

Figure 56. (a) I-V measurements on wafer in reverse bias from -40 V to 0 V for the devices fabricated. (b) Capacitance measurements in order to evaluate the doping concentration.

The KLayout software was used to define the step flow layout for the fabrication process. The process was performed by Ion Beam Services (IBS), France.

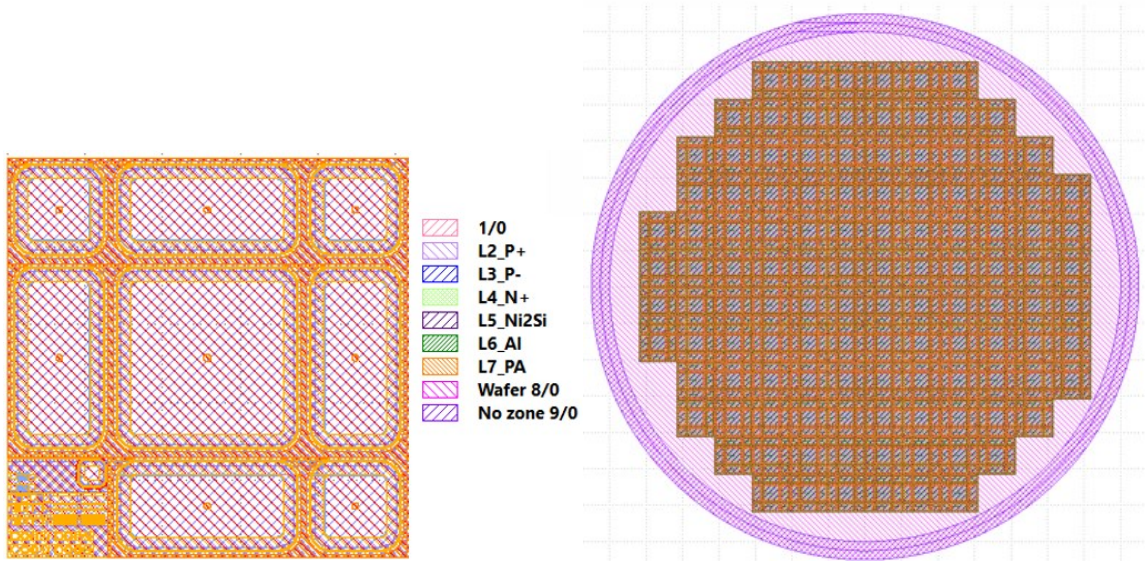

Figure 57. (a) The matrix layer-by-layer designed containing the test pattern area and (b) the same matrix repeated on a 6 inches wafer.

The figure 57 shows the project of for the flow chart fabrication process and, as the first-generation detectors, with a matrix of 9 dices with three different dimensions. Figure 56a shows the layer-by-layer matrix containing the test pattern area, and in figure 56b this matrix is reported on a 6 inches wafer.

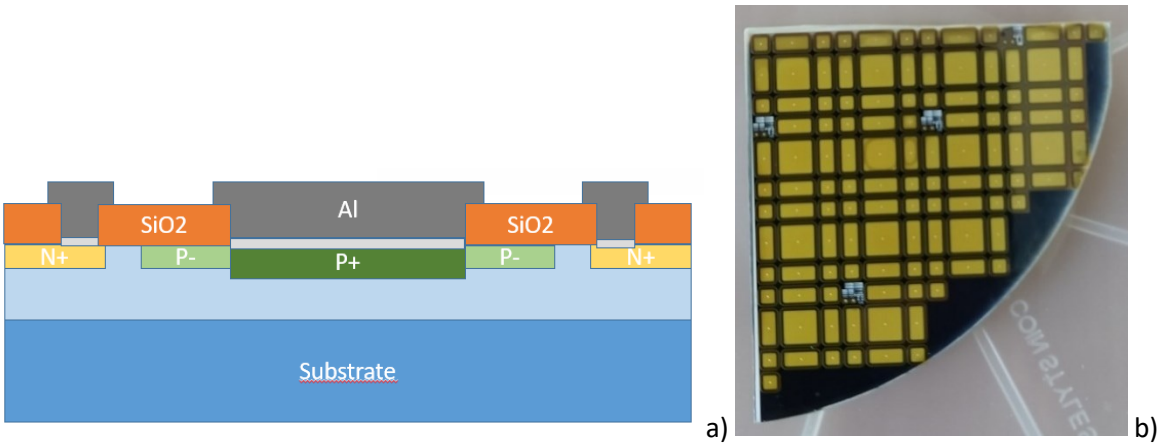

Figure 58. (a) Design of the cross section for the second-generation detectors; (b) The detectors fabricated on a quarter of 4 inches wafer with a 250 micron of epitaxial layer.

As is shown in the figure 58a, the detectors structure is more complex than the first-generation detectors in order to increment the detector performances and to obtain a more robust edge structure to avoid breakdown phenomena. However, even though the fabrication process is more complex than that of first-generation devices, it was performed and the result is shown in figure 58b. The yellow colour is due to the polyimide layer, which isn't shows in the cross-section scheme, used as passivation layer.

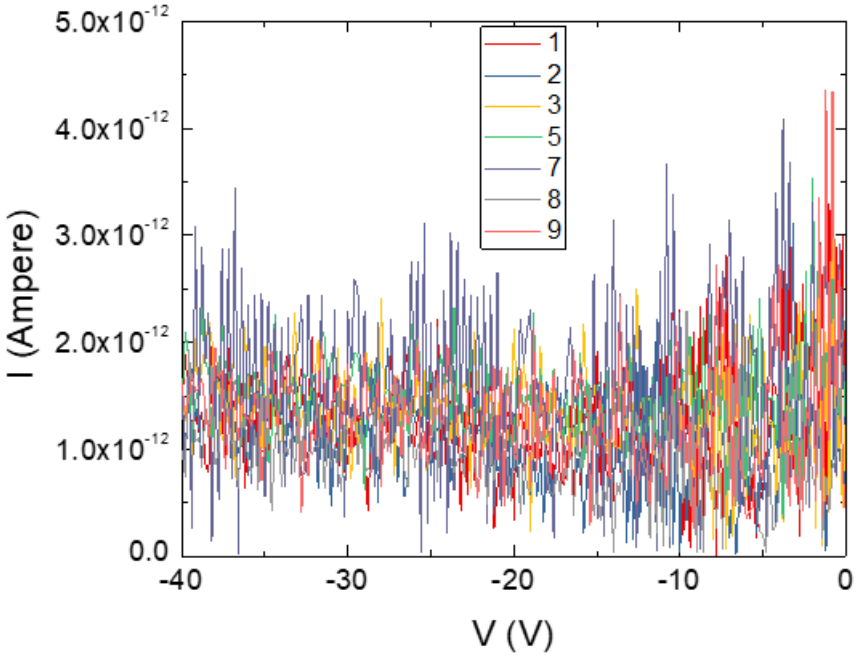

Figure 59. I-V measurement on wafer in reverse bias, from 0 to -40 V.

As is shown in figure 59, despite the more complex fabrication process, the leakage current measured on wafer result lower (~ 10^{-12} A) than the previous detectors thanks to the better edge structure designed.

4.2 Electrical characterization

Finally, cutting and bonding of the detectors was performed, then I-V and C-V tests were performed to evaluate the reliability and the detector characteristics such as doping concentration, that is fundamental to understand the real voltage for the depletion of the whole epi-layer.

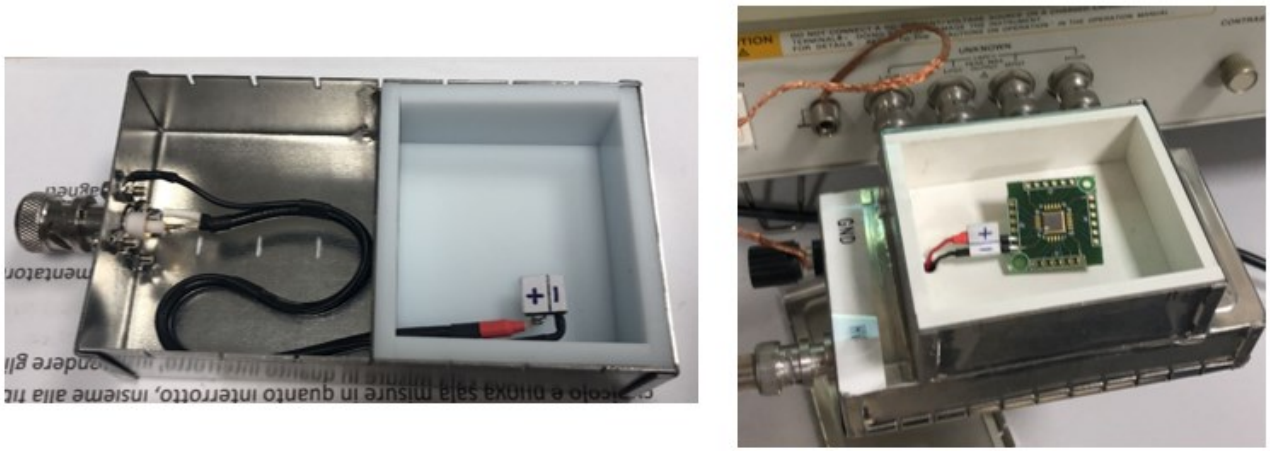

Figure 60. Two boxes used for I-V (left side) and CV (right side) measurements respectively.

As is shown in figure 60, two boxes were made to make low noise I-V and C-V measurements. In particular, through the structure on the right it is possible to perform C-V up to 1100 V.

Capacitance–voltage profiling (C–V profiling) is a technique for characterizing semiconductor materials and devices. The applied voltage is varied, and the capacitance is measured and plotted as a function of voltage. The technique uses a metal–semiconductor junction (Schottky barrier) or a p-n junction or a MOS to create a depletion region, a region which is empty of conducting electrons and holes but may contain ionized donors and electrically active defects or traps. The depletion region with its ionized charges inside behaves like a capacitor. By varying the voltage applied to the junction it is possible to vary

the depletion width. The dependence of the depletion width upon the applied voltage provides information on the semiconductor's internal characteristics, such as its doping profile and electrically active defect densities. Measurements may be done at DC or using both DC and a small-signal AC signal or using a large-signal transient voltage.

The Fig. 61 shown the electrical scheme of the box used for C-V measurements.

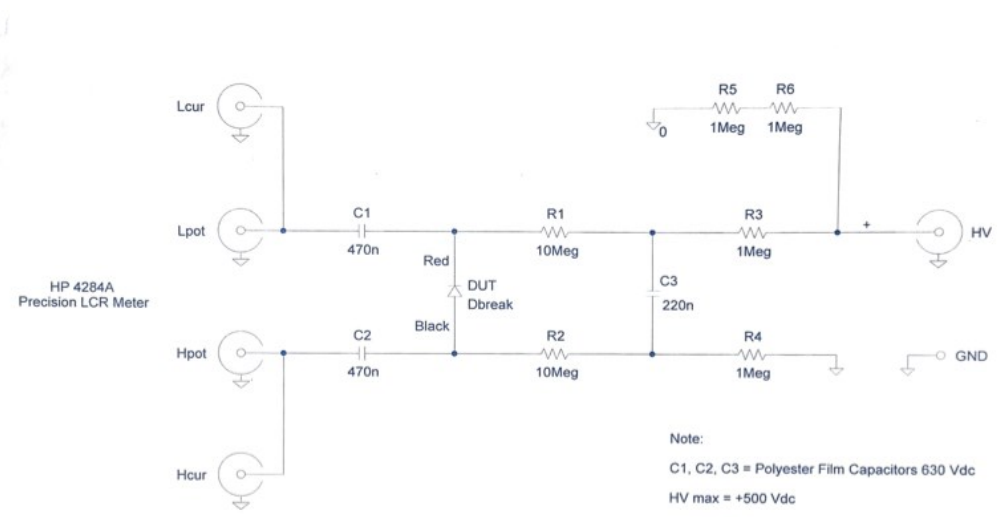

Figure 61. Electrical scheme of the box for C-V measurements.

The C–V measurements on Schottky structures give the net doping density, which is $N_D - N_A$ for n-type and $N_A - N_D$ for p-type, where N_D and N_A are the donor and acceptor densities, respectively. Because of the relatively large ionization energies of acceptors in SiC, C–V measurements on p-type SiC give very different values for the densities ($p < N_A - N_D$) at room temperature. Only the hole density changes when the measurement temperature is changed, while the net doping density remains almost constant, as expected.

In C–V measurements, Schottky barriers are formed by deposition of metal electrodes on top of the SiC samples. The net doping density can be determined from the slope of a $1/C^2 - V$ plot. If the doping density is not uniform throughout the depth, then the depth profile of the doping density can be obtained from the differential slope of the plot. In this case, the monitored depth (d) is simply determined from $d = \varepsilon_s / C_d$. Here, ε_s and C_d are the dielectric constant and the depletion capacitance per unit area of the semiconductor, respectively. Because this sample structure consists of a Schottky barrier and a series resistance (RS), selection of the probe frequency requires care. For accurate measurement of the capacitance of the space-charge region, C, it is important to satisfy the condition $\omega C R_S \ll 1$, where ω is the angular probe frequency in the C–V measurements. For example, the probe frequency

must be lowered in C–V measurements of lightly-doped p-type SiC because of the relatively high series resistance.

The capacitance of the space-charge region of Schottky barrier diodes (SBDs) (n-type) per unit area is given by:

$$C = \sqrt{\frac{\varepsilon_s q N_D}{2(V_d - V)}}$$

where N_D is the donor density and ε_s, as previously defined, the dielectric constant of the semiconductor. Squaring and inverting this equation, one obtains:

$$\frac{1}{C^2} = \frac{2(V_d - V)}{\varepsilon_s q N_D}$$

By plotting $1/C^2$ versus the bias voltage, the built-in potential (V_d) can be determined from the V-intercept of the plot.

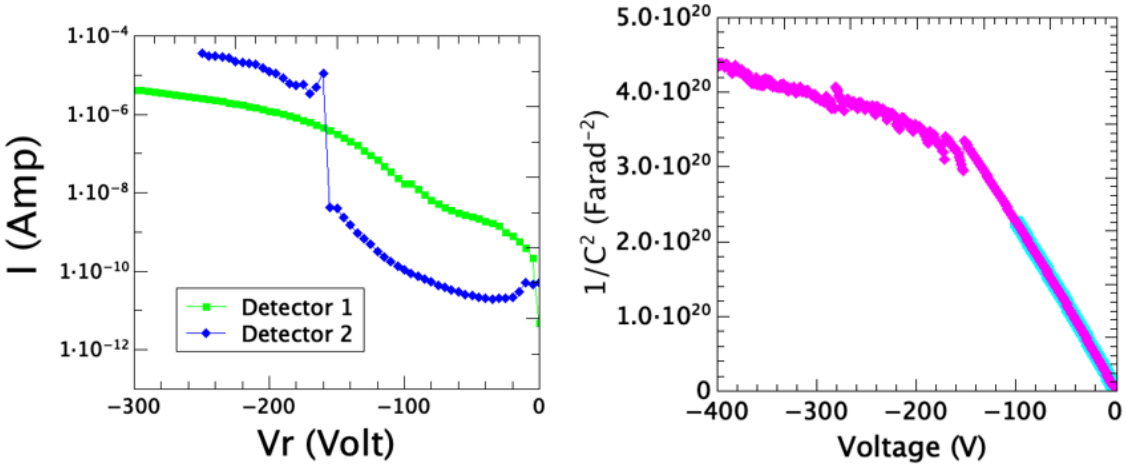

Figure 62. I-V and $1/C^2$-V graph for two (5x5 mm²) of the first generation SiC detectors fabricated on CNR-Imm institute.

As is shown in Figure 62, $1/C^2$ versus bias voltage and I-V measurements for the biggest detectors (5x5 mm^2) fabricated was performed. The leakage current and the doping density for our detectors were evaluated obtaining a low value of $N_D = 9.7\text{x}10^{13}$ and a built-in potential of $V_d = 1.53$ eV. The doping density is uniform in the epitaxial layer (straight $1/C^2$ vs. voltage characteristics) but when the leakage current exceeds $1\text{x}10^{-6}$ A, the $1/C^2$ vs.

voltage plot changes its slope due to the high RC of the used circuit (Fig. 61) for the measurements.

Should be highlighted the low N_d value obtained thanks to the improvements on the epitaxial growth process, as previously mentioned, and necessary in order to use a possible lower depletion voltage.

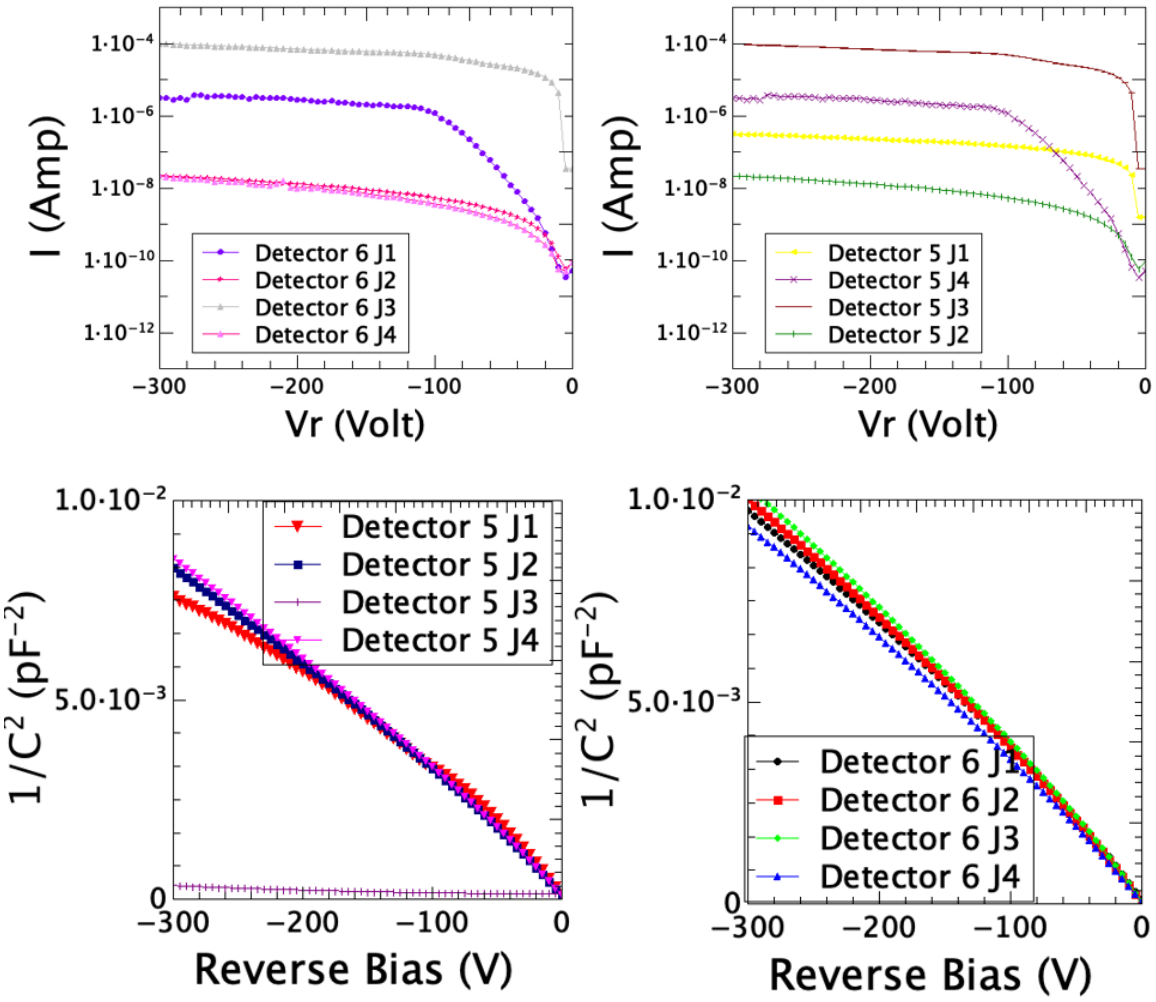

Figure 63. Comparison of I-V and C-V measurements between big (5x5 mm²) and small (2,5x2,5 mm²) detectors.

However, as is shown in the Figure 63, where I-V and C-V measurements for the 2.5x2.5 mm^2 detectors are showed, it is clear that the leakage current values are lower than the 5x5 mm^2 detectors, showed in Figure 62. This is due to the fact that larger is the detector area, more likely is that are defect inside which lead to a higher leakage current. At the same time, it is possible to observe that when the leakage current of the detectors is lower, due to the

smaller area, also the $1/C^2$ vs. reverse bias is much more linear giving an almost constant doping concentration in the epitaxial layer. The value of the doping concentration in this case is of the order of 10^{13} too.

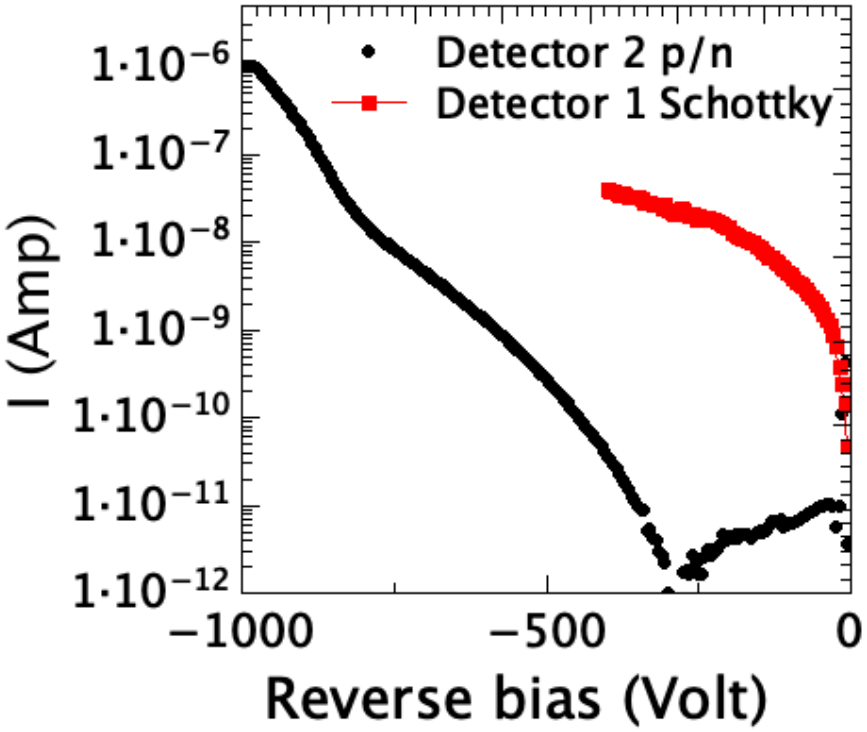

Figure 64. Comparison of I-V measurement beetween first (Schttky) and second (p/n) generation of the fabricated detectors.

As is shown in fig. 64, the I-V measurement for the second generation detector, peaviosly designed with Klayout software and then fabricated by IBS, is compared to the Schottky detector (first-generation). An important improvement is observed with this new design of the detectors which manages to bias the detector to much higher voltages in the reverse direction thus allowing to obtain a much larger depletion region. Therefore, the second generation detectors should allow us an higher sensitivity and resolution for the neutron detection than the first generation detectors. Moreover, as described before, others benefits are related to a stronger edge structure and lower leakage current than the first generation detectors, despite the more complex fabrication process.

4.3 Neutron detection

The SiC detectors fabricated will be tested under working conditions for different responses as neutrons and alfa-particles detection. The use of wide-band-gap solid-state neutron detectors is expanding in environments where a compact size and high radiation hardness are needed, such as spallation neutron sources and next-generation fusion machines. Silicon carbide is a very promising material for use as a neutron detector in these fields because of its high resistance to radiation, fast response time, stability and good energy resolution. In a previous work [192] measurements were performed with neutrons from the ISIS spallation source with two different silicon carbide detectors together with stability measurements performed in a laboratory under alpha-particle irradiation. In addition, the detector response to Deuterium-Deuterium (D-D) fusion neutrons was evaluated by comparing neutron measurements at the Frascati Neutron Generator with a GEANT4 simulation.

Solid State Detectors (SSDs) represent a recent option for neutron detection in high-flux applications, since they combine a good pulse height energy resolution and fast response time while having compact dimensions [193]. The SSD scene is currently dominated by diamond detectors, which, for instance, are currently installed at the JET tokamak [194] as neutron spectrometers [195] and at the ChipIr beamline at ISIS [196] as beam monitors [197].

However, the development of large high-power tokamaks (such as ITER [198]) requires neutron detectors to be installed closer to the plasma and, therefore, to be able to sustain the high temperature and neutron flux of such an environment. This is driving interest in new and more neutron-resilient SSDs, such as silicon carbide detectors.

The tokamak is a toroidal (donut shape) nuclear fusion reactor in which a plasma (usually hydrogen) at very high temperature and low pressure is kept cohesive and away from the internal walls thanks to a magnetic field generated by electromagnets outside the chamber. Under suitable conditions it has been shown that it is possible to create the conditions for a controlled thermonuclear fusion inside it, in order to extract the energy produced by the fusion of the nuclei of light atoms. Excellent results have been achieved with JET and new results are expected from the entry into operation of ITER and SPARC. By requiring an enormous amount of energy to bring the plasma to temperatures of several tens of millions of kelvins and to operate the reactor's confinement electromagnets and auxiliary systems, the ability of any plant to produce more electricity than it consumes remains to be demonstrated.

The first experiment was performed on two SiC detectors with different epi-layer thickness fabricated by CNR-imm in Catania. The first detector used was made with a single active volume 5 mm x 5 mm wide and 10 µm thick. The second was made of a 2 x 2 matrix of independent 5 mm x 5 mm wide and 100 µm-thick active volumes, all grown on the same substrate.

An important parameter is the detector stability that is the capability of a detector to operate for long irradiation times without altering its response. There are several factors that can alter the response of an SSD, the main one being that the prolonged exposure to ionizing radiation results in free charges trapped inside the lattice that alter the drift electric field. As mentioned in the introduction section, diamond detectors have shown to be subject to this effect [5]. This is an issue even if the restoration of the initial condition can be achieved by an inversion in the polarity of the detector [199] since it is desirable for a detector in a fusion or spallation environment to be able to operate continuously.

The results of the detector stability under α-particles irradiation are listed in table 11, the energy resolutions obtained were 4.3% for the SiC-10 and 2.9% for the SiC-100, the latter confirming the resolution obtained in [200] and in [199].

Table 11. Summary of the mean number of counts, pulse height and energy resolution measured

	Mean No. of Counts, μ	**Dispersion (σ)**	**Poisson Uncertainty ($=\sqrt{\mu}$)**
SiC10	36,460.55	±195.02	190.95
SiC100	94,737.97	±313.11	307.80
	Mean Pulse Height	**Dispersion (σ)**	**Max PH—Min PH**
SiC10	7995.52	±8.09	-
SiC100	9672.03	±27.60	9709 − 9625 = 84 (0.87%)
	Mean Energy Resolution	**Dispersion (σ)**	
SiC10	4.356%	±0.113%	-
SiC100	2.893%	±0.036%	-

These results are promising because this trend should be increased with our thicker SiC detectors (250 µm).

Both detectors were also tested with fast spallation neutrons at two different ISIS facilities and proven to have stable response functions after around 10^9 n/mm^2 of neutron irradiation. This stability, which is orders of magnitude longer than the stability proven for diamonds in [5], makes the SiC a good candidate as a neutron counter or spectrometer for installation in the harshest environments, such as the breeding blankets of next-generation tokamaks. In

order to achieve this, the functionality of the electronic chain, mainly, the preamplifier, will have to be tested in the future under similar levels of irradiation. An alternative could be to couple the SiC to a preamplifier capable of operating far away from the detector, as done for diamond detectors.

Moreover, SiC detector was tested with D-D quasi-monochromatic neutrons in order to complement the work in [8].

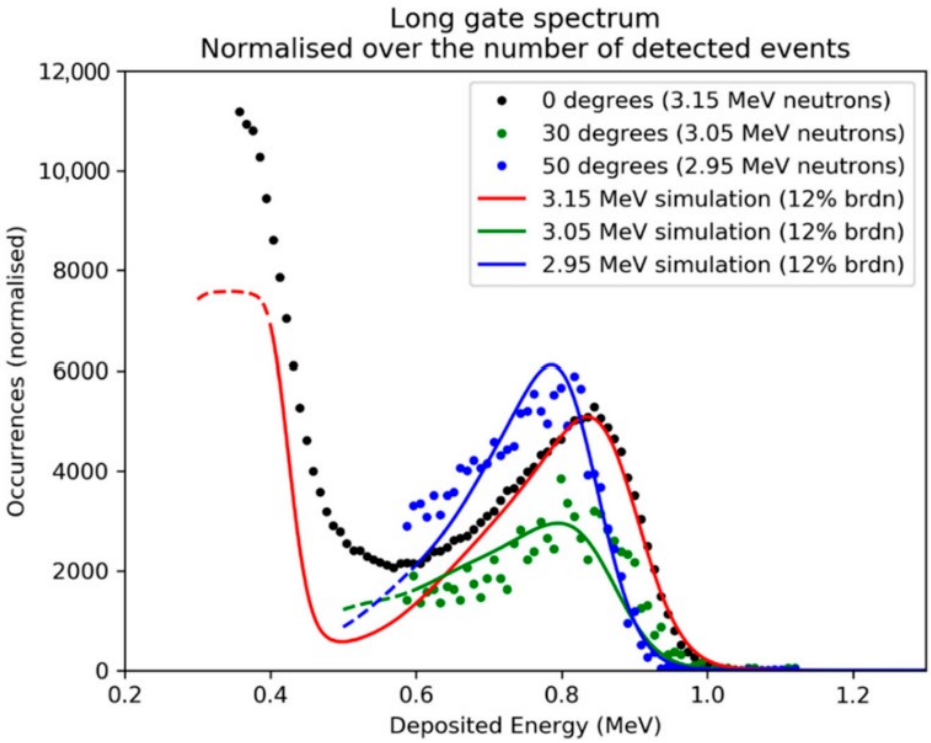

Figure 65. Deposited energy spectra for three different neutron energies at the FNG (3.1, 3.05 and 2.95 MeV). The number of events is normalized. The three sets are compared to three GEANT4 simulations, simulating 3 x 10^8 monochromatic neutrons. The simulated spectra obtained were broadened through a Gaussian convolution with FWHM = 12% of the energy value, in order to emulate the detector's energy resolution. Simulations are plotted as continuous lines and normalized to fit the data [192].

Three energies in the vicinity of En = 3 MeV were tested, showing elastic scattering on carbon to be the most robust detection mechanism. The spectra were compared to an ideal simulation with a 12% energy resolution broadening, finding a good agreement. This confirms the possibility of using the SiC as a spectrometer for D-D neutrons.

A comparison of these result with two of our thicker SiC detector (First generation 250 µm) was performed. As mentioned before, we obtain that the potential needed to fully deplete the 250 µm active volume is 4600 V. Such high voltage is unachievable at present date, due to the limits imposed by the preamplifier; as such, it was chosen to conduct a preliminary

alpha particle irradiation on a partially polarized SiC in order to test its functionality, obtain the energy resolution of the new detector and evaluate its stability, similarly to what was performed in [193]. Since the alpha particle source chosen was an Americium-241 source (emitting alphas with energy $E_\alpha = 5.49$ MeV, which are then slowed down in air) a 100 V bias was chosen in order to deplete 36.7 μm of the detector, which is deep enough to fully stop the alpha particles, more detail on the electric chain and the experimental setup are showed in [202]. Following the same process performed in [193] the signals detected were grouped up in five-minute spectra, on which a double fit was performed: first a gaussian fit on the entirety of the spectrum is performed, identifying the center of the gaussian; afterwards a second gaussian fit is performed only on the higher energies of the gaussian (the right side), using the first fit results as a starting guess. From the fit three information are extracted:

- Number of counts every five minutes, which is proportional to the detector efficiency to alphas.
- Center value of the gaussian, which gives information about the response function.
- Full width at half maximum of the gaussian (FWHM), obtained from the σ of the gaussian fit via FWHM $= 2\sqrt{2 \cdot ln2} \cdot \sigma$.

The goal is to demonstrate the stability of the detection by proving that the three quantities above do not change as a function of time and irradiation. By dividing the FWHM by the center value of the gaussian, a first estimate of the energy resolution of the setup (SiC250 + new preamplifier) can be obtained.

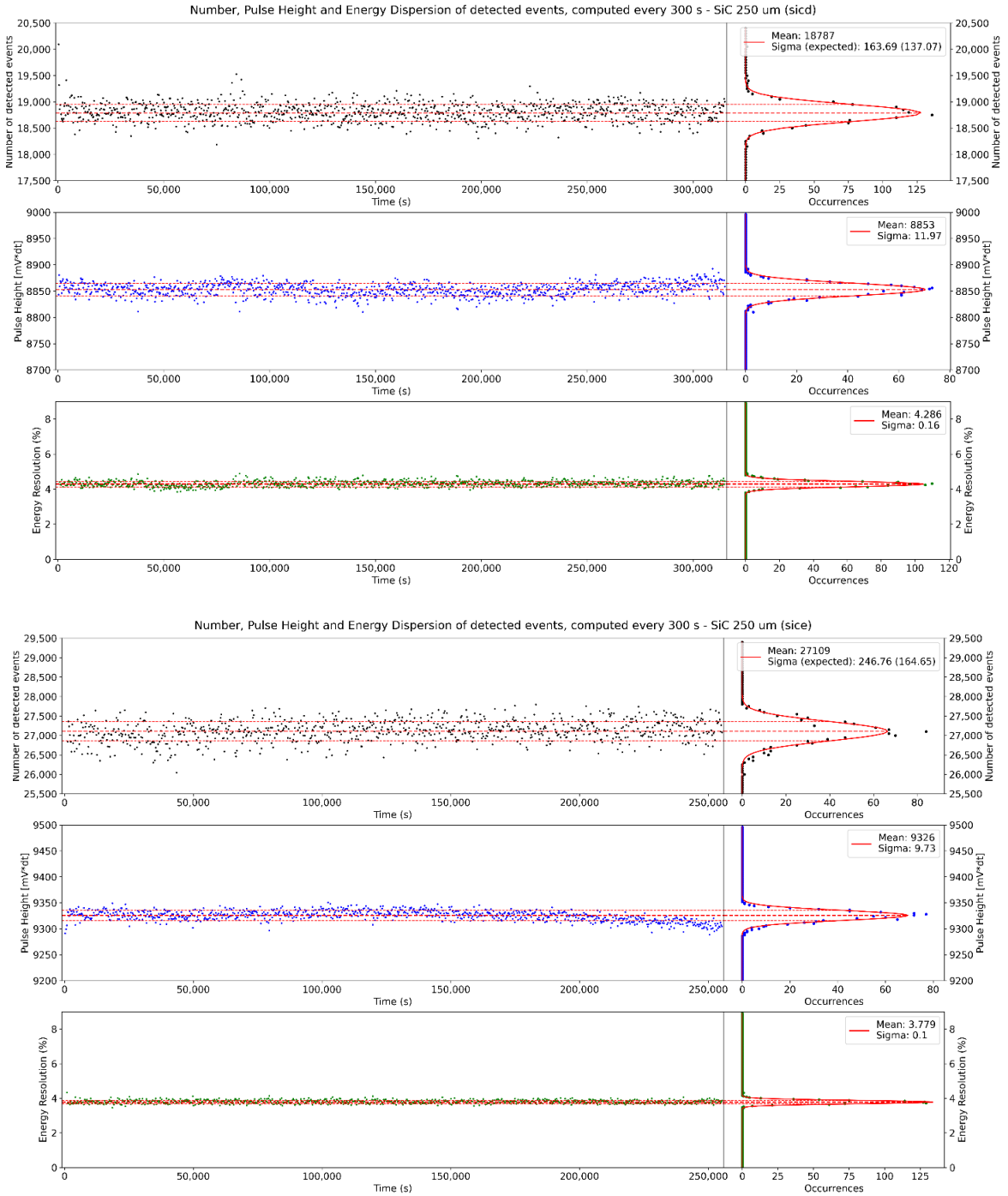

*Figure 66. Time evolution of the number of counts (**black**), the mean pulse height (**blue**) and the energy resolution (**green**) for the three SiC250, SiCA (**top**), SiCD (**middle**) and SiCE (**bottom**), under irradiation of monochromatic alpha particles (3.81 MeV, 4.17 MeV and 4.69 MeV respectively). Each of the points correspond to a 300s ensemble, the entire irradiation lasting for between 48 and 72 hours. On the right, the dispersion of the data is projected on the y-axis, computing the mean value of the three quantities along with its standard deviation. For the number of counts the standard deviation is compared to the expected dispersion due to statistical error (equal to the square root of the number of counts). The figure is the direct analogue of figure 3 from [Kushoro 2021] for the SiC250.*

The value of the number of counts, center value of the gaussian and energy resolution obtained in every five-minute interval is plotted in Figure 65. The absence of drifts in all

three quantities for the two detectors proves the detection stability. The only visible drift is the SiCE pulse height, which slightly declines by about 1.5% in the region between 200 000 seconds to 250 000 second (≃14 hours); the fact that the drift is comparatively small and has no analogue in the two other detectors suggests it could be due to changes in the air stopping power due to humidity or temperature shifts rather than actual variation in the response function of the detectors. This stability, which mm is orders of magnitude longer than the stability proven for diamonds, makes the SiC a good candidate as a neutron counter or spectrometer for installation in the harshest environments, such as the breeding blankets of next-generation tokamaks [5].

By taking the mean value of the energy resolution we can obtain the energy resolution of both detectors, which is reported in the table below. In the same table is also reported the FWHM and the projected value of energy resolution to 14 MeV neutrons if the same FWHM (and, thus, the absolute value of the energy resolution) is kept the same. The same values for SiC100 from [192] are also reported, paired with the energy resolution to 14 MeV neutrons obtained through experiment [200].

Table 12. Comparison of the final energy resolutions among SiCD, SiCE (250 µm) and SiC 100.

Detector Name	Energy Resolution (alpha energy)	Full Width at Half Maximum	Projected Value of Energy Resolution to 14 MeV Neutrons
SiCD	4.30% (4.17 MeV)	179.31 keV	1.28%
SiCE	3.80% (4.69 MeV)	178.22 keV	1.27%
			En. Res. to 14 MeV Neut. (experiment)
SiC100 [Kushoro 2021]	2.89% (4.3 MeV)	124.7 keV	2.7% [Kushoro 2020]

The energy resolution to alphas obtained for all three detectors is higher (and, thus, worse) than the 2.89% value obtained on the SiC100 (corresponding to a FWHM = 124.7 keV). This was not due to the change of preamplifier, since the energy resolution obtained in a 10-minute irradiation performed with the same three detectors while coupled to the preamplifier used in [193] wielded similar energy resolutions results. Instead, the worst performance could be due to dark currents flowing inside the active volume adding to the integral of the signal and therefore broadening its spectrum. Such currents are presumably due to trapped charges into crystal defects [203], which are expected to be more common in thicker SiCs [125] [129].

5 Conclusion

Silicon Carbide (SiC) is used extensively for the production of high-tech semiconductor devices. Today the use of this material in radiation environments such as fusion reactors create excitement in the nuclear experiments. Specific radiation types and energies which semiconductors were frequently exposed and are of great value in terms of high-tech device studies. FLUKA simulation code was used to investigate radiation induced effects in 4H-SiC for different energetic protons, neutrons and photons. It is fundamental to find the right compromise between thickness-depletion layer and diffusion length thickness. As is observed in this work, from these simulations with FLUKA it is possible to define that the efficiency of the detector increases for all materials as a function of thickness. Therefore, high thicknesses and large areas are required to obtain high efficient detectors.

Not only the volume but also the quality of the epi-layer is fundamental for good reliability and the carrier lifetime plays an important role because it can strongly affect the performances of the devices.

The epitaxial growth of a 4H-SiC wafer with a thickness of 250 μm and a deep characterization to evaluate the quality of the epi-layer was performed. For this purpose, we have used room-temperature PL spectroscopy and the micro-Raman spectroscopy by using the i-LOPC method, a non-destructive technique to determine the general quality of epitaxy. As the detector size increases, the yield decreases due to the material defects. With the improvement of substrates and epitaxial growth processes it is possible to reduce defects and improve yield. For the growth process used in this work, a horizontal hot wall reactor was used and a particular attention on several parameters during the growth was evaluated such as temperature (1550–1650 °C), low pressure regime (100 mbar), dopant gas control, Si/C ratio. The epitaxial layers were grown with different Si/H_2 ratios that produce different growth rate. At the starting of the growth, a high doped buffer layer was grown with a thickness of about 5 microns. This buffer layer should remove several defects present in the substrate (dislocations and SFs) and avoid that the depletion layer in reverse bias reach the substrate and then produce a high leakage of the junctions due to the high density of defects of the substrate. The obtained layers were analyzed by Fourier transform infrared reflectance (FTIR) for film thickness determination, and mercury-probe C–V measurements for the doping concentration.

For the carrier lifetime values, different behaviours on different samples depending both on growth rate and thickness were obtained. The induced carrier lifetime is increasing with the

decrement of laser power and also by lowering the carrier density according to the theory and other experimental data.

From our measurements it is clear that the presence of SFs in the material has a large effect at high carrier injection but at low carrier injection it is negligible. The 250 μm sample has a low percentage of SFs defects, but they are located on the left edge of the wafer due to the off-axis angle and epitaxial growth conditions. The low impact of the SFs on the carrier lifetime at low carrier injections is extremely important for the detector applications, where the carrier injection due to the particles is extremely low.

An oxidation process 1400 °C for 48 h was performed evaluating an increment in carrier lifetime especially going towards a low injection regime, that is the regime where the detectors will be under working conditions. This phenomenon is also supported by the low impact of the SFs on carrier lifetime at low carrier injection that became important for detector applications, where particles induce a very low carrier injection.

The carrier lifetime essentially depends on the concentration of $Z_{1/2}$ defects. The lower is this concentration, the longer is the lifetime of the carriers. DTLS measurements was performed before and after the oxidation process showing an important decrement of $Z_{1/2}$ defects after the process due to the carbon interstitials injection that led to a decrease of carbon vacancies. These results were confirmed by TRPL which shows the increment of the carrier lifetime after the oxidation process. Moreover, TPRL allows us to make a depth profile of the lifetime and it was found that the oxidized sample has a greater uniformity of the lifetime, especially near the interface with the substrate.

Furthermore, the oxidation process influences in different way the kinds of SFs analysed, where the 490 nm defect increase the carrier lifetime value compared to the value of non-oxidated sample, while the 430 nm does not seem to be affected by the oxidation process.

Despite the improvements on the quality of the substrate and the epitaxial growth process, there is still a small limitation due to the fact that to obtain the maximum efficiency of the detector it is necessary to deplete the entire epitaxial thickness. The voltage at which a certain thickness is depleted, strongly depends on the doping level of the epitaxy, to have low depletion voltages it is necessary to have low doping and in our case this voltage is around 5000V (N_d=1x10^{14}/cm^3).

Nevertheless, if the FWHM of the detectors can be maintained to 14 MeV neutrons, the two better performing thick SiCs coupled with the new electronics could reach a 1.27% energy resolution, which would be similar to the best energy resolution achieved with diamonds (1%). This would require very high bias voltages to fully deplete the thick crystals, which is

unreachable with the current electronics. The functionality proven in this work, though, suggests that it is possible to use the detectors even with a partial depletion region, which would allow for an online tuning of the size of the active volume, and therefore the efficiency of the detector, without needing to substitute the crystal. This might prove also a feature for high temperature operation, where lower biases have been demonstrated to be more suitable for the detection.

However, in spite the depletion voltage limitation, the 4H-SiC detectors are the best competitive candidates on the field of neutron detection compared to the current detectors used, and the improvements on this technology may make them available soon on this market.

The results obtained so far, and possible future improvements from further technological developments, make the use of SiC detectors an exciting topic that will probably reserve, in the future, many other exiting outcomes in many application fields.

6 Bibliography

[1] M. Pillon and et al, “Radiation tolerance of a high quality synthetic single crystal chemical vapor deposition diamond detector irradiated by 14.8 MeV neutrons,” *Journal of Applied Physics ,* vol. 104, no. 054513, 2008.

[2] M. Angelone and e. al., *Rev. Sci. Instrum.,* vol. 77, no. 023505, 2006.

[3] C. Cazzaniga, M. Rebai, J. Garcia Lopez, M. Jimenez-Ramosc, M. Girolami, D. Trucchi, A. Bellucci, C. Frosta, M. Garcia-Munoz, M. Nocente, M. Tardocchi and G. Gorini, “Charge collection uniformity and irradiation effects of synthetic diamond detectors studied with a proton micro-beam,” *Nucl. Instrum. Methods Phys. Res.,* vol. 405, pp. 1-10, 2017.

[4] T. Tanaka, *Diam. Relat. Mater.,* vol. 14, p. 2031–2034, 2005.

[5] M. Rebai, A. Fazzi, C. Cazzaniga, G. Croci, M. Tardocchi, E. Cippo, C. Frost, D. Zaccagnino, V. Varoli and G. Gorini, “Time-stability of a Single-crystal Diamond Detector for fast neutron beam diagnostic under alpha and neutron irradiation.,” *Diam. Relat. Mater.,* vol. 61, pp. 1-6, 2016.

[6] F. Ruddy and e. al., “Nuclear Reactor Power Monitoring Using Silicon Carbide Semiconductor Radiation Detectors,” *Radiat. Detect. Nucl. Technol. ,* vol. 140, p. 198–208, 2002.

[7] D. Szalkai and e. al., “Animma,” in *Detection of 14 MeV neutrons in high temperature environment up to 500 °C using 4H-SiC based diode detector*, Lisbon, Portugal, 2015.

[8] M. Rebai and etal., “New thick silicon carbide detectors: Response to 14 MeV neutrons and comparison with single-crystal diamonds.,” *Nuclear Inst. and Methods in Physics Research, A,* vol. 946, no. 162637, 2019.

[9] D. Szalkai, R. Ferone, D. Gehre, F. Issa, A. Klix, A. Lyoussi, L. Ottaviani, T. Rücker, P. TüttĘ and V. Vervisch, “Detection of 14 MeV Neutrons in High Temperature Environment Up To 500 ºC Using 4H-SiC Based Diode Detector,” in *Animma*, Lisbon, Portugal, 2015.

[10] S. Tudisco and etal., “SiCILIA—Silicon Carbide Detectors for Intense Luminosity Investigations and Applications,” *Sensors,* vol. 18, no. 2289, 2018.

[11] M. Johnson and et al., “The 2.5-MeV neutron time-of-flight spectrometer TOFOR for experiments at JET,” *Nucl. Instrum. Methods,* vol. 591, p. 417, 2008.

[12] G. Ericsson and e. al., “Neutron emission spectroscopy at JET—Results from the magnetic proton recoil spectrometer,” *Rev. Sci. Instrum.,* vol. 72, p. 759, 2001.

[13] M. García and e. al., “NTM induced fast ion losses in ASDEX Upgrade,” *Nucl. Fusion,* vol. 47, p. 7, 2007.

[14] M. Mazzillo and e. al., “Single photon avalanche photodiodes arrays,” *Sensors Actuators ,* vol. 138, pp. 306-312, 2007.

[15] G. Knoll, Radiation Detection and Measurements 3rd edn, New York: Wiley, 2000.

[16] J. Biela, S. M. Member and S. K. J. Waffler, “SiC versus Si-Evaluation of Potentials for Performance Improvement of Inverter and DC–DC Con¬verter Systems by SiC Power Semiconductors,” *IEEE transactions on industrial electronics,* vol. 58, no. 7.

[17] D. Marckx, “Breakthrough in Power Electronics from SiC,” *National Renewable Energy Laboratory Report,* 2005.

[18] O. Kordina, “Growth and Characterization of Silicon Carbide,” *PhD thesis, Linkoping University,* 1994.

[19] F. Bechstedt, P. Käckell, A. Zywietz, K. Karch, B. Adolph, K. Tenelsen and J. Furthmüller, “Polytypism and Properties of Silicon Carbide,” *Phys. Stat. Sol. (b),* vol. 202, no. 1, pp. 32-65, 1997.

[20] A. R. Verma, “Crystal Growth and Dislocations,” *Butterworths Scientific Publications, Ltd. London,* 1953.

[21] L. Ramsdell, “Studies of Silicon Carbide,” *Am. Mineral.,* vol. 32, pp. 64-82, 1947.

[22] T. Kimoto and J. Cooper, Foundamentals of silicon carbide technology, Singapore: John Wiley & Sons, 2014 .

[23] W. J. Choyke and G. Pensl, “Physical Properties of SiC,” *MRS Bulletin,* 1997.

[24] J. Blakemore, “Semiconductor Statistics, International Series of Monographs on Semiconductors,” *Pergamon Press,* vol. 3, 1962.

[25] A. Hangleiter and R. Häcker, “Enhancement of band-to-band Auger recombination by electron-hole correlations,” *Phys. Rev. Lett.,* vol. 65, no. 2, pp. 215-218, 1990.

[26] P. Altermatt, J. Schmidt, G. Heiser and A. Aberle, “Assessment and parameterization of Coulomb-enhanced Auger recombination coefficients in lowly injected crystalline silicon,” *Journal of Applied Phys.,* vol. 82, pp. 4938-4944, 1997.

[27] A. Galeskas, J. SiCros, V. Grivickas, U. Lindefelt and C. Hallin, “Proceedings of the 7th International Conference on SiC, III-Nitrides and Related Materials,” Stockholm, Sweden, 1997.

[28] D. Schroder, Semiconductor Material and Device Characterization-2nd Edition, New York: John Wiley & Sons, Inc, 1998.

[29] W. W. Shockley and W. Read, “Statistics of the Recombination of Holes and Electrons,” *Physical Review,,* vol. 87, no. 5, pp. 835-842, 1952.

[30] S. Selberherr, Analysis and simulation of Semiconductor Device, Wien, Austria: SpringerVerlan, 1984.

[31] Y. Choi, H. Cha, L. Eastman and M. Spencer, “A New 4H-SiC Normally Off Lateral Channel Vertical JFET With Extremely Low Power Losses: Source Inserted Double-Gate Structure

With a Supplementary Highly Doped Region," *IEEE Trans. Electr. On Dev.,* vol. 52, no. 9, pp. 1940-1948, 2005.

[32] A. Galeckas, J. Linnros, M. Frischolz, K. Rottner, N. Nordell, S. Karlsson and V. Grivickas, "Investigation of surface recombination and carrier lifetime in 4H/6H-SiC," *Material Science and Engineering,* Vols. B61-62, pp. 239-243, 1999.

[33] M. Ruff, H. Mitlehner and R. Helbig, "SiC Devices: Physics and Numerical Simulation," *IEEE Trans. On Electr. Dev.,* vol. 41, no. 6, pp. 1040-1054, 1994.

[34] P. Grivickas, A. Galeckas, J. Linnros, M. Syväjärvi, R. Yakimova, V. Grivickas and J. Tellefsen, "Carrier lifetime investigation in 4H-SiC grown by CVD and sublimation epitaxy," *Mtrl. Sci. in Semiconductor Processing,* vol. 4, pp. 191-194, 2001.

[35] R. Davis, G. Kelner, M. Shur, J. Palmour and J. Edmond, *Proc.IEEE 79,* vol. 677, 1991.

[36] H. Matsunami and T. Kimoto, *Mater. Sci. Eng.,* vol. R20, no. 125, 1997.

[37] P. Neudeck, *J. Electron. Mater. ,* vol. 24, no. 283, 1995.

[38] H. Okumura, *Jpn. J. Appl. Phys.,* vol. Part 1 45, no. 7565, 2006.

[39] V. Jennings, S. A. and H. Chang, *J. Electrochemical Society,* vol. 728, p. 113, 1966.

[40] C. R.L. and C. T.L., *J. Electrochemical Society,* vol. 827, p. 113, 1966.

[41] A. Burk and L. Rowland, *Phys. Status Solidi B,* vol. 202, no. 263, 1997.

[42] T. Kimoto, A. Itoh and H. Matsunami, "Phys. Status Solidi B," *1997,* vol. 202, no. 247.

[43] T. Kimoto, "Step-controlled epitaxial growth of a-SiC and device applications," *Ph.D. thesis, Department of Electronic Science and Engineering, Kyoto University,* p. 21, 1995.

[44] O. Kordina, C. Hallin, R. Glass, A. Henry and E. Janzèn, "A novel hotwall CVD reactor for SiC epitaxy," Washington DC , 1993.

[45] A. Henry, J. Hassan, J. Bergman, C. Hallin and E. Janzèn, "Chem. Vap. Deposition 12," *2006,* vol. 475.

[46] A. Henry, S. Leone, F. Beyer, H. Pedersen, O. Kordina, S. Andersson and E. Janzèen, *Phys. B 407,* vol. 1467, 2012.

[47] B. Thomas, W. Bartsch, R. Stein, R. Schorner and D. Stephani, *Mater.Sci. Forum,* vol. 181, p. 457–460, 2004.

[48] O. Danielsson, C. Hallin and E. Janzèn, *J. Cryst. Growth,* vol. 289, p. 252, 2003.

[49] S. Ryu, S. Krishnaswami, M. O'Loughlin, J. Richmond, A. Agarwal, J. Palmour and A. Hefner, *IEEE Electron Device Lett. ,* vol. 556, no. 25, 2004.

[50] J. Zhao, P. Alexandrov, J. Zhang and X. Li, *IEEE Electron Device Lett. 25(7),* vol. 474, 2004.

[51] M. Das, J. Sumakeris, B. Hull, J. Richmond, S. Krishnaswami and A. Powell, *Mater. Sci. Forum,* vol. 483, no. 965, 2005.

[52] J. Zhao, P. Alexandrov and X. Li, *IEEE Electron Device Lett. 24(6),* vol. 402, 2003.

[53] A. Huang, M. Crow, G. Heydt, J. Zheng and S. Dale, *Proc. IEEE 99(1),* vol. 133, 2011.

[54] J. Cooper and A. Agarwal, *Proc. IEEE 90(6),* vol. 956, 2002.

[55] H. Jacobson, J. Bergman, C. Hallin, E. Janzèn, T. Tuomi and H. Lendenmann, *J. Appl. Phys.,* vol. 95, no. 1485, 2004.

[56] L. Storasta, J. Bergman, C. Hallin and E. Janzèn, *Mater. Sci. Forum ,* vol. 549, p. 389–393, 2002.

[57] T. Tawara, H. Tsuchida, S. Izumi, I. Kamata and K. Izumi, "Evaluation of Free Carrier Lifetime and Deep Levels of the Thick 4H-SiC epilayers," *Mater. Sci. Forum,* vol. 565, p. 457–460, 2004.

[58] F. La Via, G. Galvagno, G. Foti, M. Mauceri, S. Leone, G. Pistone, G. Abbondanza, A. Veneroni, M. Masi, G. Valente and D. Crippa, *Chem. Vap. Deposition,* vol. 509, p. 12, 2006.

[59] L. Calcagno, G. Izzo, G. Litrico, G. Foti, F. La Via, G. Galvagno, M. Mauceri and S. Leone, *J. Appl. Phys.,* no. 043523, p. 102, 2007.

[60] S. Leone, M. Mauceri, G. Pistone, G. Abbondanza, F. Portuese, G. Abagnale, G. Valente, D. Crippa, M. Barbera, R. Reitano, G. Foti and F. La Via, *Mater. Sci. Forum,* vol. 179, p. 527–529, 2006.

[61] F. La Via, G. Izzo, M. Camarda, G. Abbondanza and D. Crippa, *Mater. Sci. Forum,* vol. 55, p. 615–617, 2009.

[62] A. Veneroni and M. Masi, *Chem. Vap. Deposition,* vol. 562, p. 12, 2006.

[63] D. Crippa and etAl., *Mater. Sci. Forum,* vol. 67, no. 72, pp. 483-485, 2005.

[64] F. La Via and etAl, *Mater. Sci. Forum,* vol. 157, pp. 556-557, 2007.

[65] P. Lu, J. Edgar, O. Glembocki, P. Klein, E. Glaser, J. Perrin and J. Chaudhuri, *J. Cryst. Growth,* vol. 506, p. 285, 2005.

[66] H. Pedersen, S. Leone, A. Henry, V. Darakchieva and E. Janzèn, *Surf. Coat. Technol.,* vol. 201, no. 8931, 2007.

[67] H. Tsuchida, M. Ito, I. Kamata and M. Nagano, "Formation of extended defects in 4H-SiC epitaxial growth and development of a fast growth technique," *Phys. Status Solidi B,* vol. 246, no. 1553, 2009.

[68] T. Kimoto and J. Cooper, Fundamentals of Silicon Carbide Technology, Singapore: John Wiley & Sons, 2014.

[69] T. Kimoto, “Material science and device physics in SiC technology for high-voltage power devices,” *Jpn. J. Appl. Phys.,* vol. 54, no. 040103, 2015.

[70] S. Ha, P. Mieszkowski, M. Skowronski and L. Rowland, “Dislocation conversion in 4H silicon carbide epitaxy,” *J. Cryst. Growth,* vol. 244, no. 257, 2002.

[71] G. Feng, J. Suda and T. Kimoto, “Characterization of major in-grown stacking faults in 4HSiC epilayers,” *Phys. B,* vol. 4745, pp. 23-24, 2009.

[72] I. Kamata, X. Zhang and H. Tsuchida, “Photoluminescence of Frank-type defects on the basal plane in 4H-SiC epilayers,” *Appl. Phys. Lett.,* no. 1721107, p. 97, 2010.

[73] H. Fujiwara, H. Naruoka, M. Konishi, K. Hamada, T. Katsuno and T. Ishikawa, “Impact of surface morphology above threading dislocations on leakage current in 4HSiC diodes,” *Appl. Phys. Lett.,* vol. 101, no. 042104, 2012.

[74] S. Sze and K. Ng, Physics of Semiconductor Devices, 3rd ed., New York: Wiley, 2007.

[75] J. Senzaki, A. Shimozato, K. Kojima, T. Kato, Y. Tanaka and K. Fukuda, “Challenges of high-performance and high-reliablity in SiC MOS structures,” *Mater. Sci. Forum ,* no. 703, pp. 717-720, 2012.

[76] M. Skowronski and S. Ha, “Degradation of hexagonal silicon-carbide-based bipolar devices,” *J. Appl. Phys,* vol. 99, no. 011101, 2006.

[77] T. Tawara, T. Miyazawa, M. Ryo, M. Miyazato, T. Fujimoto and K. Takenaka, “Short minority carrier lifetimes in highly nitrogen-doped 4H-SiC epilayers for suppression of the stacking fault formation in PiN diodes,” *J. Appl. Phys.,* vol. 120, no. 115101, 2016.

[78] S. Hino, H. Hatta, K. Sadamatsu, Y. Nagahisa, S. Yamamoto and T. Iwamatsu, “Demonstration of SiC-MOSFET embedding Schottky barrier diode for inactivation of parasitic body diode,” *Mater. Sci. Forum,* vol. 897, no. 477, 2017.

[79] M. Tajima, M. Tanaka and N. Hoshino, “Characterization of SiC epitaxial wafers by photoluminescence under deep UV excitation,” *Mater. Sci. Forum,* vol. 597, pp. 389-393, 2002.

[80] R. Stahlbush, K. Liu, Q. Zhang and J. Sumakeris, “Whole-wafer mapping of dislocations in 4H-SiC epitaxy,” *Mater. Sci. Forum ,* vol. 297, pp. 556-557, 2007.

[81] K. Kawahara, G. Alfieri and T. Kimoto, “Detection and depth analyses of deep levels generated by ion implantation in n- and p-type 4H-SiC,” *J. Appl. Phys.,* vol. 106, no. 013719, 2009.

[82] T. Dalibor, G. Pensl, H. Matsunami, T. Kimoto, W. Choyke and A. Schoner, “Deep defect centers in silicon carbide monitored with deep level transient spectroscopy,” *Phys. Status Solidi A ,* vol. 162, no. 199, 1997.

[83] C. Hemmingsson, N. Son, O. Kordina, J. Bergman, E. Janzèn and J. Lindstrom, “Deep level defects in electron-irradiated 4H SiC epitaxial layers,” *J. Appl. Phys.,* vol. 81, no. 6155, 1997.

[84] N. Son, X. Trinh, L. Løvlie, B. Svensson, K. Kawahara and J. Suda, “Negative-U system of carbon vacancy in 4H-SiC,” *Phys. Rev. Lett.,* vol. 109, no. 187603, 2012.

[85] T. Troffer, M. Schadt, T. Frank, H. Itoh, G. Pensl and J. Heindl, “Doping of SiC by implantation of boron and aluminum,” *Phys. Status Solidi A,* vol. 162, no. 277, 1997.

[86] K. Danno, D. Nakamura and T. Kimoto, “Investigation of carrier lifetime in 4H-SiC epilayers and lifetime control by electron irradiation,” *Appl. Phys. Lett.,* vol. 90, no. 202109, 2007.

[87] L. Storasta and H. Tsuchida, “Reduction of traps and improvement of carrier lifetime in 4HSiC epilayers by ion implantation,” *Appl. Phys. Lett.,* vol. 90, no. 062116, 2007.

[88] T. Hiyoshi and T. Kimoto, “Reduction of deep levels and improvement of carrier lifetime in n-type 4H-SiC by thermal oxidation,” *Appl. Phys. Express 2,* no. 041101, 2009.

[89] C. Fisher, M. Jennings, Y. Sharma, D. Hamilton, P. Gammon, A. Pérez-Tomás, S. Thomas, S. Burrows and P. Mawby, “Improved performance of 4H-SiC PiN Diodes using a novel combined high temperature oxidation and annealing process,” *IEEE transactions on semiconductor manufacturing,* vol. 27, no. 3, 2014.

[90] T. Kimoto, K. Kawahara, B. Zippelius, E. Saito and J. Suda, “Control of carbon vacancy in SiC toward ultrahigh-voltage power devices,” *Superlattices Microstruct.,* vol. 99, no. 151, 2016.

[91] T. Okuda, T. Miyazawa, H. Tsuchida, T. Kimoto and J. Suda, “Carrier lifetimes in lightlydoped doped p-type 4H-SiC epitaxial layers enhanced by post-growth processes and surface passivation,” *J. Electron. Mater.,* no. 6411, p. 46, 2017.

[92] A. Galeckas, J. Linnros, V. Grivickas, U. Lindefelt and C. Hallin, “Auger recombination in 4H-SiC: Unusual temperature behavior,” *Appl. Phys. Lett.,* vol. 71, no. 3269, 1997.

[93] T. Kimoto, K. Yamada, H. Niwa and J. Suda, “Promise and challenges of high-voltage SiC bipolar power devices,” *Energies,* vol. 9, no. 908, 2016.

[94] R. Babcock, S. Ruby, F. Schupp and K. Sun, “Miniature Neutron Detectors,” *Westinghouse Electric Corporation Materials Engineering Report,* no. 5711-6600, 1957.

[95] R. Babcock and H. Chang, “Silicon Carbide Neutron Detectors for High-Temperature Operation, In : Reactor Dosimetry,” vol. 1, Vienna, Austria, International Atomic Energy Agency,, 1963, p. 613.

[96] R. Ferber and G. Hamilton, “Silicon Carbide High Temperature Neutron Detectors for Reactor Instrumentation,” *Westinghouse Research & Development Center Report,* no. 65-1C2-RDFCT-P3, 1965.

[97] V. Tikhomirova, O. Fedoseeva and G. Kholuyanov, “Properties of Ionizing-Radiation Counters Made of Silicon Carbide Doped by Diffusion of Beryllium,” *Soviet Physics – Semiconductors,* vol. 6, no. 5, 1972.

[98] V. Tikhomirova, O. Fedoseeva and G. Kholuyanov, “Detector Characteristics of a Silicon Carbide Detector Prepared by Diffusion of Beryllium,” *Atomnaya Energiya ,* vol. 34, no. 2, pp. 122-124, 1973.

[99] V. Evstropov, A. Strel’chuk, A. Syrkin and V. Chelnokov, “The Effect of Neutron Irradiation on Current in SiC pn Structures,” *Inst. Physics Conf. Ser. ,* vol. 6, no. 137, 1993.

[100] F. Ruddy, A. Dulloo, J. Seidel, S. Seshadri and B. Rowland, “Development of a Silicon Carbide Radiation Detector,” *IEEE Transactions on Nuclear Science,* vol. 45, pp. 536-541, 1999.

[101] F. Nava, P. Vanni, C. Lanzieri and C. Canali, “Epitaxial Silicon Carbide Charge Particle Detectors,” *Nuclear Instruments and Methods in Physics Research A,* vol. 437, pp. 354-358, 1999.

[102] B. Phlips, K. Hobart, F. Kub, R. Stahlbush, M. Das, G. De Geronimo and P. O’Connor, “Silicon Carbide Power Diodes as Radiation Detectors,” *Materials Science Forum,* Vols. 527-529, pp. 1465-1468, 2006.

[103] J. Lees, D. Bassford, G. Fraser, A. Horsfall, K. Vassilevski, N. Wright and A. Owens, “Semi-Transparent SiC Schottky Diodes for X-Ray Spectroscopy,” *Nuclear Instruments & Methods in Physics Research A,* vol. 578, pp. 226-234, 2007.

[104] M. Bruzzi, S. Lagomarsino, F. Nava and S. Sciortino, “Characteristics of Epitaxial SiC Schottky Barriers as Particle Detectors,” *Diamond and Related Materials,* vol. 12, pp. 1205-1208, 2003.

[105] F. Ruddy, “Silicon carbide radiation detectors: Progress, limitations and future directions.,” *Mater Res Soc Online Proc,* vol. 101, no. 1576, 2013.

[106] D. N. M, “ SiC detectors: A review on the use of silicon carbide as radiation detection material.,” *Front. Phys.,* vol. 10, no. 898833, 2022.

[107] F. Moscatelli, A. Scorzoni, A. Poggi, M. Bruzzi, S. Sciortino and S. Lagomarsino, “Radiation hardness after very high neutron irradiation of minimum ionizing particle detectors based on 4H-SiC p/sup +/n junctions.,” *IEEE Trans Nucl Sci,* vol. 53, no. 1557, p. 63, 2006.

[108] F. Nava, P. Vanni, M. Bruzzi, S. Lagomarsino, S. Sciortino and G. Wagner, “Minimum ionizing and alpha particles detectors based on epitaxial semiconductor silicon carbide.,” *IEEE Trans Nucl Sci ,* vol. 51, no. 238, p. 44, 2004.

[109] F. Nava, G. Bertuccio, A. Cavallini and E. Vittone, “Silicon carbide and its use as a radiation detector material.,” *Meas Sci Technol ,* vol. 19, no. 102001, 2008.

[110] M. Rogalla, K. Runge and A. Söldner-Rembold, “Particle detectors based on semiinsulating silicon carbide.,” *Nucl Phys B - Proc Supplements ,* vol. 78, no. 516, p. 20, 1999.

[111] A. Lo Giudice, F. Fizzotti, C. Manfredotti, E. Vittone and F. Nava, “Average energy dissipated by mega-electron-volt hydrogen and helium ions per electron-hole pair generation in 4H-SiC.,” *Appl Phys Lett,* vol. 87, no. 222105, 2005.

[112] R. Bernat, I. Capan, L. Bakra õc, T. Brodar, T. Makino and T. Ohshima, “Response of 4h-sic detectors to ionizing particles,” *Crystals ,* vol. 10, p. 11, 2021.

[113] S. Chaudhuri, O. Karadavut, J. Kleppinger and K. Mandala, “High-resolution radiation detection using ni/sio2/n-4h-sic vertical metal-oxide-semiconductor capacitor.,” *J Appl Phys ,* vol. 130, no. 074501, 2021.

[114] M. De Napoli, F. Giacoppo, G. Raciti and E. Rapisarda, “Dopant concentration dependence of the response of sic Schottky diodes to light ions.,” *Nucl Instr Methods Phys Res Section A: Acc Spectrometers, Detectors Associated Equipment,* vol. 600, no. 618, p. 23, 2009.

[115] J. Kleppinger, S. Chaudhuri, O. Karadavut and K. Mandal, “Defect characterization and charge transport measurements in high-resolution Ni/n-4HSiC Schottky barrier radiation detectors fabricated on 250 um epitaxial layers.,” *J. Appl. Phys.,* vol. 129, no. 244501, 2021.

[116] A. Sciuto, F. Roccaforte, S. Franco, V. Raineri and G. Bonanno, “High responsivity 4H-SiC Schottky UV photodiodes based on the pinch-off surface effect.,” *Appl Phys Lett ,* vol. 89, no. 081111, 2006.

[117] B. Ng, J. David, R. Tozer, G. Rees, Y. Feng and J. Zhao, “Nonlocal effects in thin 4h–sic uv avalanche photodiodes.,” *IEEE Trans Electron Devices,* vol. 50, no. 1724, p. 32, 2003.

[118] A. Ivanov, N. Strokan and A. Lebedev, “Radiation hardness of a wide-bandgap material by the example of SiC nuclear radiation detectors,” *Nucl. Instrum. Methods Phys. Res. A ,* vol. 675, pp. 20-23, 2012.

[119] F. Ruddy and etal., *IEEE Transactions on Nuclear Science ,* vol. 53, pp. 1666-1670, 2006.

[120] F. Ruddy, L. Ottaviani, A. Lyoussi, C. Destouches, O. Palais and C. Carette, “Performance and applications of silicon carbide neutron detectors in harsh nuclear environments.,” *EPJ Web Conf ,* vol. 253, no. 11003, 2021.

[121] J. Coutinho, V. JBTorres, I. Capan, T. Brodar, Z. Ereš and R. Bernat, “Silicon carbide diodes for neutron detection.,” *Nucl Instr Methods Phys Res Section A: Acc Spectrometers, Detectors Associated Equipment ,* vol. 986, no. 164793, 2021.

[122] T. Brodar, I. Capan, V. Radulovic, L. Snoj, Z. Pastuovic and J. Coutinho, “Laplace DLTS study of deep defects created in neutron-irradiated n-type 4H-SiC.,” *Nucl Instr Methods Phys Res Section B: Beam Interactions Mater Atoms ,* vol. 437, pp. 27-31, 2018.

[123] “Fluka,” [Online]. Available: http://www.fluka.org/fluka.php. [Accessed dicembre 2019].

[124] A. Muoio, A. Meli, A. Trotta, M. Parisi, L. Meda and F. La Via, “Neutron Detection Study through Simulations with Fluka,” *Materials Science Forum,* vol. 1062, p. 509–513, 2022.

[125] F. La Via, M. Camarda and A. La Magna, “Mechanisms of growth and defect properties of epitaxial SiC,” *Applied Physics Reviews 1,* no. 031301, 2014.

[126] F. La Via, G. Izzo, M. Camarda, G. Abbondanza and D. Crippa, “Thick Epitaxial Layers Growth by Chlorine Addition,” *Materials Science Forum Vols.,* vol. 55, pp. 615-617, 2009.

[127] S. Ichikawa, K. Kawahara, J. Suda and T. Kimoto, " Carrier Recombination in n-Type 4H-SiC Epilayers with Long Carrier Lifetimes.," *Applied Physics Express ,* vol. 5, no. 101301, 2012.

[128] T. Miyazawa and etal., *Applied Physics Letters,* vol. 97, no. 202106 , 2010.

[129] A. Meli, A. Muoio, A. Trotta, L. Meda, M. Parisi and F. La Via, "Epitaxial Growth and Characterization of 4H-SiC for Neutron Detection Applications," *Materials,* vol. 976, no. 14, 2021.

[130] W. Choyke and R. Devaty, "Silicon Carbide Recent Major advances," in *Optical Properties of SiC: 1997-2002*, Berlin, Springer-Verlag, 2004, p. 413–433.

[131] D. Schroder, "Semiconductor Material and Device Characterization, 3rd edn," *Wiley-IEEE,* 2006.

[132] D. Feldman, J. J. Parker, W. Choyke and L. Patrick, "Phonon dispersion curves by Raman scattering in SiC, polytypes 3C, 4H, 6H, 15R, and 21R.," *Phys. Rev.,* vol. 170, no. 968, 1968.

[133] S. Nakashima and H. Harima, in *Characterization of defects in SiC crystals by Raman scattering, in Silicon Carbide – Recent Major Advances*, Springer, 2004, p. 585.

[134] S. Nakashima, "Raman imaging of semiconductormaterials: characterization of static and dynamic properties," *J. Phys. Condens. Matter,* vol. 16, no. s25, 2004.

[135] S. Nakashima, H. Okumura, T. Yamamoto and R. Shimidzu, "Deep-ultraviolet Raman microspectroscopy: characterization of wide-gap semiconductors.," *Appl. Spectrosc. ,* vol. 58, no. 224, 2004.

[136] S. Nakashima and H. Harima, "Raman investigation of SiC polytypes," *Phys. Status Solidi A,* vol. 162, no. 39, 1997.

[137] H. Harima, S. Nakashima and T. Uemura, "Raman scattering from anisotropic LO-phononplasmon– coupled mode in n-type 4H- and 6H-SiC," *J. Appl. Phys.,* vol. 78, no. 1996, 1995.

[138] D. Lockwood and J. Baribeau, "Strain-shift coefficients for phonons in Si1-xGex epilayers on silicon," *Phys. Rev. B,* vol. 45, no. 8565, 1992.

[139] S. Rohmfeld, M. Hundhausen and L. Ley, *Phys. Status Solidi B ,* vol. 215, no. 115, 1999.

[140] T. Mitani, S. Nakashima, H. Okumura and H. Nakasawa, *Mater. Sci. Forum,* vol. 343, p. 527–529, 2006.

[141] N. Piluso, R. Anzalone, M. Camarda, A. Severino, A. La Magna, G. D'Arrigo and F. La Via, *J. Raman Spectrosc.,* vol. 44, no. 299, 2013.

[142] N. Piluso, R. Anzalone, A. Severino, A. La Magna, G. D'Arrigo and F. La Via, *Mater. Sci. Forum,* vol. 141, p. 679–680, 2011.

[143] S. Nakashima, Y. Nakatake, H. Harima, M. Katsuno and N. Ohtani, *Appl. Phys. Lett. ,* vol. 77, no. 3612, 2000.

[144] T. Tomita, S. . Matsuo, T. Okada, T. Kimoto, H. Matsunami, T. Mitani and S. Nakashima, *Appl. Phys. Lett. ,* vol. 87, no. 241906, 2005.

[145] S. Nakashima, T. Mitani, J. Senzaki, H. Okumura and T. Yamamoto, *J. Appl. Phys. ,* vol. 97, no. 123507, 2005.

[146] Yu, P.Y. and M. Cardona, Fundamentals of Semiconductors, 2nd ed., New York: Springer-Verlag Berlin Heidelberg, 2003.

[147] G. Irmer, V. Toporov, B. Bairamov and J. Monecke, "Determination of the charge carrier concentration and mobility in n-gap by Raman Spectroscopy," *Phys. Status Solidi B,* vol. 119, no. 595, 1983.

[148] H. Harima, S. Nakashima and T. Uemura, "Raman scattering from anisotropic LO-phonon–plasmon–coupled mode in n-type 4H- and 6H-SiC," *J. Appl. Phys.,* vol. 78, no. 1996, 1995.

[149] M. Chafai, A. Jaouhari, A. Torres, R. Anton, E. Martin, J. Jimenez and W. Mitchel, "Raman scattering from LO phonon-plasmon coupled modes and Hall-effect in n-type silicon carbide 4H–SiC," *J. Appl. Phys.,* vol. 90, no. 5211, 2001.

[150] N. Piluso, A. Severino, M. Camarda, R. Anzalone, A. Canino, G. Condorelli, G. Abbondanza and F. La Via, "Raman characterization of doped 3C-SiC/Si for different silicon substrates and C/Si ratios.," *Mater. Sci. Forum,* vol. 255, pp. 645-648, 2010.

[151] H. Yugami, S. Nakashima, A. Mitsuishi, A. Uemoto, M. Shigeta, K. Furukawa, A. Suzuki and S. Nakajima, *J. Appl. Phys. ,* vol. 354, p. 61, 1987.

[152] J. Caldwell, O. Glembocki, S. Prokes, E. Glaser, K. Hobart, D. Hansen, G. Chung, A. Bolotnikov and T. Sudarshan, "Free carrier distribution profiling of 4H-SiC substrates using a commercial optical scanner," *J. Appl. Phys.,* vol. 101, no. 093506, 2007.

[153] H. Nather, L. Quagliano and J. Lumin, vol. 50, p. 30, 1985.

[154] H. Yugami, S. Nakashima, Y. Oka, M. Hangyo and A. Mitsuishi, *J. Appl. Phys.,* vol. 3303, p. 60, 1986.

[155] O. Glembocki, M. Skowronski, S. Prokes, D. Gaskill and J. Caldwell, *Mater. Sci. Forum,* vol. 347, pp. 527-529, 2006.

[156] Horiba, "LabRAM HR Evolution Confocal Raman Microscope," [Online]. Available: https://www.horiba.com/int/scientific/products/detail/action/show/Product/labram-hr-evolution-1083/. [Accessed 10 November 2020].

[157] P. Klein, "Carrier lifetime measurement in n- 4H-SiC epilayer," *J. Appl. Phys.,* vol. 103, no. 033702, 2008.

[158] D. Lang, *J. Appl. Phys.,* vol. 45, no. 3023, 1974.

[159] D. Losee, *Appl. Phys. Lett.,* vol. 21, no. 54, 1972.

[160] D. Lang, Topics in Applied Physics - Thermally Stimulated Relaxation in Solids, New York: P. Bräunlich, Soringer Verlag, 1979.

[161] C. Sah and J. Walker, *Appl. Phys. Lett. ,* vol. 384, p. 22, 1973.

[162] T. Kimoto, G. Feng, K. Danno, T. Hiyoshi and J. Suda, "4H-SiC epitaxial growth and defect characterization.," in *Silicon Carbide Epitaxy*, Gujarat, India, La Via Ed., Research Signpost, 2012, p. 121–144..

[163] G. Feng, J. Suda and T. Kimoto, "Characterization of stacking faults in 4H-SiC epilayers by room-temperature microphotoluminescence mapping. Characterization," vol. 92, no. 221906, 2008.

[164] N. Piluso, M. Camarda and F. La Via, "A novel micro-Raman technique to detect and characterize 4H-SiC stacking faults.," *J. Appl. Phys.,* vol. 116, no. 163506, 2014.

[165] N. Piluso, A. Severino, M. Camarda, A. Canino, A. La Magna and F. La Via, "Optical investigation of bulk electron mobility in 3C–SiC films on Si substrates," *Appl. Phys. Lett.,* vol. 97, no. 142103, 2010.

[166] J. Burton, L. Sun, M. Pophristic, S. Lakacs, F. Long, Z. Feng and I. Ferguson, "Spatial characterization of doped SiC wafers by Raman spectroscopy," *J. Appl. Phys.,* vol. 84, no. 6268, 1998.

[167] M. Camarda, A. La Magna and F. La Via, "A kinetic Monte Carlo method on super-lattices for the study of the defect formation in the growth of close packed structures," *J. Comput. Phys,* vol. 227, no. 1075, 2007.

[168] M. Camarda, A. La Magna, P. Fiorenza, G. Izzo and F. La Via, "Theoretical Monte Carlo study of the formation and evolution of defects in the homoepitaxial growth of SiC.," *Mater. Sci. Forum ,* vol. 135, pp. 600-603, 2009.

[169] F. La Via, G. Galvagno, A. Firrincieli, F. Roccaforte, S. Di Franco, A. Ruggiero, M. Barbera, R. Reitano, P. Musumeci, L. Calcagno and etal, "Epitaxial layers grown with HCl addition: A comparison with the standard process.," *Mater. Sci. Forum,* vol. 163, pp. 527-529, 2006.

[170] A. Galeckas, V. Grivickas, J. Linnros, U. Lindefelt and C. Hallin, "Evaluation of Auger Recombination Rate in 4H-SiC," Stafa-Zurich, Switzerland, Tech, Trans Publications Ltd., 1998.

[171] P. Scajev and K. .. Jarasiunas, "Temperature- and excitation-dependent carrier diffusivity and recombination rate in 4H-SiC," *J. Phys. D Appl. Phys. ,* vol. 46, no. 265304, 20013.

[172] S. Privitera, G. Litrico, M. Camarda, N. Piluso and F. la Via, "Electrical properties of extended defects in 4H-SiC investigated by photoinduced current measurements," *Appl. Phys. Express,* vol. 10, no. 036601, 2017.

[173] R. Myers-Ward, K. Lew, B. VanMil, R. Stahlbush and K. Liu, " Impact of 4H-SiC Substrate Defectivity on Epilayer Injected Carrier," *Mater. Sci. Forum ,* vol. 481–484, pp. 600–603,, 2009.

[174] T. Kimoto, K. Danno and J. Suda, “Lifetime-killing defects in 4H-SiC epilayers and lifetime control by low-energy electron irradiation.,” *Phys. Status Solidi B ,* vol. 245, p. 1327–1336, 2008.

[175] T. Kimoto, K. Hashimoto and H. Matsunami, “Effects of C/Si Ratio in Chemical Vapor Deposition of 4H-SiC(1120) and (0338),” *Jpn. j. Appl. Phys. ,* vol. 12R, p. 42, 2003.

[176] J. Zhang, L. Storasta, J. Bergman, N. Son and E. Janzén, “Electrically active defects in n-type 4H–silicon carbide grown in a vertical hot-wall reactor,” *J. Appl. Phys.,* vol. 93, no. 4708, 2003.

[177] K. Danno, T. Hori and T. Kimoto, “Impacts of growth parameters on deep levels in n-type 4H-SiC,” *J. Appl. Phys.,* vol. 101, no. 053709, 2007.

[178] L. Storasta, H. Tsuchida, T. Miyazawa and T. Ohshima, “ Enhanced annealing of the Z 1/2 defect in 4H–SiC epilayers.,” *J. Appl. Phys.,* vol. 103, no. 013705, 2008.

[179] T. Hiyoshi and T. Kimoto, “Elimination of the Major Deep Levels in n- and p-Type 4H-SiC,” *Appl. Phys. Express ,* vol. 2, no. 091101, 2009.

[180] K. Kawahara, J. Suda and T. Kimoto, “Analytical model for reduction of deep levels in SiC by thermal oxidation.,” *J. Appl. Phys.,* vol. 111, no. 053710, 2012.

[181] S. Maximenko, J. J. Freitas, P. Klein, S. Shrivastava and T. Sudarshan, “Cathodoluminescence study of the properties of stacking faults in 4H-SiC homoepitaxial layers.,” *Appl. Phys. Lett. ,* vol. 94, no. 092101, 2009.

[182] J. Hassan and J. Bergman, “Influence of structural defects on carrier lifetime in 4H-SiC epitaxial layers: Optical lifetime mapping,” *J. Appl. Phys.,* vol. 105, no. 123518, 2009.

[183] T. Kimoto, T. Hiyoshi, T. Hayashi and J. Suda, “Impacts of recombination at the surface and in the substrate on carrier lifetimes of n-type 4H–SiC epilayers.,” *J. Appl. Phys.,* vol. 108, no. 083721, 2010.

[184] E. Sveinbjörnsson and Ó. Gíslason, “Deep traps in 4H-SiC MOS capacitors investigated by Deep Level Transient Spectroscopy.,” *Mater. Sci. Forum,* vol. 603–606, p. 778–780, 2014.

[185] K. Kawahara, J. Suda and T. Kimoto, “Deep Levels Generated by Thermal Oxidation in n-Type 4H-SiC.,” *Appl. Phys. Express ,* vol. 6, no. 051301, 2013.

[186] A. Meli, A. Muoio, R. Reitano, E. Sangregorio, L. Calcagno, A. Trotta, M. Parisi, M. Meda and F. La Via, “Effect of the Oxidation Process on Carrier Lifetime and on SF Defects of 4H SiC Thick Epilayer for Detection Applications,” *Micromachines ,* vol. 13, no. 1042, 2022.

[187] B. Baliga, Physics of Semiconductor Power Devices, vol. 75, JWS Publishing, 1996.

[188] A. Chynoweth, “Ionization rates for electrons and holes in silicon,” *Phys. Rev.,* vol. 109, no. 1537, 1958.

[189] A. Konstantinov, Q. Wahab, N. Nordell and U. Lindefelt, “Ionization rates and critical fields in 4H silicon carbide,” *Appl. Phys. Lett.,* vol. 71, no. 90, 1997.

[190] P. Neudeck, D. Larkin, E. Starr and e. al., “Electrical properties of epitaxial 3C- and 6H-SiC p-n junction diodes produced side-by-side on 6H-SiC substrates,” *IEEE Trans. Electron Devices,* vol. 41, no. 826, 1994.

[191] J. J. Cooper, M. Melloch, R. Singh and e. al., “ Status and prospects for SiC power MOSFETs.,” *IEEE Trans. Electron Devices,* vol. 49, no. 658, 2002.

[192] M. Ruff, H. Mitlehner and R. Helbig, “SiC devices: physics and numerical simulation.,” *IEEE Trans. Electron Devices,* vol. 41, no. 1040, 1994.

[193] M. Kushoro, M. Rebai, M. Tardocchi, C. Altana, C. Cazzaniga, E. De Marchi, F. La Via, L. Meda, A. Meli, M. Parisi, E. Cippo, M. Pillon, A. Trotta, S. Tudisco and G. Gorini, “Detector Response to D-D Neutrons and Stability Measurements with 4H Silicon Carbide Detectors,” *Materials,* vol. 568, p. 14, 2021.

[194] G. Ericsson, “Advanced Neutron Spectroscopy in Fusion Research,” *J. Fusion Energy ,* vol. 38, pp. 330-355, 2019.

[195] JET, “EURO fusion’s Flagship Device.,” [Online]. Available: https://www.euro-fusion.org/devices/jet/. [Accessed 20 december 2020].

[196] D. Rigamonti, L. Giacomelli, G. Gorini, M. Nocente, M. Rebai, M. Tardocchi, M. Angelone, P. Batistoni and A. Cufar, “Neutron spectroscopy measurements of 14 MeV neutrons at unprecedented energy resolution and implications for deuterium–tritium fusion plasma diagnostics.,” *Meas. Sci. Technol.,* no. 045502, p. 29, 2018.

[197] J. Thomason, “The ISIS spallation neutron and muon source—the first thirty-three years.,” *Nucl. Instrum. Methods Phys. Res. Sect. A Accel. Spectrometers Detect. Assoc. Equip. ,* vol. 917, pp. 61-67, 2019.

[198] L. Giacomelli, M. Rebai, A. Fazzi, E. Cippo, M. Tardocchi, C. Frost, A. Pietropaolo, N. Rhodes, E. Schooneveld and G. Gorini, “Pulsed neutron beam measurements with diamond detectors.,” *Nucl. Instrum. Methods Phys. Res. Sect. A,* vol. 720, p. 125–127., 2013.

[199] ITER. [Online]. Available: www.iter.org. [Accessed 20 december 2020].

[200] Y. Sato, T. Shimaoka, J. Kaneko, H. Murakami, M. Isobe, M. Osakabe, M. Tsubota, K. Ochiai, A. Chayahara and H. Umezawa, “Radiation hardness of a single crystal CVD diamond detector for MeV energy protons.,” *Nucl. Instrum. Methods Phys. Res. Sect. A ,* vol. 784, pp. 147-150, 2015.

[201] M. Kushoro, M. Rebai, M. Dicorato, D. Rigamonti, C. Altana, C. Cazzaniga, G. Croci, G. Gorini, G. Lanzalone and F. la Via, “Silicon Carbide characterization at the n_TOF spallation source with quasi-monoenergetic fast neutrons.,” *Nucl. Instrum. Methods Phys. Res. Sect. A Accel. Spectrometers Detect. Assoc. Equip. ,* vol. 983, no. 164578, 2020.

[202] M. Kushoro, M. Rebai, F. La Via, A. Meli, L. Meda, M. Parisi, E. Cippo, O. Putignano, A. Trotta and M. Tardocchi, “Performance of a Thick 250µm Silicon Carbide Detector: Stability and Energy Resolution”.

[203] D. Napoli and M., “SiC detectors: A review on the use of silicon carbide as radiation detection material,” *Front. Phys.,* 2022.

[204] H. Harima, S. Nakashima and T. Uemura, “Raman scattering from anisotropic LO-phonon–plasmon–coupled mode in n-type 4H–and 6H–SiC.,” *J. Appl. Phys.,* vol. 79, no. 1996, 1995.

[205] N. Sugiyama, A. Okamoto and T. Tani, “Growth orientation dependence of dopant incorporation in bulk SiC single crystals,” *Inst. Phys. Conf. Ser.,* vol. 142, no. 489, 1996.